UNIVERSITY OF COPENHAGEN

Sofie Lindskov Hansen

Single-Photon Manipulation in Nanophotonic Circuits

Ph.D.

Sofie Lindskov Hansen

Single-Photon Manipulation in Nanophotonic Circuits

Ph.D.

Single-Photon Manipulation in Nanophotonic Circuits

This thesis was prepared by
Sofie Lindskov Hansen

Supervisors
Peter Lodahl

Release date: 14.09.2017

Comments: A dissertation submitted to the Niels Bohr Institute at the University of Copenhagen in partial fulfillment of the requirements for the degree of philosophiae doctor

Quantum Photonics Group
Niels Bohr Institute
University of Copenhagen
Blegdamsvej 17
DK-2100 Copenhagen
Denmark

http://quantum-photonics.nbi.ku.dk/

Preface

The work presented in this thesis is the result of three years of research carried out in the Quantum Photonics group at the Niels Bohr Institute, University of Copenhagen under supervision of Professor Peter Lodahl and Assistant Professor Leonardo Midolo.

I would like to sincerely thank Peter Lodahl for giving me the opportunity to work within this fascinating field of physics, and for guiding and supervising me throughout the project. I would like give a special thanks to Leonardo Midolo who has inspired, supervised and helped me in every aspect of this work. His expertise, enthusiasm and attention to detail is inspiring, and I appreciate his dedication to my research project. The work presented in chapters 3 and 4 is a direct result of his creativity and expertise.

I would like to thank all current and former members of the research group, for developing the understanding and technical proficiency necessary to realize the experiments put forth in this thesis. I thank Weili Zhang for all his help in the lab when conducting the experiments presented in chapter 3. I would like to thank the whole Sparrow Quantum team for their collaboration on the work presented in chapter 4. A special thanks to Immo Söllner and Alisa Javadi who were the driving forces behind the work presented in chapter 5. Thank you for the fruitful discussions and valuable lessons.

Aside from the pull of the intriguing experiments waiting for me in the basement of the institute, the rest of the Quantum Photonics members have made it a pleasure to come here every day.

I would like to thank Morten Krabbe for his continuous support through all the years. Last but not least, I thank my daughter Petra, who was born midway through my PhD. She has been a great source of distractions, and having her taught me how to be focused and efficient.

Abstract

Quantum dots in photonic nanostructures has long been known to be a very powerful and versatile solid-state platform for conducting quantum optics experiments. The present PhD thesis describes experimental demonstrations of single-photon generation and subsequent manipulation all realized on a gallium arsenide platform. This platform offers near-unity coupling between embedded single-photon emitters and a photonic mode, as well as the ability to suppress decoherence mechanisms, making it highly suited for quantum information applications.

In this thesis we show how a single-photon router can be realized on a chip with embedded quantum dots. This allows for on-chip generation *and* manipulation of single photons. The router consists of an on-chip interferometer where the phase difference between the arms of the interferometer is controlled electrically. The response time of the device is experimentally shown to be in the sub-microsecond range.

The performance of the device is limited by the reflections from the out-coupling gratings used, and we thus developed a new type of out-coupler that reduces reflections as well as increases the coupling efficiency to the fiber. The grating design is inspired by a well-known design from silicon photonics and is adopted for quantum dot emission wavelengths. The new gratings offer a fivefold increase in efficiency compared to the gratings used previously. These results are found from simulations as well as transmission measurements and have recently been confirmed in single-photon experiments.

Lastly, an examination of some of the possible applications of quantum dots efficiently coupled to the propagating mode of a photonic crystal waveguide is presented. Specifically, we describe how we can realize propagation-direction-dependent light-matter interactions in engineered nanostructures, and how we can utilize a well coupled quantum dot to realize giant nonlinearities at the single-photon level.

Resumé

Man har længe vidst at kvantepunkter i fotoniske nanostrukturer udgør en vigtig og alsidig platform for udførelsen af kvanteoptiske eksperimenter. Denne PhD afhandling beskriver eksperimentelle demonstrationer af enkelt-foton udsendelse og efterfølgende manipulation, altsammen realiseret i en gallium arsenid platform. Det er muligt at koble enkelte fotoner udsendt fra indlejrede kvantepunkter, til en fotonisk modus med næsten 100 % effektivitet. Yderligere muliggør denne platform at undertrykke dekoheræns processer, hvilket gør den specialt attraktiv i forbindelse med processering af kvante information.

I denne afhandling vil vi vise hvordan en enkelt-foton router kan fremstilles på en chip med indlejrede kvantepunkter. Dette muliggør udsendelse *og* manipulation af enkelte fotoner på én og samme chip. Routeren består af et interferometer hvor fase-forskellen mellem de to arme kan kontrolleres vha. spænding. Eksperimenter viser at routerens respons-tid er mindre end et micro-sekund.

Reflektioner fra de cirkulære udkoblere begrænser routerens ydeevne, og derfor udvikler vi en ny type udkobler der reducerer reflektioner og øger koblingseffektiviteten til en optisk fiber. Designet er kendt fra silicium fotonik, og er tilpasset den bølgelænge kvantepunkter typisk udsender ved. Den nye type udkobler er fem gange så effektiv som de cirkulære udkoblere brugt tidligere. Dette er vist i transmissions målinger og er for nylig blevet bekræftet i eksperimenter med enkelte fotoner.

Slutteligt har vi undersøgt mulige anvendelser af kvantepunkter koblet til en fotonisk krystal bølgeleder. Vi beskriver hvordan vi kan realisere propagationsretnings-afhængige vekselvirkninger mellem lys og stof i specielt designede krystal bølgeledere og hvordan vi, ved hjælp af et vel-koblet kvantepunkt, kan opnå ikke-lineariteter på enkelt-foton niveau i en fotonisk krystal bølgeleder.

List of Publications

The work performed during this Ph.D.-project has resulted in the following publications:

Journal Publications

- I. Söllner, S. Mahmoodian, **S. Lindskov Hansen**, L. Midolo, A. Javadi, G. Kiršanskė, T. Pregnolato, H. El-Ella, E. H. Lee, J. D. Song, S. Stobbe, and P. Lodahl, "Deterministic photon-emitter coupling in chiral photonic circuits", Nat. Nanotechnol. 10, 775–778 (2015)
- A. Javadi, I. Söllner, M. Arcari, **S. Lindskov Hansen**, L. Midolo, S. Mahmoodian, G. Kiršanskė, T. Pregnolato, E. H. Lee, J. D. Song, S. Stobbe, and P. Lodahl, "Single-photon non-linear optics with a quantum dot in a waveguide", Nat. Commun. 6, 8655 (2015)

Journal publications in preparation

- Leonardo Midolo, **Sofie L. Hansen**, Weili Zhang, Camille Papon, Rüdiger Schott, Arne Ludwig, Andreas D. Wieck, Peter Lodahl, Søren Stobbe, "Electro-optic routing of photons from single quantum dots in photonic integrated circuits". Submitted to Optica

Contents

Chapter 1

Introduction

The emergence of quantum mechanics in the first part of the last century, forced us to drastically revise our understanding of nature. The development was largely initiated by Max Planck's suggestion of quantized radiation, leading to a wave-particle duality of light [1]. The formulation of both the photoelectric effect in 1905 [2], and the atomic model from 1913 [3] relies heavily on the notion of quantization. De Broglie generalized the wave-particle duality to matter itself [4], Heisenberg [5] and Schrödinger [6] came up with mathematical formulations of quantum mechanics, while the probabilistic interpretation was first described by Born, who introduced the idea of probability amplitudes. The new theory had profound philosophical implications for our understanding of physical reality, exemplified in particular in the acclaimed discussions between Niels Bohr and Albert Einstein [7, 8]. Aside from the philosophical discussions spurred by this new understanding of nature, the theory of quantum mechanics has provided the insight necessary to develop the fields of solid-state physics and quantum optics.

Quantum optics is the study of the nature of light treated as quantized entities known as photons. Over the last twenty years, four Nobel prizes have been awarded for work in quantum optics[1], signifying the outstanding contributions made within this field.

Since the burgeoning of the field of solid-state physics in the middle of the 20th century, it has experienced a tremendous technological revolution. The discovery of the transistor in the late 1940s [9], led to a miniaturization of integrated circuits, and subsequently we have experienced an exponential increase in the density of transistors in integrated circuits as predicted by Moore's law [10]. The ultimate

[1] In 2012: Serge Haroche and David J. Wineland. In 2005: Theodor W. Häsch, Roy J. Glauber and John L. Hall. In 2001: Wolfgang Ketterle, Eric A. Cornell and Carl Wieman, and in 1997: Steve Chu, Claude Cohen-Tannoudji and William D. Phillips.

limit is to have a single two-level system, e.g., the spin-states of an electron or energy states of an atom, act as a transistor. In this case we have entered the realm of quantum computing, where the internal state of the bit is no longer restricted to be either 0 or 1, but can exist in a superposition of the two allowed states: $\Psi = \alpha |0\rangle + \beta |1\rangle$. These quantum mechanical bits are known as qubits, and the generation and manipulation of these, is at the heart of quantum information science, which holds great promise for increasing the efficiency of certain computational tasks such as factoring large numbers [11] and searching large data-bases [12]. Using quantum key distribution, communication may become unconditionally secure [13], and quantum metrology utilizes quantum mechanics to reduce statistical errors in measurements [14, 15]. Finally, quantum systems may be used in simulations as proposed by Richard Feynman in the early 80's [16].
The great advantage lies in the unique features of quantum mechanics, namely superposition and entanglement. In order to harvest this advantage we must be able to generate qubits as well as realize quantum gates and efficient detection schemes. To this end, several systems have been proposed. The use of photons as qubits is a promising candidate for encoding and transmitting quantum information. The advantage of using photons is their low decoherence and high-speed transmission making them suited for transmission over long distances. A major disadvantage of this system is the weak photon-photon interactions, making any two-qubit gate very demanding [17, 18]. Strong interactions may be realized in trapped electrons making this system suited for information processing. However, this system is prone to decoherence and the achievable interactions have limited spatial range [19]. An interface that offers the best of both worlds is expected to find a wide range of applications in quantum information processing [20]. Such an interface can be found at the intersection between solid-state physics and quantum optics. The field of quantum photonics investigates the quantum interactions between light and semiconductor materials, and offers a platform for a highly-efficient light-matter interface.

In chapter 2 we present a theoretical background, introducing the electronic and optical properties of self-assembled Gallium Arsenide (GaAs) quantum dots. A brief introduction to single-photon routing is presented including an overview of a selection of available tuning-strategies. Lastly a summary of out-coupling strategies is presented.
In chapter 3 we present an experimental demonstration of a reconfigurable beam splitter, based on the electro-optic effect in GaAs. Simulations of the device reveal what limits the performance, and points towards the importance of implementing a different out-coupling strategy that reduces back-reflections into the structure. Chapter 4 presents the development of a new type of grating-coupler, specifically designed to reduce back-reflections and increase fiber-coupling at $\sim 930\,\mathrm{nm}$. We start with numerical simulations to optimize the design, and finally test the design

experimentally.
In chapter 5, we present two experiments that highlight the rich physics associated with quantum dots coupled to photonic crystal waveguides. The first part of the chapter presents a chiral light-matter interface, and point to a possible application that necessitates a reconfigurable beam splitter such as the one presented in chap. 3. The second part of the chapter gives an introduction to single-photon nonlinearities, and demonstrates how photon-photon interactions can be mediated by matter in a 1D atom.

Chapter 2

Theoretical background

The number of proposals for a platform for quantum information processing [21, 22, 23, 24] is a testament to the applicability as well as the intriguing and challenging physics underlying it.
Here we present one such platform based on III-V semiconductor materials, more explicitly InAs quantum dots embedded in circuits defined on GaAs. The mature fabrication technologies combined with the optical and electrical properties of the material, makes this platform suited for the development of quantum information processing.

2.1 Quantum dots as single-photon sources

A quantum dot is a 0-dimensional system that confines charge carriers to a point[1]. Confinement in all three spatial directions leads to discretized energy levels in the quantum dot. By analogy with atoms, quantum dots can be excited and will subsequently decay radiatively emitting a single quantum of light, a photon.

2.1.1 Self-assembled quantum dots

One way of realizing quantum dots is to embed InAs into bulk GaAs. This can be achieved by means of molecular-beam epitaxy, which is a thin-film deposition method. Due to the 7 % larger lattice constant of InAs compared to GaAs, the accumulated strain in the InAs is released by spontaneous nucleation after deposition of some monolayers of InAs on the GaAs substrate. This growth method is known

[1] We talk about quantum confinement when the diameter of confinement is comparable to the de Broglie wavelength $\Delta x \leq \lambda_{\mathrm{deB}}$ [25]

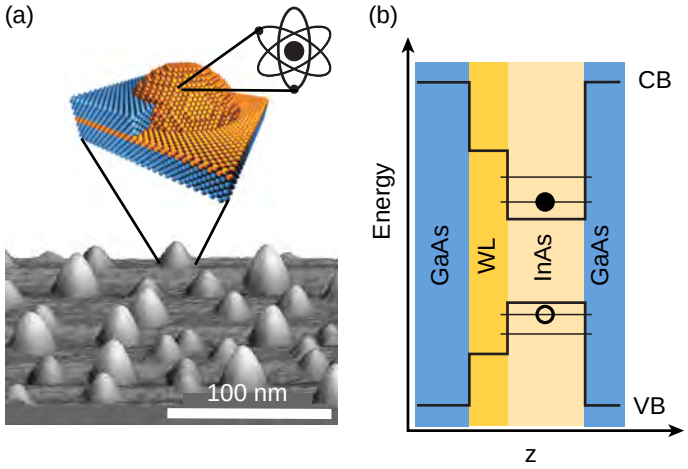

Figure 2.1: Self-assembled quantum dot: (a): Top: Schematic of a self assembled quantum dot, where InAs (yellow) is encapsulated in GaAs (blue). Bottom; a transmission electron microscopy (TEM) image of InAs quantum dots grown on a GaAs substrate (Institute for Microstructural Sciences, NRC, Cananda) **(b):** Sketch of the energy band diagram of a quantum dot. The solid circle in the conduction band (CB) represents an electron, and the open circle in the valence band (VB) represents a hole. Figure reproduced from Ref. [29]

as the Stranski-Krastanov method [26] and quantum dots grown in this way are schematically illustrated in fig. 2.1(a). The spontaneously formed islands of InAs, are capped by GaAs, resulting in confinement in all three directions. The quantum dots form in random positions, and have varying sizes resulting in different emission energies. The typical in-plane size of the dots is 15-30 nm, and the height in the growth direction is usually around 3-5 nm [27, 28]. The few monolayers deposited before the formation of the InAs quantum dots act as a quantum well, and is called the wetting layer (WL). The energy of a quantum dot can be represented in a band diagram, which is a real-space projection of the band edge energies. Figure 2.1(b) shows the band diagram of a self assembled quantum dot along the growth direction z. By analogy with the single atom, the quantum dot has discrete energy levels, and may thus be used as a source of single photons. An electron (solid circle in fig. 2.1(b)) may be promoted from the valence band to the conduction band, leaving behind a hole. The two attract each other via the Coulomb interaction and form a bound state called an exciton, which upon recombination emits a photon [30].

2.1.2 Excitons in quantum dots

The electron and hole are fermions of half-integer total angular momentum, $j = l+s$, where l is the orbital angular momentum, and s is the spin. The spin structure of the electrons and holes confined in the quantum dot are inherited from the bulk semiconductor. The total angular momentum of an electron in the conduction band j, and its projection along the growth direction m_j is: $|j = 1/2, m_j = \pm 1/2\rangle$. The heavy-holes in the valence band have $|j = 3/2, m_j = \pm 3/2\rangle$. This leads to

four possible spin-state combinations where $\Delta j = \pm 1$ or $\Delta j = \pm 2$. Only the recombinations where $\Delta j = \pm 1$ are allowed as photons carry angular momentum ± 1, and this exciton doublet is called bright, while the $\Delta j = \pm 2$ doublet is called dark. The electron-hole exchange interaction is responsible for lifting the degeneracy between the bright and dark states, as well as altering the polarization of the emitted photons from the bright states from circular to linear, X and Y. The fine structure splitting between the X and Y states are on the order of few tens of µeV, while the energy splitting between the bright and dark states is on the order of few hundred µeV [31, 32]. The resulting level-scheme is illustrated in fig. 2.2(a). The bright excitons are; $|X_b\rangle = 1/\sqrt{2}(|\Uparrow\downarrow\rangle - |\Downarrow\uparrow\rangle)$ and $|Y_b\rangle = 1/\sqrt{2}(|\Uparrow\downarrow\rangle + |\Downarrow\uparrow\rangle)$, where $\Uparrow$ and $\Downarrow$ denotes hole spin states, while $\uparrow$ and $\downarrow$ denotes electron spin states. The dark excitons are: $|X_d\rangle = 1/\sqrt{2}(|\Uparrow\uparrow\rangle - |\Downarrow\downarrow\rangle)$ and $|Y_d\rangle = 1/\sqrt{2}(|\Uparrow\uparrow\rangle + |\Downarrow\downarrow\rangle)$. The bright excitons may decay to the ground state, $|0\rangle$, radiatively at a rate γ_{rad}, accompanied by the emission of a single photon. This is illustrated by the red dashed line in fig. 2.2(a). All the transitions may decay non-radiatively at rates γ_{nrad}, and spin flip processes couples the bright and dark excitons at a rate γ_{sf}. We neglect double or higher order spin flip-processes as they are strongly inhibited in quantum dots as compared to bulk or quantum wells [33].
When the exciton is in the bright state (fig. 2.2(d)), it may decay directly. If it is in the dark state (fig. 2.2(e)), it may only decay by first undergoing a spin-flip. This leads to a bi-exponential decay of the exciton population

$$\rho(t) = A_{\text{f}} \cdot \exp(-\gamma_{\text{f}} t) + A_{\text{s}} \cdot \exp(-\gamma_{\text{s}} t), \tag{2.1}$$

where the fast rate is the sum of the radiative and non-radiative decay rates, $\gamma_{\text{f}} = \gamma_{\text{rad}} + \gamma_{\text{nrad}}$, the slow rate is the sum of the non-radiative and the spin-flip rate $\gamma_s = \gamma_{\text{nrad}} + \gamma_{\text{sf}}$, and $A_{\text{f(s)}}$ are the corresponding amplitudes. Fitting experimental decay curves to bi-exponential model of eq. (2.1) allows us to extract information about the radiative, non-radiative and spin-flip rates. These rates can then be used to gain information about the local light-matter interaction. Figure 2.2(b) illustrates Pauli filling of the lowest energy level, with two electrons and two holes forming a bi-exciton. The bi-exciton decays to one of the neutral exciton states, before decaying to the ground state. Another example of multiexcitonic states is that of trions. Trions consist of two antisymmetric identical carriers, and one carrier of the opposite charge, i.e., two holes and an electron (X^+) or two electrons and a hole (X^-). The decay of a trion to a single electron or hole is accompanied by a circularly polarized photon, where the orientation depends on the spin of the additional carrier, which can be prepared in an eigenstate, making trions particularly interesting for spin-physics [34]. Figure 2.2(c) shows the negative trion where the additional electron is in the $|\uparrow\rangle$ or $|\downarrow\rangle$ state. The grey lines indicate the "forbidden" transitions, arising as a result of the in-plane magnetic field from the nuclear spins inside the quantum dot [35]. A magnetic field in the growth direction of the quantum dots leads to an energy-splitting between the two states.

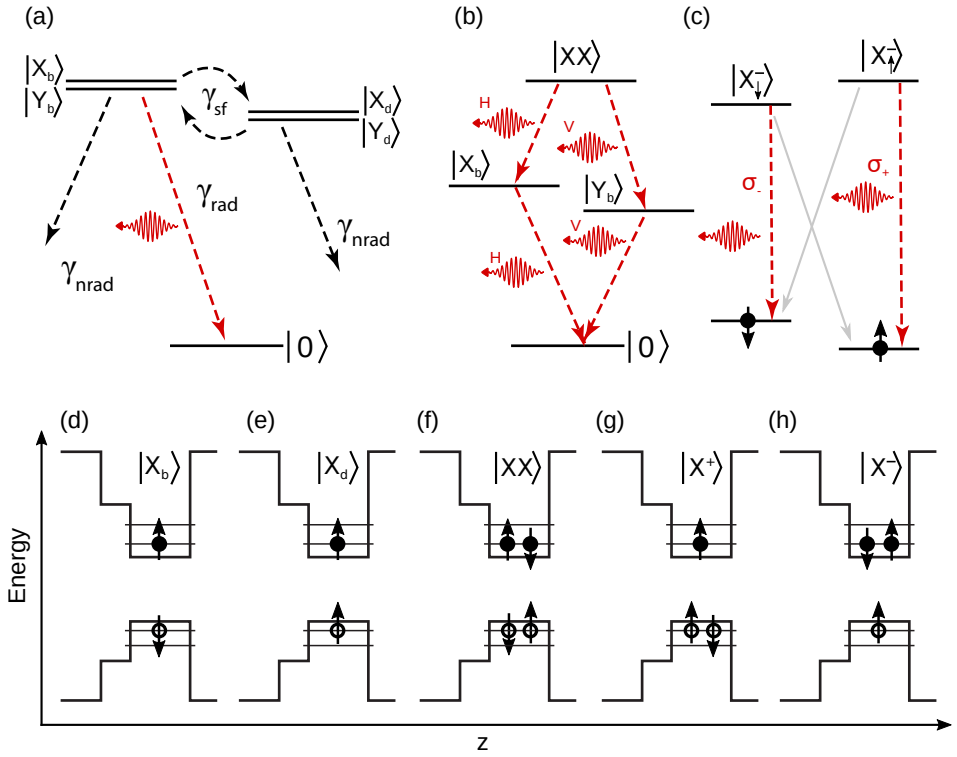

Figure 2.2: Decay dynamics of quantum dots: (a): Level scheme of a quantum dot where the bright states, $|X_b\rangle$ and $|Y_b\rangle$, can decay radiatively at a rate γ_{rad}. The bright states are coupled to the dark states, $|X_d\rangle$ and $|Y_d\rangle$, via spin-flip processes that occur at a rate of γ_{sf}. The degeneracy between the X and Y components of the bright and dark states is lifted due to the exchange interaction. The bright and dark states can both decay non-radiatively at a rate γ_{nrad}. **(b)**: Four-level scheme depicting the bi-exciton level, the two bright exciton levels and the ground state. The bi-exciton will decay through a cascade process. **(c):** Negative trions in the presence of an out-of-plane magnetic field. The emitted photons are circularly polarized with the orientation depending on the spin of the additional carrier. **(d)-(h):** Possible excitonic complexes in a quantum dot: The bright exciton $|X_b\rangle$, the dark exciton $|X_d\rangle$, the bi-exciton $|XX\rangle$, the positively charged trion $|X^+\rangle$, and the negatively charged trion $|X^-\rangle$.

2.1.3 Quantum dots in nanophotonic waveguides

Quantum dots in nanophotonic waveguides serve as a powerful platform for dramatically enhancing light-matter interactions. It was recently demonstrated that a quantum dot in a photonic crystal waveguide emits more than 98 % of the emitted photons into the propagating mode of the waveguide as quantified by the β-factor [36]. Furthermore, quantum dots in bulk have been experimentally shown to emit transform-limited single photons [37]. Quantum dots sitting in a nanobeam waveguide have also been demonstrated to emit single photons with a very high degree of indistinguishability [38, 39], which is a key ingredient in quantum information processing [40]. The main source of decoherence, is coupling to phonons [41] and jittering introduced in the relaxation process in non-resonant excitation [42].
Low loss waveguiding have been reported in rib- [43] and ridge-waveguides [44]. When integrated with quantum dots, the rib- and ridge-type waveguides are not suited as the emission leaks into the substrate, necessitating fully suspended waveguides. Suspended nanobeam waveguides offer good mode confinement and β-factors up to 95 % are achievable [45].
The fabrication of suspended waveguides involves patterning of the waveguides on a 550 nm-thick ZEP520 electron beam resist layer spin-coated on the GaAs membrane surface at 2000 rotations per minute (rpm), and baked for 5 minutes on a hot plate. The pattern is defined using a 100 kV electron-beam lithography tool (Elionix ELS-7000G) and developed for 1 minute at 22°C in n-amylacetate. Subsequently the structure is etched in a reactive ion etching (RIE) tool (Plasmalab 100) from Oxford Instruments that has an inductively coupled plasma source. When the pattern is defined on the membrane, the sample is bathed in hydrofluoric acid for 45 seconds to remove the sacrificial layer consisting of an $Al_xGa_{1-x}As(x = 0.75)$ layer below the GaAs membrane. This leaves suspended structures that can be used to guide light from embedded quantum dots. More information on the fabrication of GaAs nanomembranes can be found in Ref. [46]. The planar technology of suspended nanobeam waveguides allows for integration of single-photon sources with in-plane photonic circuits.

2.2 Single-photon routing

It is a tremendous achievement that the decoherence processes can be overcome to the extent that near-unity indistinguishability between photons emitted from the same quantum dot is obtainable [38, 39]. However, the photons are emitted one after the other, and the next step is convert this string of photons into a demultiplexed state with many identical photons in individual modes as illustrated in fig. 2.3.

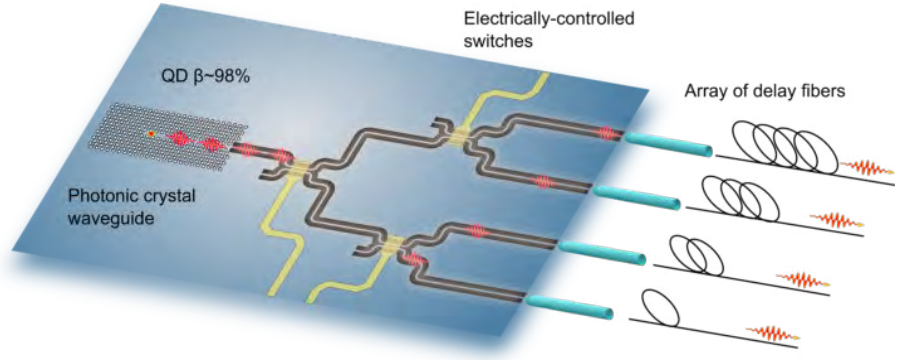

Figure 2.3: A single-photon demultiplexing scheme using on-chip routers: A quantum dot in a photonic crystal waveguide emits photons into the propagating mode of the waveguide with an efficiency β of 98%. These photons are emitted at a frequency determined by the pumping laser. Electrically controlled switches route the photons to paths with different delay lines, ensuring a state with N (in this case 4) indistinguishable photons emerging from the fibers. This figure is a courtesy of Dr. L. Midolo.

2.2.1 Efficiency requirement

The realization of a de-multiplexed $(N\times1)$-photon state, with N spatially separated identical photons, is a key ingredient in quantum information processing, quantum simulation or boson sampling [47, 48]. Integration of single-photon sources, waveguides and passive beam splitters has been demonstrated [49, 50]. However, in order to boost the efficiency of the circuits, the networks must be dynamically reconfigurable and therefore reconfigurable networks are sought after, and are being developed in various ways on different platforms [51, 52, 53, 54, 55]. Many quantum information algorithms require an $(N \times 1)$-photon state, and we thus need a dynamically tunable optical switch that can be implemented on the same platform as the photon generation. With such a device one could route subsequently emitted photons into paths with different delays resulting in an $(N \times 1)$-photon state. This is illustrated in fig. 2.3, where a quantum dot emits single indistinguishable photons at a repetition rate set be the driving laser. These photons are then routed into different spatial modes by electrically controlled switches resulting in an $(N \times 1)$-photon state. The performance of such a device relies heavily on the efficiency with which photons are routed from the source to one of the N outputs. An $(N \times 1)$-photon state requires $(N - 1)$ switches, and each photon will have to be switched $\log_2 N$ times, where $N = 2^n$, n being an integer. Assuming that all the paths have the same transmission efficiency from the source to the fiber: η, then the probability of successfully generating an $(N \times 1)$-photon state scales as η^N, where $\eta = \kappa^{\log_2 N}$. Here κ is the efficiency of the individual switch, defined as the probability with which it routes an incoming photon to the desired output port. The probability of successfully generating an $(N \times 1)$-photon state can be

calculated as

$$P_{(N\times1)}(\kappa) = \eta(\kappa)^N = (\kappa^{\log_2 N})^N. \tag{2.2}$$

Consequently, the rate at which an $(N\times1)$-photon state is generated is given by [56]

$$R_{(N\times1)}(\kappa) = \frac{R_p \times \eta^N}{N}, \tag{2.3}$$

where R_p is the repetition rate of the laser. As an example; if the switch-efficiency of each switch is 75 %, then we can generate an (8×1)-photon state with probability of 0.1 %. If we use a laser with a repetition-rate of 80 MHz, then we generate the (8×1)-photon state at a rate of $\sim$ 10 kHz.

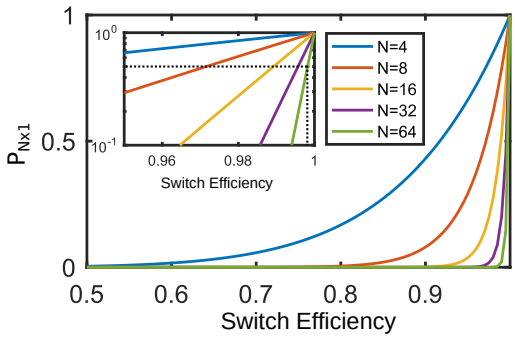

Figure 2.4: De-multiplexing efficiency as a function of switch efficiency: The inset shows a zoom-in of the high-κ region. The horizontal dotted line indicates 50 % success probability. The vertical dotted line indicates the required switch efficiency to achieve a 50 % success probability to generate a 64-photon state.

$P_{(N\times1)}(\kappa)$ for five different values of N is shown in fig. 2.4. This graph ignores any other loss channels associated with the circuit, and only considers the effect of the efficiency of the switches.

The inset illustrates that switch-efficiencies above 99.8 % are required to generate a 64-photon state with more than 50 % probability. For switch efficiencies below 80 % the probability to generate even an $N = 4$ photon state is less than 20 %. Aside from the efficiency requirement, the switching platform will also have to be scalable. The realization of a highly efficient and scalable switching device is thus a daunting task, and many switching methods have been proposed.

2.2.2 Switching methods

Some switching methods involve active phase-tuning, whereas others involve mechanical tuning. Two important figures of merit related to switches is the product of the switching voltage, i.e., the voltage required to realize a π-phase shift, and the length of the device: $V_\pi L$, and the response time of the switch. In the following,

a brief overview of the available methods is presented along with an evaluation of their applicability in the experiments described in this thesis.

Thermo-optic tuning

When the temperature of a material is changed, the crystal structure tends to shrink or expand, which imparts a change of the refractive index, n, of the material. This phenomenon is known as the thermo-optic effect. In semiconductors, dn/dT values are usually on the order of $\sim 10^{-4}\mathrm{K}^{-1}$ [57].

The thermo-optic effect can be used to dynamically change the refractive index in a Mach-Zehnder-Interferometer (MZI), and can thus be used as a means to route light between two outputs [58, 59]. The effect is fast, and switching speeds in the µs range have been demonstrated in silicon [60, 61]. The thermal control may be realized by tightly focusing a high-power laser to the sample [62, 63], or by having micro-heaters built into the circuit [60, 61, 64].

Thermo-optic tuning offer large tuning ranges at low power [61]. However, the thermal expansion coefficient is negligible at cryogenic temperatures [65], making this approach unsuited for experiments involving quantum dots, as the elevated temperatures will lead to excessive noise in the quantum dot spectra.

Free-carrier injection

A temporary change of the refractive index may also be realized by injecting free carriers in a semiconductor [66]. The introduction of free carriers causes a bandgap shrinkage, bandfilling and free-carrier absorption. Below the bandgap of the material, the free-carrier absorption is dominant and leads to a negative shift of the refractive index. The carriers may be injected through doped layers or optically with light pulses. For moderate concentrations of the injected carriers, the resulting change in refractive index is proportional to the concentration [67]. This approach is potentially very fast, only limited by the carrier recombination time as was demonstrated in a GaAs/AlGaAs microring resonator [68] and a GaAs cavity [69].

Free carrier injection offers fast operation and compact devices, however this approach is not compatible with integrated quantum dots as the generated carriers may recombine in the quantum dots [70].

Mechanical tuning

A promising alternative for phase tuning is the physical displacement of of micro- or nano-mechanical structures, where the displacement is realized via electrical actuation such as capacitive forces. These systems, known as micro/nano-electro-mehanical systems (MEMS/NEMS), have gained a lot of attention recently, as they offer a compact platform for controlling light propagation, and thus offer a way of realizing on-chip photonic switches.

Recently, a 64×64 silicon photonic switch was realized employing MEMS-actuated vertical couplers [52]. The coupling ratio of a directional-coupler may be tuned by

electro-mechanically changing the distance between the two suspended waveguides, which provides a way of routing light between two outputs. The coupling of optical, electrical and mechanical degrees of freedom in nanoscale devices is a rapidly developing field, and more information about these Nano-Opto-Electro-Mechanical systems (NOEMS) may be found in Ref. [71].
Mechanical tuning offers very compact devices with low actuation voltages, i.e., low $V_\pi L$. It can be used at cryogenic temperatures and does not adversely affect embedded quantum dots. The drawback of these mechanical systems is the maximally attainable frequency which is expected to be in the MHz range [72].

Electro-optic tuning
Another option is to change the refractive index by means of an applied electric field. In anisotropic materials, the change in the refractive index is proportional to the applied field. This effect is known as the linear electro-optic or Pockels effect. The electro-optic effect is potentially very fast, and offers low switching voltages and compact devices. Values of $V_\pi L$ as low as 0.21 V cm have been demonstrated in GaAs in the past [73].
The electro-optic effect is potentially fast, the switches may be very compact and the switching voltage required is low. Finally the effect is present at cryogenic temperatures in GaAs [74] and is thus suited for experiments involving switching of single-photons from integrated quantum dots. However, the Pockels effect is not the only effect of applying an electric field across a GaAs membrane with integrated quantum dots. The presence of an electric field causes a change in the optical absorption close to the band edge of the material due to a distortion of the electron and hole wavefunctions. This effect was first observed in 1958 by W. Franz and L. Keldysh, and is known as the Franz-Keldysh effect [75, 76, 77].
Applying an external electric field across a quantum dot in the growth direction will cause the emission energy to tune proportional to the applied field strength as the bands are tilted and the overlap-integral between the electron- and hole wavefunctions is reduced. This effect is known as the quantum confined Stark effect [78]. Lastly, an applied electric field has the advantageous effect of minimizing spectral wandering of the quantum dot by stabilizing the charge environment of the emitter [79, 80, 81].

Electrically controlled routing of photons from an InAs/GaAs self-assembled quantum dot has been demonstrated [55]. The architecture presented in Ref. [55] offers low-power and high-speed operation, however it is not suited for multiplexing schemes as the functionality relies on the tuning of the quantum dot, rather than a change in the refractive index. In chapter 3 we present an experimental demonstration of on-chip electro-optic routing, where the emission-energy of the quantum dots is independent of the electric field used to realize the phase-tuning. We achieve a $V_\pi L = 0.1\,\mathrm{V\,cm}$, and sub-microsecond response time.

2.3 Chip-to-fiber coupling

The challenge of coupling single photons off chip can be dealt with in numerous ways. One strategy is to employ a system where the photons are emitted directly upwards such as in micropillar structures illustrated in fig. 2.5(a) [82, 83]. The drawback of this approach is that it does not immediately allow for on-chip manipulation of the emitted photons.
The feasibility of on-chip manipulation combined with emitter-waveguide coupling exceeding 98 % [36], a high degree of indistinguishability ($\sim 86\,\%$) and single photon purity ($> 99.4\,\%$) of photons emitted from quantum dots sitting in suspended nanobeam waveguides [38], makes the planar technology very attractive for photonic quantum information processing. A main challenge is the efficient out-coupling of photons from the planar structure and into an optical fiber. This is because of the mode-mismatch between the mode of the fiber and the sub-wavelength mode of the nanobeam waveguides. One strategy is to use end-fire coupling from a tapered waveguide to a lensed fiber as illustrated in fig. 2.5(b) [86, 84]. The mode matching condition is met by adiabatically tapering the waveguide along the propagation direction. This method has a theoretical efficiency of $\sim 80\,\%$, but has the drawback, that it restricts the structures to the edge of the phonic chips and it requires very long tapers to fulfil the adiabatic condition . Another option, illustrated in fig. 2.5(c), is to use evanescent coupling of the light field from a tapered nanobeam waveguide to a dimpled fiber. This approach has been demonstrated to offer a chip-to-fiber coupling efficiency exceeding 80 % [85]. This method of out-coupling is not restricted to the edge of the sample, but the setup is complex, and requires specially fabricated dimpled fibers.
Yet another option is to use surface grating couplers that scatters the light travelling in the plane upwards due to diffraction. An example of a surface grating coupler is the second order Bragg grating [63]. These gratings have efficiencies of $\sim 7\,\%$ [87] due to poor mode-matching to the optical fiber mode. Furthermore this type of gratings reflect light back into the structure leading to unwanted Fabry-Perot resonances, that may have detrimental effects on the performance of the on-chip devices. Chapter 4 presents a description of the design and characterization of a shallow-etched grating coupler that outperforms the second order bragg gratings in terms of increased chip-to-fiber coupling, and reduced backscattering into the waveguide. An SEM image is shown in fig. 2.5(d). The design is well known from silicon photonics where simulations predict coupling efficiencies between 80 and 95 % [88]. The design is adapted to the suspended membrane architecture, and for a working wavelength of 930 nm, which is the emission wavelength of the InAs quantum dots used in this work.

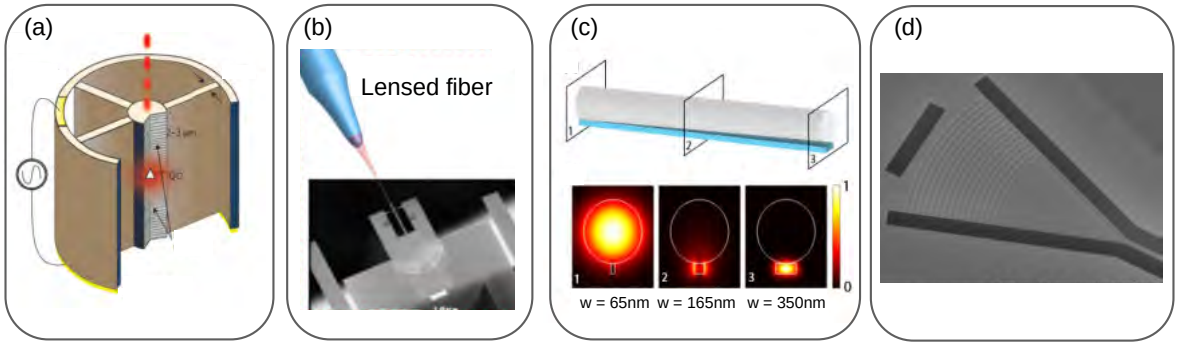

Figure 2.5: Out-coupling strategies: (a): Single quantum dot in a vertical micropillar cavity. The extraction efficience is experimentally determined to be $\sim 65\,\%$. The figure is reproduced from Ref. [82]. **(b):** End-fire coupling from a $7\,\mu\mathrm{m}$ long tapered waveguide to a lensed fiber. The figure is reproduced from Ref. [84]. **(c):** Evanescent coupling from a tapered out-coupler to a dimpled optical fiber. The electric field is coupled from the fiber-mode to the waveguide-mode as the width of the waveguide is increased. The figure is reproduced from Ref. [85]. **(d):** SEM of a shallow-etched grating fabricated on a suspended GaAs membrane. The trenches around the grating ensures a full undercut of the membrane.

Chapter 3

On-chip electro-optic routing

3.1 Introduction

This chapter describes the experimental realization of electro-optic routing in a photonic circuit with integrated quantum dots. The routing is actuated electrically without tuning the emitters, making the approach suitable for multiplexing schemes. Part of the results presented here have been submitted for publication in a peer-reviewed journal [89].

3.2 Device principles

3.2.1 The electro-optic effect in gallium arsenide

The derivation presented here follows that of Refs. [25, 90].
Applying an electric field to an anisotropic material will result in a dependence of the polarization on the direction of the field relative to the crystal axes. This can be included in the description of the relation between the polarization and the field, by replacing the dielectric susceptibility, χ, in $\mathbf{P} = \epsilon_0 \chi \mathbf{E}$ by the a dielectric susceptibility tensor, $[\chi]$, and we can write the relation between the polarization and the field including the direction dependence as

$$\begin{bmatrix} \mathbf{P}_x \\ \mathbf{P}_y \\ \mathbf{P}_z \end{bmatrix} = \epsilon_0 \begin{bmatrix} \chi_{xx} & \chi_{xy} & \chi_{xz} \\ \chi_{yx} & \chi_{yy} & \chi_{yz} \\ \chi_{zx} & \chi_{zy} & \chi_{zz} \end{bmatrix} \begin{bmatrix} \mathbf{E}_x \\ \mathbf{E}_y \\ \mathbf{E}_z \end{bmatrix}. \tag{3.1}$$

From $[\chi]$ we may define a tensor for the dielectric constant: $[\epsilon] = \epsilon_0\{1 + [\chi]\}$, and the relative dielectric constant: $[\epsilon_r] = \{1 + [\chi]\}$. From the principle of energy conservation it can be shown that the dielectric tensor must be symmetric, i.e., $\epsilon_{ij} = \epsilon_{ji}$.

A consequence of the direction dependent polarization is that the phase velocity of waves propagating in an anisotropic material, will also depend on the orientation of the electric field vector relative to the crystal axes. A geometrical interpretation of propagation in an anisotropic material is given by the index ellipsoid. We start by considering the energy density associated to an electromagnetic wave: $U = \frac{1}{2}\mathbf{E}\cdot\mathbf{D}$, where $\mathbf{D} = \epsilon_0[n^2]\mathbf{E}$. From this we can write the energy density as

$$2U = \frac{\mathbf{D}_{xx}^2}{\epsilon_0 n_{xx}^2} + \frac{\mathbf{D}_{yy}^2}{\epsilon_0 n_{yy}^2} + \frac{\mathbf{D}_{zz}^2}{\epsilon_0 n_{zz}^2} + \frac{2\mathbf{D}_x\mathbf{D}_y}{\epsilon_0 n_{xy}^2} + \frac{2\mathbf{D}_y\mathbf{D}_z}{\epsilon_0 n_{yz}^2} + \frac{2\mathbf{D}_z\mathbf{D}_x}{\epsilon_0 n_{zx}^2}, \tag{3.2}$$

where we have used the symmetry of the dielectric tensor to combine terms. This can be rewritten by introducing the substitution, $\frac{\mathbf{D}_{xx}^2}{2\epsilon_0 n_{xx}^2 U} = x^2$ and so on, yielding

$$\frac{x^2}{\epsilon_{rxx}} + \frac{y^2}{\epsilon_{ryy}} + \frac{z^2}{\epsilon_{rzz}} + \frac{2xy}{\epsilon_{rxy}} + \frac{2yz}{\epsilon_{ryz}} + \frac{2zx}{\epsilon_{rzx}} = 1 \tag{3.3}$$

This equation describes an ellipsoid whose orientation in space is given by the off diagonal elements. In the case where the off-diagonal terms are zero, eq. (3.3) reduces to

$$\frac{x^2}{\epsilon_{rxx}} + \frac{y^2}{\epsilon_{ryy}} + \frac{z^2}{\epsilon_{rzz}} = 1, \tag{3.4}$$

and the ellipsoid is now oriented along the coordinate axes, and the semi-major-axes are given by the refractive index: $\sqrt{\epsilon_{rii}} = n_i$. In a uniaxial crystal the refractive index along two axes are equal, and the index ellipsoid becomes an ellipsoid of revolution, whose symmetry axis is called the optic axis.

The intersection between the ellipsoid and a plane, through the origin, normal to the propagation vector $\mathbf{k}$, is an ellipse from which the effective indices can be read off. The full ellipsoid is depicted in fig. 3.1, and the ellipse is shown in fig. 3.2(a).

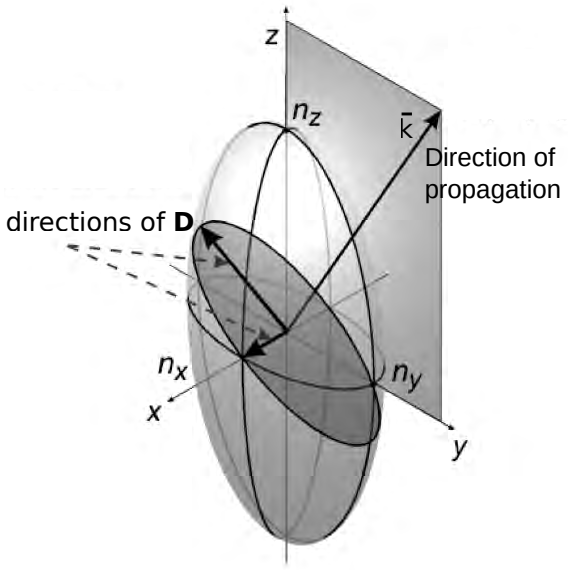

Figure 3.1: Index Ellipsoid: Illustration of an index ellipsoid or indicatrix. In this case the off diagonal terms in eq. (3.3) are zero, and the orientation of the ellipse is along the coordinate axis. Figure from: *http* : *//nicadd.niu.edu/piot/phys*630/*Lesson*14.*pdf*

We define an electro-optic coefficient tensor r_{ij} whose components determine the change in the refractive index when a field is applied

$$\Delta\left(\frac{1}{n^2}\right)_i \approx \sum_{j=1}^{3} r_{ij}E_j. \tag{3.5}$$

Due to symmetry, only the r_{41} term survives in the case of GaAs. We can write $\Delta\left(\frac{1}{n^2}\right) = -2\frac{\Delta n}{n^3} \approx r_{41}E$, which can be rearranged

$$|\Delta n| \approx \frac{1}{2} r_{41} n_0^3 E, \tag{3.6}$$

where n_0 is the index in the absence of a field E.
When a field is applied in the [001]-direction, the index along [110] and $[1\bar{1}0]$ is changed as follows

$$\begin{aligned} n[1\bar{1}0] &= n_0 - \frac{1}{2} n_0^3 r_{41} E = n_0 - \Delta n \\ n[110] &= n_0 + \frac{1}{2} n_0^3 r_{41} E = n_0 + \Delta n, \end{aligned} \tag{3.7}$$

The field thus induces birefringence. By applying a field in the [001]-direction, the refractive index along the $[1\bar{1}0]$-axis gets smaller by Δn, whereas the refractive index along [110] increases by Δn as indicated by the dashed line in fig 3.2(a).

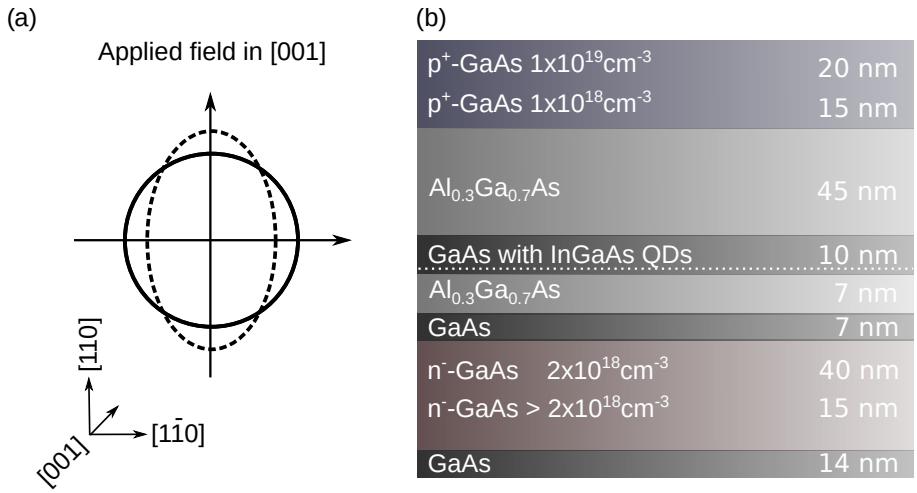

Figure 3.2: Ellipse and layer structure: (a): Index ellipse illustrating the effect of an electric field applied in the growth ([001])-direction. the solid line corresponds to zero applied field, while the dashed line shows the effect of an applied field; the refractive index is increased in the [110]-direction, while it is decreased in the $[1\bar{1}0]$-direction. **(b):** Layer structure of the wafer on which the device is fabricated.

The layer structure of the wafer is illustrated in fig. 3.2(b). The wafer was grown at Ruhr University Bochum in Germany by Rüdiger Schott. The wafer consists of a GaAs layer with embedded quantum dots surrounded by AlGaAs layers with an aluminum content of 30%. The AlGaAs layers form a barrier that prevents charge tunnelling from the doped layers when applying a forward bias [91]. The diode is formed by capping the intrinsic layer by a *p*- and an *n*-doped layer, forming a *p-i-n* junction with a depletion layer width of approximately 70 nm. The built-in voltage $V_{bi} \approx -1.4\,\mathrm{V}$ gives rise to an electric field of $\approx 20\,\mathrm{MV\,m^{-1}}$. This field can be reduced or increased by applying a forward or reverse bias, and the magnitude of the total electric field across the intrinsic layer is given by

$$E = \frac{V_{bi} - V}{d}, \tag{3.8}$$

where V is the applied voltage and d is the thickness of the intrinsic layer.

3.2.2 Device design

In order to utilize the electro-optic effect to route photons between two possible output ports, an on chip Mach-Zehnder interferometer (MZI) is designed.
A MZI routes photons to one of two outputs depending on the relative phase (ϕ) between the two arms.

By designing a MZI where the two arms of the interferometer are defined along the [110] and $[1\bar{1}0]$ directions of GaAs as illustrated in fig. 3.3, and allowing

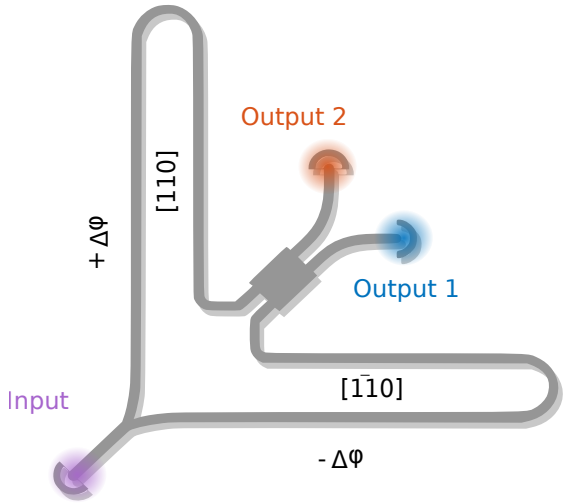

Figure 3.3: Schematic outline of the device: The interferometer consist of an initial power splitter followed by two arms aligned along the [110] and [1$\bar{1}$0] directions of the crystal respectively. The two arms are then combined on an MMI with two output ports. A field applied in the growth direction leads to a phase difference between the light propagating in the two arms, which results in an anti-correlated output at the two output ports.

for the application of an electric field in the [001]-direction, we can change the phase of the light propagating along the two arms and thus the interference at the two outputs. This can be understood by considering the photon propagation along the device. The effect of the initial power splitter is that of a 50:50 beam splitter. After propagation along the interferometer-arms, the photon will acquire a phase that depends on the path traversed. This can be written as

$$\frac{1}{\sqrt{2}}\left(e^{i\phi}\left|1\right\rangle\left|0\right\rangle + e^{-i\phi}\left|0\right\rangle\left|1\right\rangle\right) \tag{3.9}$$

where the phase ϕ depends on the change in the refractive index, the free-space wave number and the length of the path traversed; $\phi = |\Delta n| kL$. The state (3.9) is incident on the MMI that is similar to a 50:50 beam splitter. Hence

$$\begin{aligned}\left|1\right\rangle\left|0\right\rangle &\xrightarrow{\text{MMI}} \frac{1}{\sqrt{2}}\left(\left|1\right\rangle\left|0\right\rangle + i\left|0\right\rangle\left|1\right\rangle\right)\\ \left|0\right\rangle\left|1\right\rangle &\xrightarrow{\text{MMI}} \frac{1}{\sqrt{2}}\left(\left|0\right\rangle\left|1\right\rangle + i\left|1\right\rangle\left|0\right\rangle\right)\end{aligned} \tag{3.10}$$

Combining eqs. 3.9 and 3.10 yields a final state that can be written as

$$\frac{1}{2}\Big[e^{i\phi}(\left|1\right\rangle\left|0\right\rangle + i\left|0\right\rangle\left|1\right\rangle) + e^{-i\phi}(\left|0\right\rangle\left|1\right\rangle + i\left|1\right\rangle\left|0\right\rangle)\Big]. \tag{3.11}$$

From this we see that the probability of the photon leaving from port 1 and 2

respectively, is given by

$$P_1 = \frac{1}{2}(1 + \sin(2\phi))$$
$$P_2 = \frac{1}{2}(1 - \sin(2\phi)), \tag{3.12}$$

Hence the probability of the photon exiting the device from port 1 and 2 oscillate out of phase, and we can thus route the light to either of the outputs by changing the phase difference between the light propagating along the arms of the interferometer.

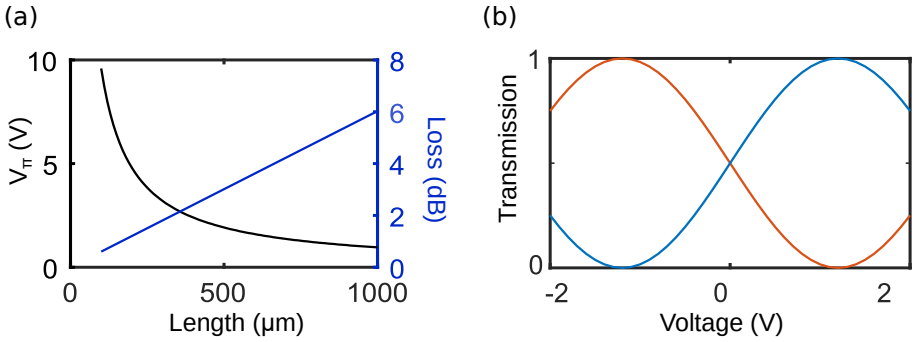

Figure 3.4: Behavior of the device: (a): The black curve shows the expected voltage needed to achieve a full π-switch as a function of the length of the arms of the interferometer. The blue curve shows the calculated propagation loss as a function of the length of the device. **(b):** Ideal behavior of the device. Light can be routed between the two outputs by changing the voltage across the arms of the device.

The phase *difference* between light propagating along the [110]- and [1$\bar{1}$0]-directions is given by $2\phi = 2|\Delta n|kL$. It follows that the voltage required to achieve a full π-phase difference between the two arms is given by

$$V_\pi = \frac{d\pi}{kLn^3 r_{41}}. \tag{3.13}$$

The longer the arms of the interferometer, the smaller the V_π, however, longer arms lead to an increase in propagation loss, which is mainly caused by the free-carrier absorption in the doped layers. This is explained in greater detail in section 3.3.4. This absorption is calculated from Finite Element (FE) simulations, and the optimum length of the interferometer arms is found considering the trade-off between loss and V_π. Figure 3.4(a) shows how V_π reduces with an increased length of the interferometer arms (black line), while the losses increase with the length (blue line). We find that for a length of 400 μm, we can switch the light between the two outputs by applying approximately 2.5 V, while keeping propagation loss under 3 dB. The expected behavior for a device of this size is shown in fig. 3.4(b), where the red and blue curves correspond to the output from the two ports shown in fig. 3.3.

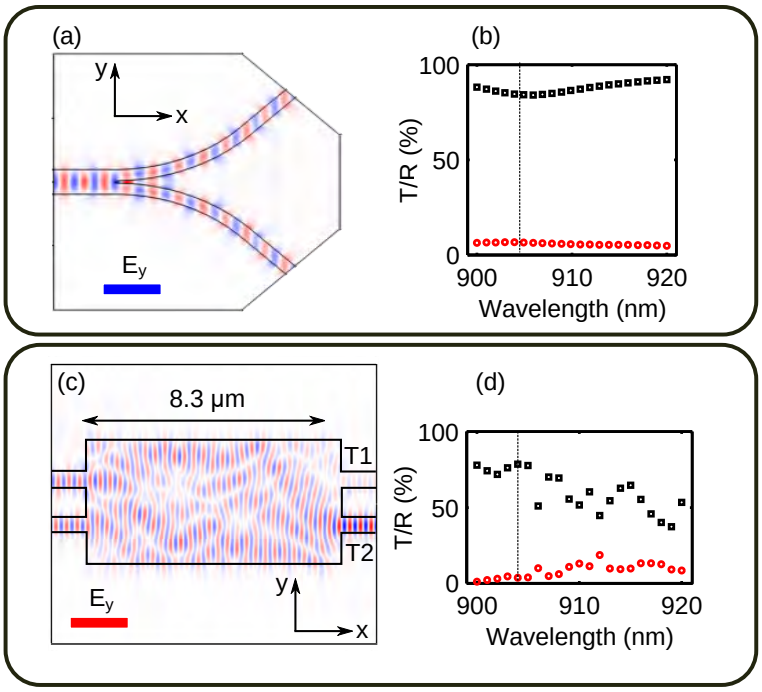

Figure 3.5: Numerical analysis of the components of the circuit: (a): FE simulation of the y-component of the electric field distribution in the power-splitter at a wavelength of 904 nm. Equal power and phase at the two outputs is ensured by the mirror symmetry. **(b):** Simulated total transmission efficiency (black squares) and reflectivity (red circles) of the power-splitter. The dashed vertical line indicates the wavelength of the quantum dot used in this experiment (904 nm). **(c):** Simulated electric field distribution in the MMI combiner, when launching the same amount of power in the two ports but $\pi/2$ out of phase. **(d):** Simulated total transmission (black squares) and reflection (red circles) in the MMI. The transmission level is the sum of both outputs T1 and T2 indicated in (c). The simulations are done by Dr. L. Midolo.

3.2.3 Sample simulations and fabrication

The individual components of the device, i.e., the power splitter and the MMI, are simulated in order to assess their performance as a function of wavelength. The power-splitter [92] consists of a single-mode waveguide, that is tapered out to a cross-sectional width of 500 nm and then split into two 240 nm wide single-mode waveguides. The MMI is a 2×2 3-dB coupler based on two-fold imaging [93]. Figure 3.5(a) shows the FE simulation of the y-component of the electric field along the power-splitter. Figure 3.5(b) shows that for a broad range of wavelengths, the transmission efficiency (black squares) is close to unity, while the reflectivity (red circles) of the device is low. The MMI is simulated as well, and fig. 3.5(c) shows the y-component of the electric field, when the two input ports are excited with equal power, but $\pi/2$ out of phase. The simulated total transmission (black squares) and reflection (red circles) as a function of wavelength is shown in fig. 3.5(d). These simulations suggest that the device will show good performance at a wavelength of 904 nm. The reflections introduced by the power-splitter and MMI respectively

are low enough that we neglect them in the further simulation (see sec. 3.3.4). The performance of the power-splitter depends weakly on the wavelength in the considered range, whereas the MMI shows significant oscillations in transmission and reflection with wavelength with a transmission maximum and reflection minimum around 904 nm as desired for the experiment considered here. It is thus concluded that the imperfections of these constituent components will not have a detrimental effect on the performance of the device.

The device is fabricated on a wafer, the structure of which is illustrated in fig. 3.2(b).

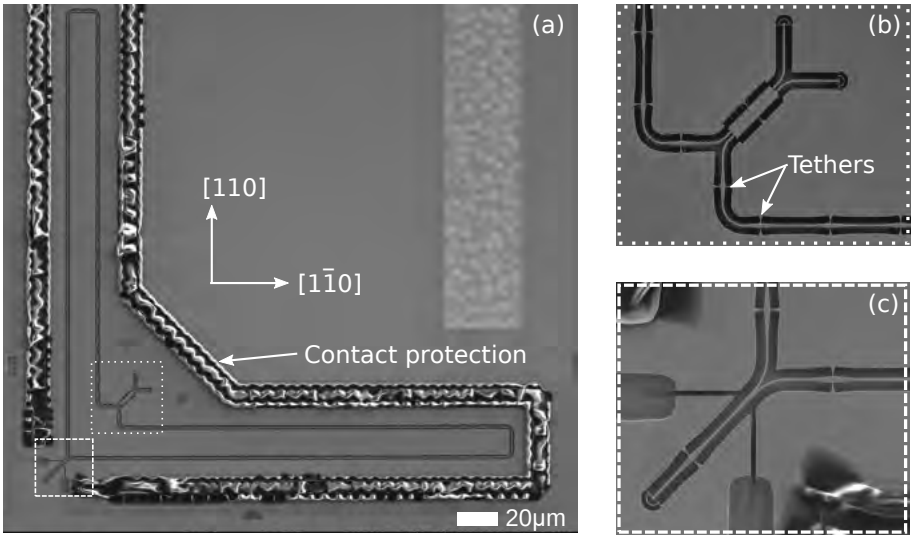

Figure 3.6: Scanning electron microscope (SEM) image of the device: (a): SEM image of the full device. The wavy pattern is contact protection on the p-contact. **(b)**: Zoom-in on the multi-mode interferometer (MMI). **(c):** Zoom-in of the power-splitter. The trenches ensure electrical isolation between the switching-region containing the interferometer, and the source-region containing the quantum dots. The SEM images are taken by Dr. L. Midolo.

Figure 3.6(a) shows a SEM image of the full device. The light propagates from the input port in the bottom left corner of the SEM, to the initial power splitter shown in fig. 3.6(c). It then propagates along the arms of the interferometer, experiencing a phase change depending on the applied bias and the propagation direction. The light from the two arms is then recombined on a 3 dB MMI combiner shown in fig. 3.6(b). The light is coupled out from the chip using circular gratings [63].

The suspended waveguides are supported by 100-nm-wide tethers. Aside from supporting the waveguides, the tethers serve the purpose of electrically connecting the bulk and the waveguide, meaning that the electric field applied between the p- and n- contacts is transported to the waveguide region. The presence of an electric field in the waveguide is crucial for the operation of this device. A trench is defined between the input-waveguide and the power-splitter as can be seen in fig. 3.6(c). The purpose of the trench is to allow us to change the bias across the arms, and

thus route the light between the two outputs, without tuning the quantum dots in the source region of the device. If the dots tune with the applied field, this would result in the dots exiting the device from one output port having a different energy than the dots exiting the device from the other output port, and the device would not be applicable in any algorithm requiring indistinguishable photons to be routed between two outputs.

3.3 Device characterization

3.3.1 Experimental setup

The sample is mounted on a chip-carrier, and wire-bonded to a printed circuit board (PCB). The PCB is placed on a cold-finger in a Microstat HiRes II (Oxford Instruments) flow cryostat with coaxial feedthroughs (see fig. 3.7). The cold-finger is cooled with liquid helium, and the temperature is measured by a sensor with $\pm$ 12 mK accuracy and controlled by a 50 Ω thermofoil heater anchored on the cold-finger [29]. The temperature is kept at 10 K throughout the measurements in order to avoid thermal depopulation of the quantum dots. The sample can be moved in the xy-plane, by controlling the translation stages.

The excitation laser used for the quantum dot measurements in this experiment is a Ti:sapphire laser (Coherent Mira 900) operated in continuous wave mode. For transmission measurements, we use a continuously tunable laser (CTL) from Toptica. The laser is coupled to a polarization maintaining (PM) fiber and sent to the cryostat table. Here the excitation laser is sent through a half-waveplate ($\lambda/2$) followed by a polarizing beam splitter (PBS) which allows controlling the power sent to the sample. Subsequently, the beam is sent through a 50:50 beam splitter to monitor the power sent to the sample. Another half-waveplate ensures control over the polarization of the laser light going to the sample. The beam then goes through an optical microscope setup (Olympus BXFM) where a 50:50 beam splitter guides the light to an objective (Nikon CFI Plan Flour ELWD 40xC) with a numerical aperture of 0.6.

The sample is imaged by flipping in and out mirrors so that white light rather than laser light is sent to the sample, and the reflection is sent to the CCD camera rather than to the detection path. An example of the image of a structure is shown in fig. 3.7 on the PC-screen. The high resolution combined with the fine step-size of the translational stages allows for very precise alignment of $\approx \pm 100$ nm. To go from imaging mode to measurement mode, the two flip mirrors are switched back, and the sample is now illuminated by the laser, and the luminescence is sent to a spectrometer through a PM fiber. The fiber serves as a pinhole for spatially selecting the area from which to collect the photo-luminescence. The luminescence from the sample is sent to a spectrometer (McPHERSON 207), that decomposes the light into its wavelength components with a resolution of 50 pm, and detects it

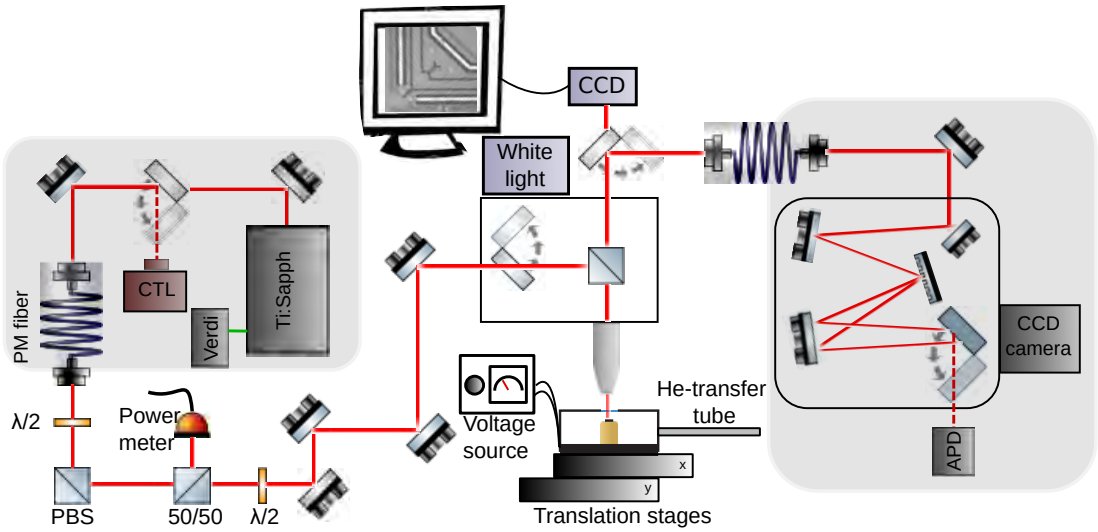

Figure 3.7: Experimental setup: Sketch of the optical setup used to carry out electrical and optical characterization of the sample. The sample can be excited with a Ti:Sapph laser or a continuously tunable laser (CTL). The laser is coupled to a fiber and sent to the cryo-table where a half-wave plate and a PBS ensures power control, and a subsequent half-wave plate provides control over the polarization. The sample may be illuminated with white light or laser light, and the photoluminescence from the sample may be sent to the CCD camera for direct imaging of the sample, or to the spectrometer for further analysis.

on a CCD camera (Princeton instruments TEA/CCD)

3.3.2 Electrical characterization

As mentioned in sec. 3.2.3, the device consists of two regions separated by an isolation trench allowing to set the voltage in the two regions independently. We refer to these regions as the source region and the switching region in the following. Figure 3.8(a) shows a model of the electrical circuit. The two diodes can be controlled individually, but are connected by the waveguide running across the trench. This connection is modelled as a resistance in the n- and p-layer respectively. When there is a voltage drop between the two diodes, electrical power may be dissipated in the waveguide causing it to heat up, which may in extreme cases lead to sublimation of the material. This happened at the early stage of the experiment, as can be seen in fig. 3.8(b), after which special care was taken by connecting the n-contacts to the same ground. The sheet resistance of the p-layer is ≈ 20 times larger than the n-layer due to the lower carrier mobility, therefore the current will mainly flow in the n-layer. Due to this potential heat dissipation, we are limited to work in a restricted voltage range in the switching region, as the voltage in the source region must be kept constant. However, the V_π of the device is as small as 2.5 V, allowing us to fully switch emission without damaging the sample.
Figure 3.8(c) and (d) indicate that there is some cross-talk between the two regions, mediated by the waveguide connecting the two. This is seen as a shift in the inflection point given by the voltage applied in the other region. In order to assess whether this cross talk between the two regions has a significant effect on the emission from the quantum dots in the source region, spectra of dots located in the source region are recorded while changing the voltage across the switching region. Figure 3.9 shows the intensity of quantum dots in the source region as a function of the voltage across the switching region. It shows that the quantum dots do not tune significantly when the voltage is changed across the other diode.

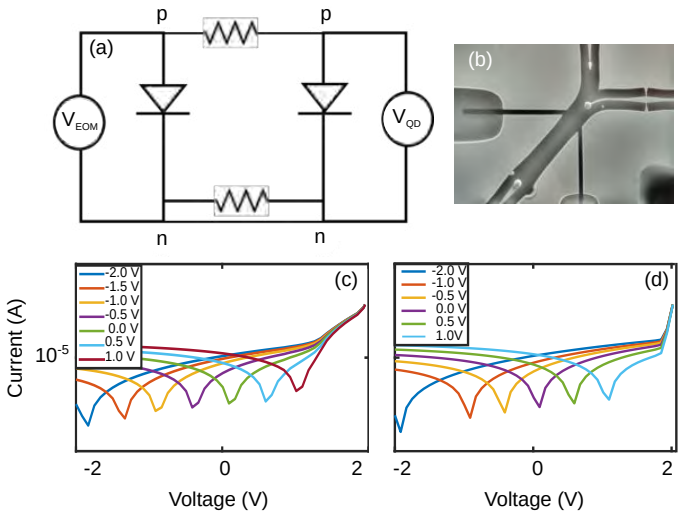

Figure 3.8: Circuit and IV-curves: (a): Model of the electrical circuit of the device. The two sources are grounded together ensuring a common n contact. When the two regions/diodes are biased differently, there will be a current running in the p-layer. The waveguide connecting the two regions is indicated as a resistance in both the n and the p-layer. **(b):** SEM image of a broken sample. **(c):** IV curve of the switching-region for different constant voltages across the source region as indicated in the inset. The graphs show the absolute value plotted on log scale **(d):** IV curve of the source-region for different constant voltages across the switching region as indicated in the inset.

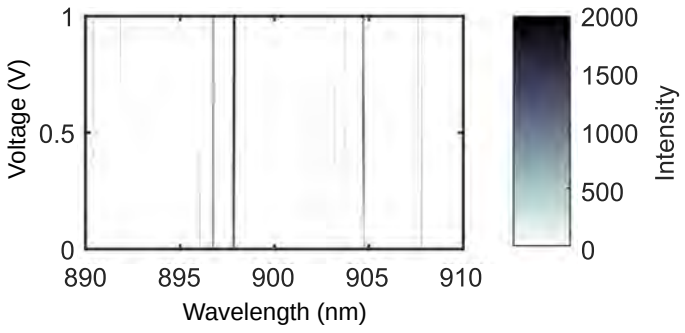

Figure 3.9: Tuning-test: Photoluminescence intensity of the quantum dots in the source region as a function of the voltage applied across the switching region.

3.3.3 Transmission measurements

Initial optical characterization is done at 10 K by focussing the CTL laser (see fig. 3.7) at the input port (see fig. 3.3) of the device, and analysing the intensity at the two outputs. The intensity is evaluated from the image on the CCD as a function of applied voltage in the switching region and wavelength of the CTL. The voltage is scanned between −1.5 V and 1.5 V in steps of 0.1 V, and the wavelength is swept from 911 nm to 920 nm in steps of 0.1 nm. The analysis is done by defining two regions of interest on the image, and integrating the intensity in that region by summing the pixels. Figure 3.10 shows the intensity of output 2 (a) and output 1 (b). In order to correct for any power fluctuations of the laser, the data from each wavelength has been normalised using a gray-scale normalisation. The plots in fig. 3.10 clearly show an anti-correlated behavior of the two outputs as a function of the voltage in a broad wavelength range. The maximum emission from port 1 (fig. 3.10(b)) occurs at a positive voltage, while the emission from this port is minimized at −1 V. The maximum emission from port 2 (fig. 3.10(a)) occurs at a negative voltage and is minimized at 1 V.
The maximum emission from port 2 shifts slightly to lower voltages for longer wavelengths. The fact that the maximum emission from port 2 is not exactly matched with the minimum emission from port 1 can be explained by electroabsorption and is investigated further in sec. 3.3.4.
We repeat the measurements using a single quantum dot as a light source. The measurement is performed at 10 K, and the dots are excited above the GaAs band using the Ti:Sapph laser in cw at 808 nm. A constant bias of 1.15 V is applied to the source region throughout the measurement. An ensemble of quantum dots is probed by exciting and collecting at the input port (see fig. 3.11(a)). To probe only the dots that couple to the propagating mode of the waveguide, we keep the excitation at the input port but move the collection to the output port. In the device in question, only one dot at 904 nm couples efficiently to the propagating

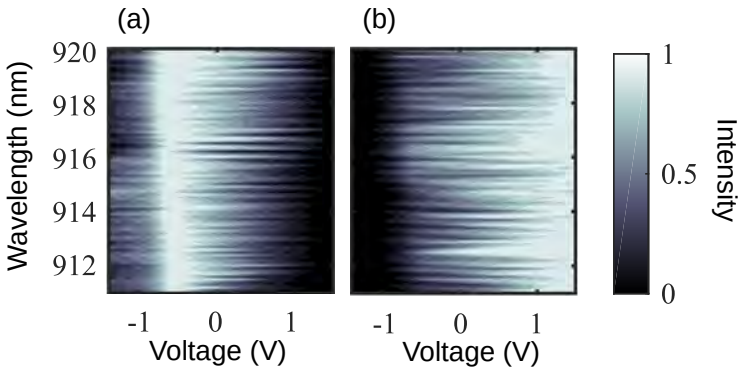

Figure 3.10: Transmission measurements: The intensity evaluated from images on the CCD camera at the two outputs as a function of wavelength and voltage. Subfigure a (b) shows the intensity from output 2(1).

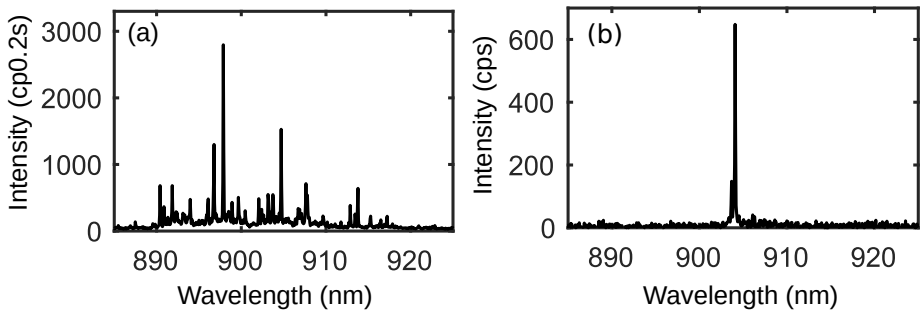

Figure 3.11: Quantum dot spectra: (a): Ensemble of QDs excited and collected at the input port. **(b)**: Emission from a QD excited at the input and collected at the output.

mode and can thus be collected from either of the output ports depending on the voltage applied in the switching region cf. fig. 3.10.

While exciting the quantum dot at the input port, we change the voltage in the switching region and monitor the intensity of the quantum dot line at the two output ports.
Figures 3.12(a) and (b) show the dot emission collected from port 1 at applied voltages of -0.4 V and +1.2 V respectively. In figs. 3.12(c) and (d) emission from the same dot is collected at the same voltages, but collected from port 2. The total integrated intensity of the dot emission as a function of the voltage applied across the switching region is shown in fig. 3.12(e). These data show an anti-correlation in the emission intensity between the two output ports for a voltage range spanning from -1 V to +1.2 V. We notice that the maximum emission from port 2 (red) does not coincide with the minimum emission from port 1 (blue). In fact the intensity of the signal from both ports decreases with the field strength in reverse bias. One initial concern could be that the lack of total isolation between the two diodes causes the quantum dot to quench when the field is too strong in the switching region. However, as we see the same behavior when using an external laser source, (fig. 3.10), we can rule out this effect. The experimental data show agreement with the predicted behavior of the device (see fig. 3.4(b)), and shows an anti-correlation in the output as a function of the applied voltage. The fact that the transmission measurements performed using the external laser source mimics the measurements performed using the quantum dot as a light source, confirms that the switching is in fact caused by a phase difference accumulated over the two arms. The deviations between the observed data (fig. 3.12(e)) and the ideal behavior (fig. 3.4(b)) are analyzed and by including contributions from other effects such as propagation loss, electroabsorption and reflections, we devise a model that mimics the experimentally observed behavior.

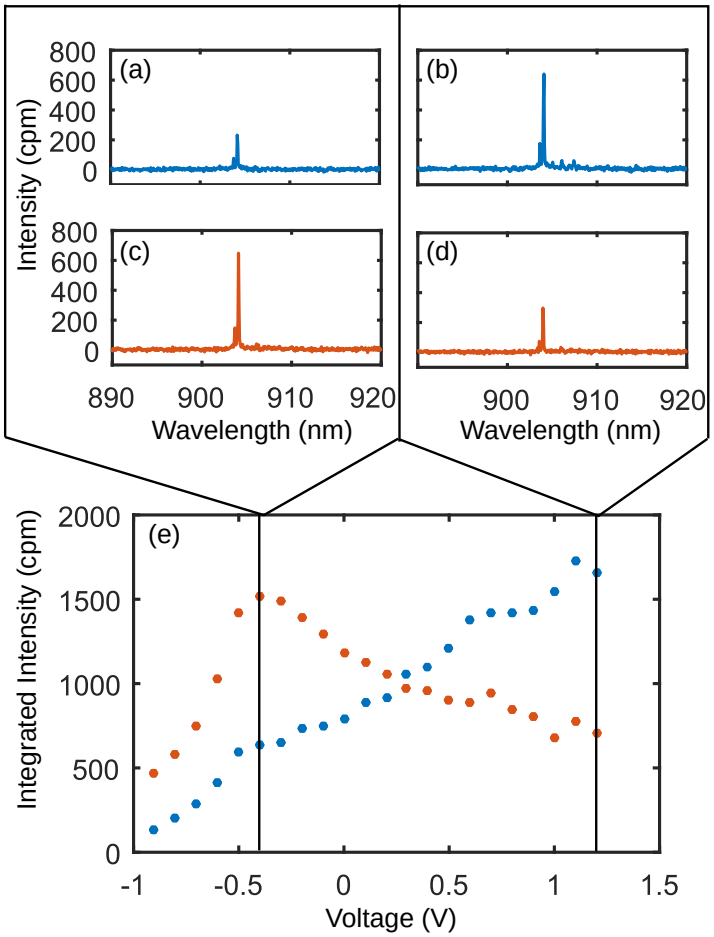

Figure 3.12: Routing of single quantum dot emission: (a): Spectrum obtained from output 1 at -0.4V. **(b):** Spectrum obtained from output 1 at +1.2V. **(c):** Spectrum obtained from output 2 at -0.4V. **(d):** Spectrum obtained from output 2 at 1.2V. **(e):** The integrated peak intensity of the quantum dot emission as a function of the voltage. The blue (red) dots show the intensity collected at port 1(2).

3.3.4 Simulations

In this section, a theoretical model is proposed to explain the experimentally observed behavior of the device. Starting from the ideal case and gradually including contributions from other effects, we end up with a model that mimics the experimentally observed behavior of the device.
The device consists of many components; namely in- and out couplers, a power-splitter, waveguides and an MMI. Each component is initially considered individually, yielding an S-matrix for that component. These have then been combined using a cascading method [94], resulting in a transmission model of the full device. First the S-matrices for the power-splitter (abbreviated Y-splitter) and the waveguides are identified.

$$S_{y-splitter} = \begin{pmatrix} 0 & 0 & \beta \\ 0 & 0 & \beta \\ \beta & \beta & 0 \end{pmatrix}, \tag{3.14}$$

where $\beta = \frac{1}{\sqrt{2}}$.
The two waveguides can be described by a 4×4 matrix of the form

$$S_{wg} = \begin{pmatrix} 0 & 0 & \zeta_1 & 0 \\ 0 & 0 & 0 & \zeta_2 \\ \zeta_1 & 0 & 0 & 0 \\ 0 & \zeta_2 & 0 & 0 \end{pmatrix}, \tag{3.15}$$

where $\zeta = e^{iknl}$. Here $k = \frac{2\pi}{\lambda}$, l is the length of the arms, and n is the wavelength- and voltage-dependent effective refractive index of the waveguide, given by

$$n(\lambda, V) = n_0(\lambda) \pm \frac{1}{2} n_0(\lambda)^3 r_{41} \frac{V}{d}, \tag{3.16}$$

where d is the distance between the contacts, and V is the applied voltage. The built-in voltage is taken into account in the simulations.
In the matrix (3.15), ζ_1 and ζ_2 corresponds to light travelling in the two arms of the interferometer, and thus to the positive and negative solutions of eq. (3.16).
The 2×2 MMI, can be described by

$$S_{MMI} = \begin{pmatrix} 0 & 0 & \beta & i\beta \\ 0 & 0 & i\beta & \beta \\ \beta & i\beta & 0 & 0 \\ i\beta & \beta & 0 & 0 \end{pmatrix}. \tag{3.17}$$

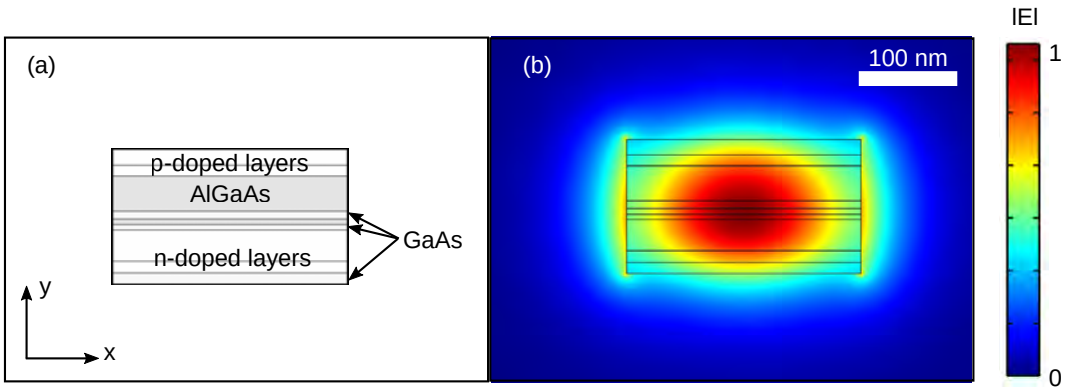

Figure 3.13: Finite element simulations: (a): Geometry of model used to predict the effective refractive index in the waveguides. **(b):** FE simulation of the transverse electric mode. The overlap between the electric field and the various layers defines the effective electro-optic coefficient and the magnitude of the absorption.

These three matrices are cascaded, yielding a transmission model for the device assuming perfect in and out-coupling

$$S_{tot} = \begin{pmatrix} 0 & \beta^2\zeta_1 + i\beta^2\zeta_2 & i\beta^2\zeta_1 + \beta^2\zeta_2 \\ \beta^2\zeta_1 + i\beta^2\zeta_2 & 0 & 0 \\ i\beta^2\zeta_1 + \beta^2\zeta_2 & 0 & 0 \end{pmatrix}, \tag{3.18}$$

which can be simplified to

$$S_{tot} = \begin{pmatrix} 0 & \frac{1}{2}(\zeta_1 + i\zeta_2) & \frac{1}{2}(i\zeta_1 + \zeta_2) \\ \frac{1}{2}(\zeta_1 + i\zeta_2) & 0 & 0 \\ \frac{1}{2}(i\zeta_1 + \zeta_2) & 0 & 0 \end{pmatrix}. \tag{3.19}$$

A FE simulation of the structure gives us the real and imaginary part of the effective refractive index as a function of the wavelength of the light propagating in the structure and the voltage applied. Figure 3.13(a) shows the model as it is built in the FE software COMSOL. All the different layers of the wafer have been included in the model. Figure 3.13(b) shows the electric field distribution inside the waveguide. The simulation is run for both the case of a positive and a negative change of refractive index, and ζ_1 and ζ_2 can thus be calculated.
The intensity at the two outputs is found from $I_{1(2)} = |\frac{1}{2}(i\zeta_{1(2)} + \zeta_{2(1)})|^2$. The doped layers give rise to increased free-carrier absorption, i.e., the promotion of a carrier from one excited state to another excited state by means of energy from an absorbed photon. To see this we start by including the imaginary part of the

refractive index

$$\begin{aligned}\zeta &= e^{i\frac{2\pi}{\lambda}nl} \\ &= e^{i\frac{2\pi}{\lambda}(n_r+in_i)l} \\ &= \underbrace{e^{i\frac{2\pi}{\lambda}n_r l}}_{\text{A}} \cdot \underbrace{e^{-\frac{2\pi}{\lambda}n_i l}}_{\text{B}}.\end{aligned} \tag{3.20}$$

We see from the term marked B in eq. (3.20) that the imaginary part of the refractive index is responsible for attenuation of the wave as it propagates in the medium. The real part of n determines the phase velocity of the wavefronts. Since the optical intensity of light is proportional to the square of the electric field, we can define a decay constant of

$$\alpha = \frac{4\pi n_i}{\lambda}. \tag{3.21}$$

The decay constant, α, is related to the free-carrier density, N, in the doped layers, and we deduce how they are related in the following. First, we look at the free electron model, and then modify it to describe the case of a doped semiconductor. The electric displacement $\mathbf{D}$ is given by

$$\mathbf{D} = \epsilon_r\epsilon_0\mathbf{E} = \epsilon_0\mathbf{E} + \mathbf{P}, \tag{3.22}$$

where ϵ_0 is the vacuum permittivity and ϵ_r is the relative dielectric constant. $\mathbf{E}$ is the electric field, and $\mathbf{P}$ is the polarization, i.e., the net dipole moment per unit volume. Here we are interested in ϵ_r as it contains information about how light propagates through the material.
We can treat the free electrons in our doped semiconductor as a plasma, and apply the free electron model to our system. The equation of motion for a free electron in an electric field $\mathbf{E}(t)$, is given by

$$\ddot{x} + \gamma\dot{x} = \frac{qE_0}{m_0}e^{-i\omega t}, \tag{3.23}$$

where ω is the angular frequency of the driving field, E_0 is the field amplitude, q is the charge of the electron and γ is the damping. Hence the electron will oscillate with some damping. The solution to this is found by expressing the time dependence of x; $x = x_0e^{i\omega t}$, and solving for x. This yields

$$x = \frac{qE_0e^{-i\omega t}}{m_0(\omega^2 + i\gamma\omega)}. \tag{3.24}$$

Since the polarization $\mathbf{P}$ can be written as qNx, where N is the number of electrons per unit volume, we can express the displacement field as

$$\mathbf{D} = \epsilon_0\epsilon_r\mathbf{E} = \epsilon_0\mathbf{E} + \frac{Nq^2E_0e^{-i\omega t}}{m_0(\omega^2 + i\gamma\omega)}, \tag{3.25}$$

and thus we have an expression for the relative dielectric constant ϵ_r, namely

$$\epsilon_r(\omega) = 1 + \frac{Nq^2}{\epsilon_0 m_0} \frac{1}{(\omega^2 + i\gamma\omega)} = 1 + \frac{\omega_p^2}{(\omega^2 + i\gamma\omega)}, \tag{3.26}$$

where ω_p is the plasma frequency, which is a characteristic oscillation frequency of the electron in a material when exposed to a small charge separation.
In order to adapt this model to describe a doped semiconductor, we must take into account the effective masses of the electrons and holes. This is done merely by replacing the m_0 in eq. (3.26) by m^*. Additionally, we must account for the polarizability of the undoped material. This is taken into account by rewriting eq. (3.25) as

$$\mathbf{D} = \epsilon_b \epsilon_0 \mathbf{E} + \frac{Nq^2 E_0 e^{-i\omega t}}{m^*(\omega^2 + i\gamma\omega)}, \tag{3.27}$$

where ϵ_b is added to account for the polarization of the undoped material. In this equation, N denotes the density of free carriers caused by the doping. From this we can now rewrite the relative dielectric constant for the case of a doped semiconductor

$$\epsilon_r(\omega) = \epsilon_b + \frac{Nq^2}{m^* \epsilon_0} \frac{1}{(\omega + i\gamma\omega)} = \epsilon_b \left(1 + \frac{\omega_p^2}{(\omega + i\gamma\omega)}\right), \tag{3.28}$$

where the plasma frequency now takes the form: $\omega_p^2 = \frac{Nq^2}{\epsilon_b \epsilon_0 m^*}$, and is thus also affected by the introduction of dopants.
The imaginary part of the relative dielectric constant is given by $\epsilon_i = \frac{\epsilon_b \omega_p^2 \tau}{\omega(1-\omega^2\tau^2)}$, and can be related to the imaginary part of the refractive index by $n_i = \frac{\epsilon_i}{2n}$. From eq. (3.21), we can now define a free-carrier absorption as

$$\alpha_{\text{fc}} = \frac{Nq^2}{m^* \epsilon_0 n c \tau} \frac{1}{\omega^2}. \tag{3.29}$$

Here we have used the substitution $\tau = 1/\gamma$, and τ thus denotes the characteristic damping time scale of the system. The absorption scales with the carrier density in the doped layers, and since we have a relatively high degree of doping, we include absorption in our model, by including the imaginary part of the refractive index in the four doped layers [95] (see fig. 3.13(a)). This diminishes the signal as can be seen from fig. 3.14, and explains the relatively long integration times needed to get a good signal-to-noise ratio, but it neither explains the asymmetrical shape of the signal we observe, nor the low extinction ratio defined as the ratio between the optical power generated when the ports are on and off.

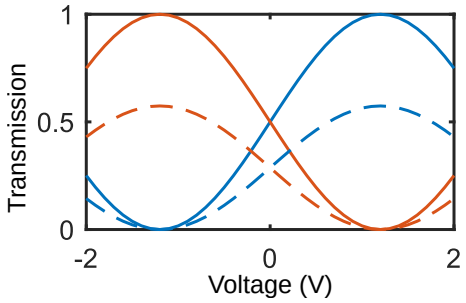

Figure 3.14: Including propagation loss: By adding absorption in the doped layers of the wafer the model predicts an attenuation of signal by almost a factor of 2 (dashed line) compared to the ideal case of no absorption (solid lines).

In order to account for the fact that the signal from both arms decreases at large negative applied voltages in the switching region, we included electroabsorption in the model according to the phenomenological work by Stillman et. al. [96]. This work presents theoretical calculations of the Franz-Keldysh effect based on the theory developed in Refs. [97, 98], along with experimental work, and shows good agreement between the model and the experimental results.
The Franz-Keldysh effect is a change in the optical absorption in a semiconductor in the presence on an electric field. Applying a static electric field to a semiconductor changes the optical absorption profoundly. The potential will no longer retain the periodicity of the lattice, and therefore the Bloch wavefunctions will no longer represent the stationary states of the crystal. The semiconductor may now absorb photons with energy less than the band-gap energy; $\hbar\omega < E_g$ [77]. It is a result of the electron and hole wavefunctions acquiring tails that extend into the bandgap, and as a consequence, the overlap between the wavefunctions is increased leading to an increase in the optical absorption. The field- and wavelength dependent Franz-Keldysh electroabsorption coefficient for GaAs can be calculated from [96]

$$\alpha(\omega, E) = \frac{1.0 \cdot 10^4}{n} E^{1/3} \sum_{j=1,2} \left(1 + \frac{m}{m_{vj}}\right) \left(\frac{2\mu_j}{m}\right)^{4/3} \cdot \left[\left| \left(\frac{d\mathrm{Ai}(z)}{dz}\right)_{\beta_j} \right|^2 - \beta_j |\mathrm{Ai}(\beta_j)|^2 \right], \tag{3.30}$$

where

$$\beta_j = 1.1 \cdot 10^5 (E_g(x,T) - \hbar\omega)(2\mu_j/m)^{1/3} E^{-2/3}. \tag{3.31}$$

Here Ai is the Airy function and the sum is over the light- and heavy-hole valence bands. The parameters used for the numerical calculations are: refractive index $n = 3.5$, effective mass of the light hole; $m_{v1}/m = 0.087$, reduced mass of the electron and light hole; $\mu_1/m = 0.0377$, effective mass of the heavy hole; $m_{v2}/m = 0.450$ and the reduced mass of the electron and heavy hole; $\mu_2/m = 0.0579$. The

temperature dependent band-gap of AlGaAs, $E_g(x,T)$, can be calculated from[1]

$$E_g(x,T) = 1.519 + 1.155x + 0.37x^2 - 5.41 \cdot 10^4 * T^2/(T+204), \tag{3.32}$$

where x is the aluminum (Al) content.
From eq. (3.30); the behavior of the absorption coefficient is thus governed by Airy functions. For small fields, $E \to 0$ the absorption drops quickly to zero at $\hbar\omega = E_g$. In the presence of an electric field, $\alpha(\omega, E)$ shows oscillations above the band-gap, and more importantly, acquires a tail extending into the band-gap. This is illustrated in fig. A.1 in the appendix.
Figure 3.15 shows the absorption coefficient $\alpha(\mathrm{cm}^{-1})$ for GaAs at 10 K (a), GaAs at 300 K (b), and AlGaAs at 10 K (c) evaluated at different *applied* voltages. The built-in field of -1.4 V is included in the model, and therefore the absorption is minimized for an applied field of 1.5 V, and maximized for -2.0 V.

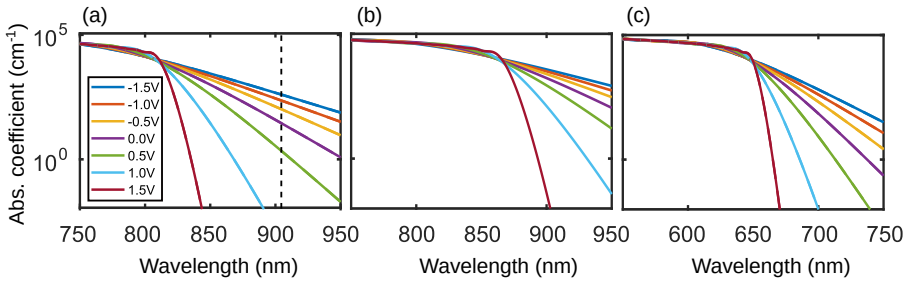

Figure 3.15: Absorption coefficient as a function of wavelength for different applied voltages: (a): Absorption coefficient for GaAs at 10 K. The dashed line indicates the emission wavelength of the quantum dot investigated. **(b)**: Absorption coefficient for GaAs at 300 K. **(c)**: Absorption coefficient for AlGaAs at 10 K. Note the different wavelength axes

Figure 3.15 shows the absorption coefficient as a function of wavelength for different applied voltages. It is clear that at $V_{applied} = 1.5$ V (dark-red line), the applied voltage counteracts the built-in voltage and the absorption coefficient drops rapidly at $\hbar\omega = \hbar 2\pi c/\lambda = E_g$. When going in reverse bias, the applied and built in field add up, and the effective field causes the absorption to extent into the band-gap. It is evident that the device only works at cryogenic temperatures, as the absorption coefficient in the wavelength range of quantum dot emission (~ 900 nm) exceeds $1000\,\mathrm{cm}^{-1}$ when applying a reverse bias at 300 K (fig. 3.15(b)). This is because the increase in temperature causes the band-gap to shift to longer wavelengths as given by eq. (3.32) and evidenced by comparing figs. 3.15(a) and (b). Figure 3.15(c) shows that the absorption in the AlGaAs does not influence the propagation significantly at the targeted wavelengths as the band-gap energy is much higher than the quantum dot emission energy. For this reason we only include the Franz-Keldysh

[1] http://www.ioffe.ru/SVA/NSM/Semicond/AlGaAs/bandstr.html

effect in the GaAs layer situated between the p- and n-contacts of the waveguide (see fig. 3.13).
By including this effect in the FE simulations of the device, we see a clear reduction in the signal at large negative voltages (see fig. 3.16(a)) as well as a wavelength dependence. Light with longer wavelengths, i.e., further from the GaAs band-edge (1.52 eV), experience a smaller degree of electro-absorption. Since the dot that couples efficiently to the propagating mode of the device emits at 904 nm (1.37 eV), where the large field increases the absorption significantly, we observe a decrease in the signal from both ports when applying a large negative voltage. We stress that the reason why this effect is not symmetric in applied voltage is that the built-in field is negative, therefore applying a positive voltage effectively diminishes the field in the waveguide, while applying a negative voltage adds to the field already present in the waveguide.

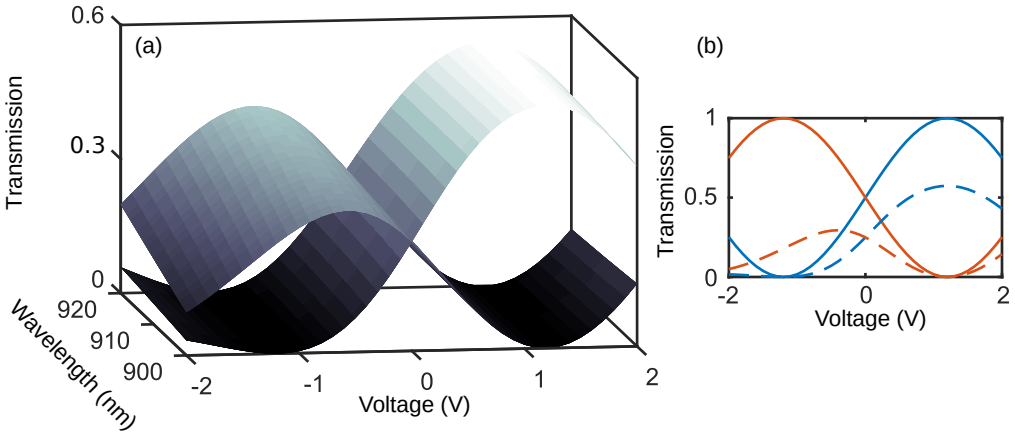

Figure 3.16: The Franz-Keldysh effect: (a): Transmission from the two outputs as a function of voltage and wavelength. The model includes propagation loss and the Franz-Keldysh effect. **(b):** The signal evaluated at 904 nm when including absorption and the Franz-Keldysh effect (dashed lines) compared to the ideal case (solid lines).

Figure 3.16(b) shows the effect of the Franz-Keldysh effect at 904 nm. Here the effect is evident, and clearly shows that the transmission will be reduced significantly at large negative applied voltages. However, the Franz-Keldysh effect does not account for the low extinction ratio we see in our data, as the signal can still be switched completely off even in the presence of the included electroabsorption. Thus, we must look for an explanation for the reduced extinction ratio elsewhere. The gratings terminating the device have finite reflectivity of $\sim 30\,\%$, and therefore standing waves form in the structure. In order to investigate the effect of the reflectivity at the couplers, they are included in the numerical model. The effect of the finite reflectivity is visible from fig. 3.17. The anti-correlated output from the two ports is still present, but the resonances caused by the reflections add intensity fluctuations as a function of wavelength and reduce the extinction ratio of the switching

signal (fig. 3.17(a) and (b)). Figures 3.17(c) show the signal evaluated at 904 nm. The dashed lines represent the result of the numerical model including propagation loss, electroabsorption and reflectivity from the gratings, and should be compared to the ideal case represented by the solid lines. The gratings introduce Fabry-Pérot resonances in the structure which has a detrimental effect on the extinction ratio of the signal. This becomes evident when comparing to fig. 3.17(d) that show the same numerical simulation with a reflectivity of 3 %. The extinction ratio of the signal in this case is ~ 26 which should be compared to the extinction ratio of ~ 3.3 extracted from the data from fig. 3.17(c), where we have used a reflectivity of 30 %.

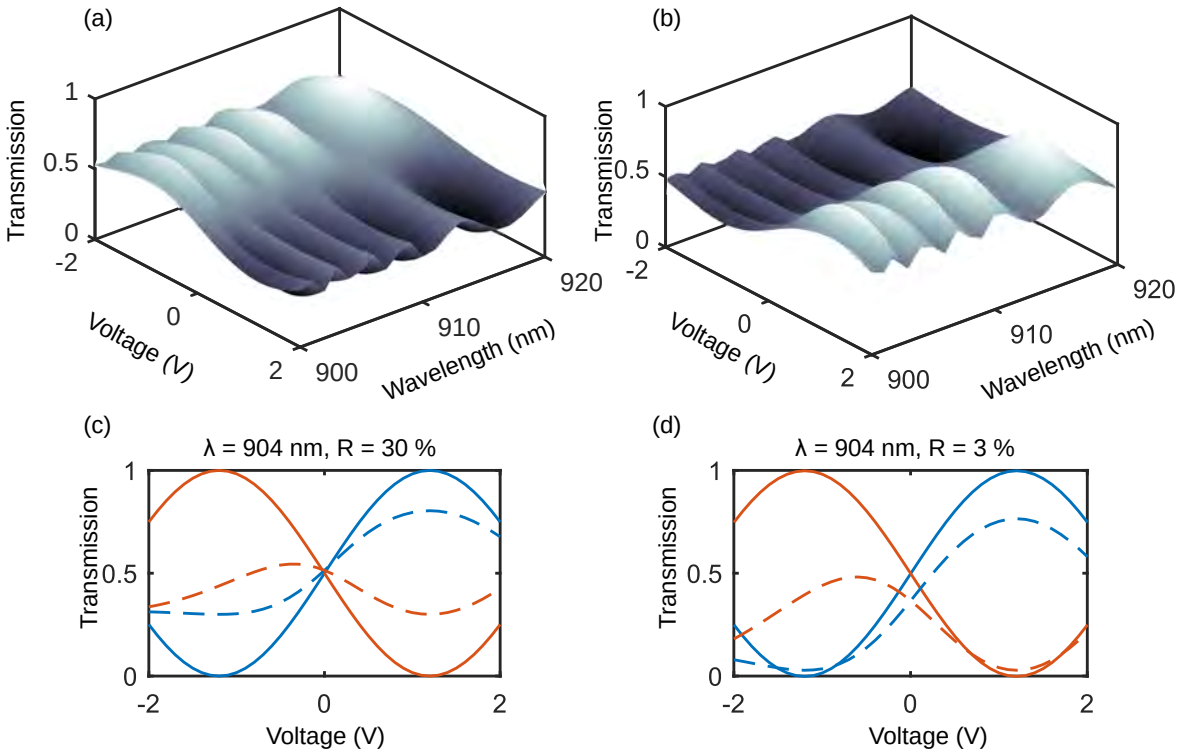

Figure 3.17: The effect of the finite reflectivity from the gratings: The output from port 2(a) and 1(b) as a function of applied voltage and wavelength as calculated from the transmission model including propagation loss, electroabsorption and reflections from the gratings. **(c):** Comparison between the simulation evaluated at 904 nm in the ideal case (solid lines) and the case where propagation loss, electroabsorption and reflections are included (dashed lines). **(d):** Same as (c) but evaluated at 904 nm for a reflectivity of 3%.

The full transmission model including propagation loss, electroabsorption and grating induced reflectivity shows good agreement with the experimental data. Figure 3.18 shows the experimental data from the quantum dot measurements (dots) and the result of the full transmission model evaluated at the emission energy of the quantum dot (solid lines). In both cases the data is normalized to the sum of the two output intensities. The model is fit to the data using only one free parameter, namely the crossing point of the two curves (at $V = 0.3$ V). The reason for

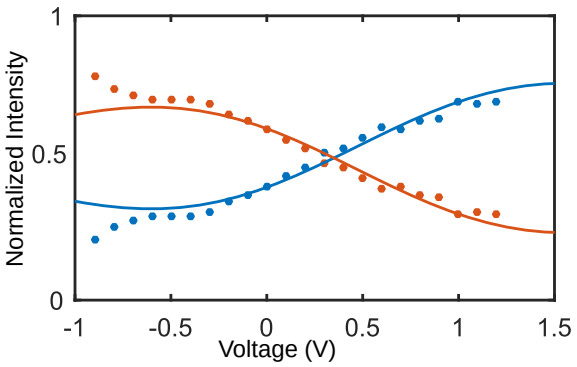

Figure 3.18: Comparing model and quantum dot experiment: The experimental data (dots) and the model (solid lines) including propagation loss, the Franz-Keldysh effect and the gratings. The model has been fitted to the data using only one free parameter, namely the crossing point of the two curves at $V = 0.3\,\mathrm{V}$.

this shift in crossing-voltage is the built-in field and unavoidable asymmetry in the device caused by fabrication imperfections. Given the good agreement between the data and the prediction of the transmission model, it is reasonable to argue that the effects taken into account in the model are responsible for the observed behavior. Hence, we conclude that the anti-correlation in the output intensities is a direct result of the index modulation caused by the applied voltage. The fact that the signal from both ports decreases at large fields is attributed to, and well explained by the Franz-Keldysh effect, and finally we can account for the low extinction ratio of the signal by including the reflections from the gratings. The deviations between the model and the experimental data at large negative voltages may be attributed to a stronger electroabsorption than the model predicts at this field strength. In fact, the signal from port 1 almost goes to zero at -1 V (see fig. 3.12(e)). This is not reproduced accurately in the model accounting for the discrepancy between the model and the experimental data in fig. 3.18.
Figure 3.18 only shows the comparison between model and experimental data for one wavelength, namely the emission wavelength of the quantum dot (904 nm). The model is also compared to the data obtained in the wavelength-dependent transmission measurements performed using the external laser.

Figures 3.19(a) and (b) shows the data from the transmission measurements performed using the CTL laser. The data for each wavelength is normalized using gray-scale normalization. Figure 3.19(c) and (d) show the behavior predicted by the model for the same wavelength- and voltage-range as the experimental data. The data from the model has been normalized in the same way as the experimental data in order to allow for direct comparison. The model reproduces the behavior of the experimental results well. The decrease in intensity at large reverse bias is successfully accounted for by including the Franz-Keldysh effect in the model, and the low extinction ratio is a result of the reflectivity of the gratings.

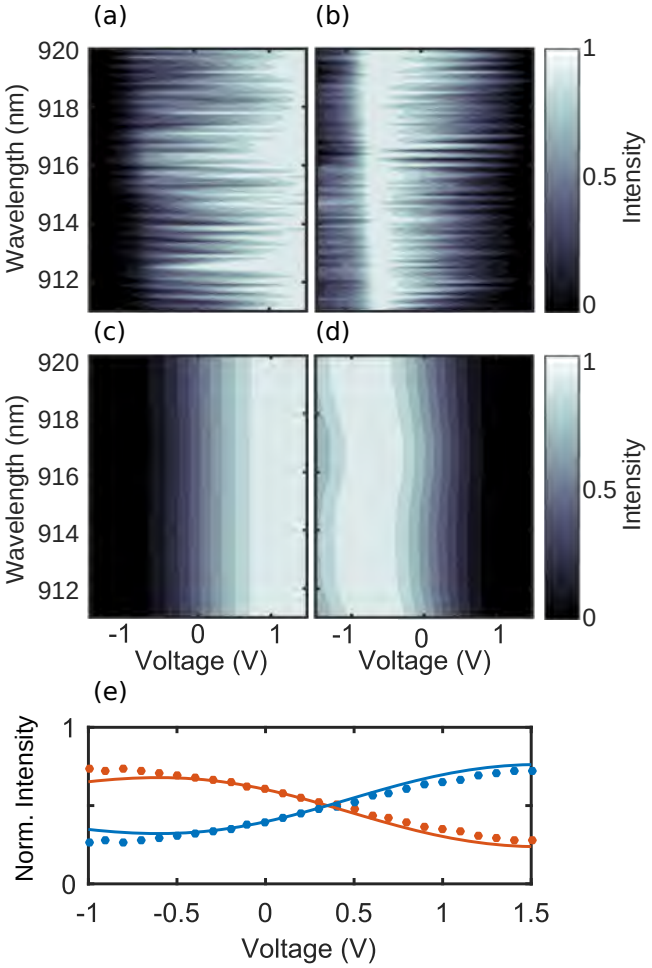

Figure 3.19: Comparing model and transmission experiment: The experimental data from the transmission measurements (**(a)**and **(b)**) and the model (**(c)**and **(d)**) that includes, propagation loss, the Franz-Keldysh effect and the reflections from the gratings. **(e):** Data from a single wavelength ($918.7\,\mathrm{nm}$) normalised to the sum of the two outputs (dots) compared to the model evaluated at the same wavelength (solid lines). The model has been fitted to the data using only one free parameter, namely the crossing point of the two curves at $0.35\,\mathrm{V}$.

In the range from $-0.5\,\mathrm{V}$ to $-1.0\,\mathrm{V}$ there is a discrepancy between the model and the data obtained from both the quantum dot experiment (fig. 3.18) and the transmission experiment (fig. 3.19(e)). The experimental data suggest that light is routed to port 2 (red data points) to a larger extent than predicted by the model. The discrepancy between model and experimental data using the laser is less pronounced but similar to the discrepancy witnessed in fig. 3.18 comparing the model to the quantum dot data. Hence, we estimate that the deviations do not stem from an effect of the electric field on the quantum dots, and is most likely due to the fact that the model assumes perfect 50:50 splitting ratios of the power-splitter and the MMI. As the deviations between the model and the experimental data are small, we conclude that the actual splitting ratios do not differ significantly from the ideal case.

3.3.5 Switching speed

An essential figure of merit for re-configurable photonic devices is the response time. In the case of switches, we are interested in the time it takes to change the output from port 1 to port 2. The time scales required depend on the desired application. Some applications require switching-times on the order of the spin coherence of the quantum dot which may be up to $1\,\mu\mathrm{s}$ [99, 100, 101]. Generation of an $(N \times 1)$-indistinguishable-photon state requires the switch to respond well within the coherence-time of the emitter. It has recently been demonstrated that indistinguishability between two photons separated in time by $14.7\,\mu\mathrm{s}$ exceeds $90\,\%$ [102].
In order to experimentally assess the switching speed of the device presented here, we perform confocal photoluminescence measurements from a quantum dot located in the switching region of the device while driving it with a periodic square-wave signal as depicted in fig. 3.20(a). The change in the integrated intensity as a function of the modulation frequency is recorded, and in this way we measure the time constant of the circuit: $\tau = RC$, where R is the resistance arising from the contacts as well as the doped layers, and C is the capacitance of the *p-i-n* junction. The time constant tells us about the time it takes to charge the capacitor through the resistor to $63\,\%$ of the final value.
The switching speed of the device is limited by the time-constant, i.e., how fast the device responds to a change in applied voltage. We measure the time constant by using the fact that the intensity of the dot depends on the applied voltage as the voltage sets the tunnelling rate of the carriers. This allows us to define a voltage $V_{off} = 0.32\,\mathrm{V}$ where the emission from the dot is completely switched off (see fig. 3.20(c)) and another voltage $V_{on} = 0.58\,\mathrm{V}$, where the dot emission is maximized (see fig. 3.20(b)). The intensity scales linearly with voltage between these values. The square-wave signal with variable frequency is applied to the switching region of

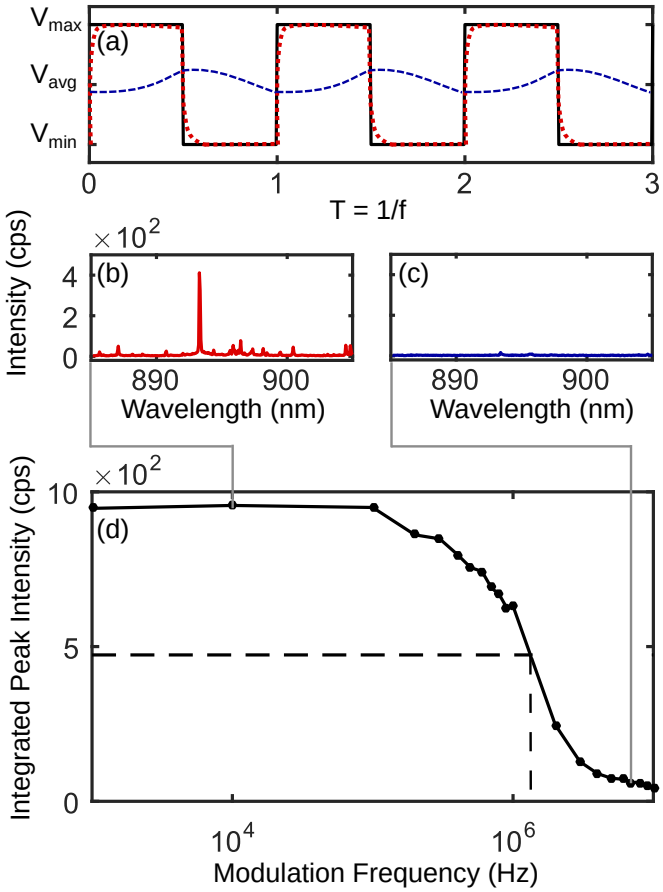

Figure 3.20: Switching speed of the device: (a): A square-wave voltage is applied to the sample, where V_{max} and V_{min} are chosen so that the quantum dot emission is maximized at V_{max} and completely turned off at $V_{avg} = \frac{V_{max} + V_{min}}{2}$. The red dash-dotted (blue dashed) line indicates the system response below (above) cut-off. **(b):** Emission from the QD when the frequency of the driving field is low. **(c):** Emission from the QD when the frequency of the driving field is high. **(d):** Integrated intensity as a function of the frequency of the driving field.

the sample and adjusted so that the maximum voltage corresponds to V_{on} and the average voltage corresponds to V_{off} (see fig. 3.20(a)). Expecting that the circuit can be modelled as a low-pass-filter, the junction voltage averages to V_{off} when the applied modulation frequency is above cut-off, thus we do not see any emission from the dot under this condition (see fig. 3.20(c)). Below cut-off the dot emits 50% of the time, and since the spectra are recorded with much longer integration time than the period of the modulation frequency, we observe emission under this condition (see fig. 3.20(b)).
Figure 3.20(d) shows the integrated intensity as a function of the modulation frequency, showing a clear low-pass characteristic. A 3 dB cut-off is extracted for approximately 2 MHz. The measurement was repeated by exciting the wetting layer in one af the arms of the interferometer. In this case a time constant of $RC = 55 \pm 8$ ns is extracted, corresponding to a 3 dB cut-off at 2.8 ± 0.5 MHz (see fig. A.2).

3.4 Conclusion and Outlook

In conclusion, we have demonstrated a compact device that deterministically routes photons between two output ports. Switching between the two ports is realized with a switching voltage -length product, $V_\pi L$, as low as 0.1 V cm. This allows for a significant reduction of the footprint compared to mm long electro-optic modulators previously fabricated on GaAs [103]. Moreover, the reconfiguration time of this device is measured to be in the sub-microsecond range.
The drawbacks of this device is the high degree of propagation loss and the low extinction ratio. The propagation loss in this work stems from the free-carrier absorption in the doped layers, but is increased further as the emission energy of the quantum dot is very close to the band edge of GaAs at 10 K, meaning that the Franz-Keldysh effect influences the propagation loss in the device.
The low extinction ratio is caused by the finite reflectivity of the gratings introducing unwanted Fabry-Perot resonances in the structure. Numerical simulations of these gratings show that the reflection back into the waveguide is around 30% resulting in a cavity forming inside the device, with resonances interfering with the desired behavior of the device, and causing a significant reduction in the achievable extinction ratio. The achievable extinction ratio of ~ 3 reported in this work means that, if we neglect other sources of loss, we can successfully generate a 4-photon state with a probability calculated from eq. (2.2): $P_{(4\times1)}(3/4) = \left((3/4)^{\log_2 4}\right)^4 \approx 10\%$. For comparison, using passive 50:50 beam splitters would yield a probability of $P_{(4\times1)}(1/2) = \left((1/2)^{\log_2 4}\right)^4 \approx 0.4\%$.
The mentioned limitations have severe consequences for the performance of the device, but as the cause is well known, they can be overcome in future routing

experiments. The propagation loss may be reduced by doping the material more lightly, and by finding a quantum emitter with emission energy further from the band gap of the host material, reducing the electroabsorption.
Battling the reflections from the gratings takes more effort as it includes designing and fabricating a new type of gratings [88] that do not reflect light back into the structure to the same extend as the circular gratings used in this work.
From simulations it should be possible to increase the extinction ratio from the current ~ 3.3 to ~ 74 by using gratings with a reflectivity of 1%. If we envision a fully integrated device where the generation, manipulation, and detection [104] all take place on a single chip, the extinction ratio would not be limited by reflections. However, such a chip is yet to be realized and for now we must look into ways of coupling light from the chip with minimal back-reflections into the circuit.
The next chapter describes how such gratings have been designed, optimized and experimentally characterized.

Chapter 4

Shallow-etched gratings

4.1 Introduction

By adding one more step in the fabrication process of out-couplers we achieve a five-fold increase in the chip-to-fiber coupling-efficiency as well as a significant reduction in back-reflections into the structure. The design is robust against fabrication imperfections, and the yield of working devices is close to 100 %.
This chapter describes the design and characterization of a shallow-etched grating-coupler that outperforms the second order bragg gratings previously used, in terms of increased chip-to-fiber coupling, and reduced backscattering into the waveguide. The new design is well known from silicon photonics where simulations predict coupling efficiencies between 80 and 95 % [88]. The design is adapted for a working wavelength of 930 nm, which is the emission wavelength of the InAs quantum dots used in this work. Based on numerical simulations, the design is tested in order to assess the sensitivity of the design to fabrication imperfections and the bandwidth of the grating. Additionally the performance of the shallow-etched gratings is compared to second order Bragg gratings (referred to as circular gratings) used up until now in the group, and the achievable advantage is calculated as the increase in chip-to-fiber efficiency when replacing circular gratings with shallow-etched gratings. Lastly, an attempt to separate the in- and out-coupling efficiencies from the experimental data is presented. This is done by comparing transmission measurements of waveguides terminated by different types of gratings. This work is complicated by the fact that the structures are fabricated on a wafer with a substrate thickness optimized for the shallow-etched gratings, and a direct comparison between the two types of gratings is thus biased, as the performance of the circular gratings is sub-optimum at this substrate-thickness. For this reason a comparison to simulated data is presented as well.

4.2 Theory

There are several advantages in using surface couplers for off-chip coupling, however it also poses a major challenge in that the light has to make a dramatic change in direction from the on-chip propagation in the waveguide to the objective. Grating couplers offer a solution to this challenge [88]. They consist of a periodic modulation of the refractive index, realized by periodically etching away small grooves as illustrated in fig. 4.1(a). These grooves and teeth then act as scatterers, and the scattered contributions interfere constructively in the vertical direction as can be understood from the Huygens-Fresnel principle. More specifically, when light with a given wavelength propagates from left to right, as illustrated in fig. 4.1(a), a certain combination of the period of the grating Λ, the off-chip angle θ and the wavelength of the light λ will cause the the scattered light to be in phase, forming a coherent phase-front radiating away from the chip [105]. This is known as the Bragg condition and is fulfilled whenever the phase delay between two consecutive teeth is exactly $n \cdot 2\pi$, where n is an integer. Figure 4.1(b) illustrates the operational principle in k-space. The diffraction grating has its own momentum $K = 2\pi/\Lambda$, which is transferred to the light propagating in the waveguide with waveguide propagation constant $\beta = \frac{2\pi n_{eff}}{\lambda_0}$. Here, n_{eff} is the effective index in the waveguide, and λ_0 is the free-space wavelength of the light. From conservation of momentum in the x-direction, we get from fig. 4.1(b) that

$$\beta - k_x = mK, \tag{4.1}$$

where m is the diffraction order. The momentum of the diffracted light projected onto the x-direction can be written as $k_x = k\sin(\theta_m)$, and we arrive at an expression for the Bragg condition for the mth order diffraction in terms of the grating period, Λ, the emission angle θ, the effective index of the grating n_{eff}, and the wavelength of the light, λ_0

$$n_{eff} \cdot \Lambda - n_0 \sin(\theta_m) \cdot \Lambda = m \cdot \lambda_0 \tag{4.2}$$

Here n_0 is the refractive index of the surrounding medium.
If we choose to design the grating such that the light is emitted directly up, i.e., $\theta_1 = 0°$, then it follows from eq. (4.1) that $\beta = K$. This type of grating is called a second order grating because there is also a solution for $m = 2$ where the grating can now reflect light back into the waveguide. This leads to unwanted Fabry-Perot resonances in the structure. For this reason, the grating couplers are designed to have off-vertical emission restricting the solution to only the case where $m = 1$ and eq. (4.2) can be simplified to

$$n_{eff} - n_0 \sin(\theta) = \frac{\lambda_0}{\Lambda}. \tag{4.3}$$

The task is to design the grating such that the effective index n_{eff}, which can

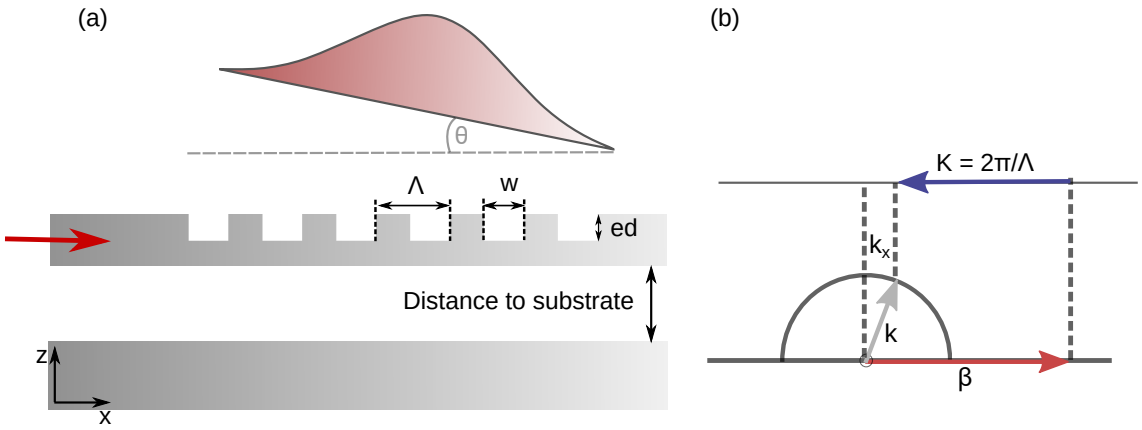

Figure 4.1: Working principle of a shallow-etched grating: (a): Light from a waveguide enters the shallow-etched grating from the left. The grating has a pitch of Λ, a fill factor $\frac{w}{\Lambda}$, and an etch depth, ed. Light from the grating is scattered at an angle θ in order to minimize reflections back into the waveguide. The distance to the substrate must be chosen such that the interference between light scattered from the grating, and light reflected from the substrate interfere constructively in the direction of emission. **(b):** Operating condition for a grating coupler in *k*-space. The light is emitted at an angle given by $\arcsin(k_x/k)$. The grating has its own momentum K which is transferred to the light travelling in the waveguide with propagation constant β.

be calculated as the weighted average of the etched and un-etched regions [106], matches the targeted wavelength, emission angle and grating period. This can be modulated by changing the geometry of the grooves and teeth, hence, by changing the etch depth (ed) and the fill factor (ff = w/Λ). From eq. (4.3), we see that for a fixed geometrical design, i.e., a fixed n_{eff} and Λ, a change in the wavelength of the light will cause a change in the emission angle.

Extending the grating into the 3rd dimension with straight grooves poses a problem in that the sub-micron waveguide mode has to be matched to the mode of the light accepted into a fiber. Hence, a tapering section is needed as illustrated in fig. 4.2(a). This tapering section will have to be very long ($\approx 100\mu m$) in order to maintain a high conversion efficiency, which compromises the compactness of the circuits. For this reason it is desirable to use confocal gratings [107], where the grooves and teeth are curved elliptically with a common focal point as illustrated in fig. 4.2(b).

The grating-ellipses are defined from

$$\text{Semi major axis} = \sqrt{\frac{q\lambda n_0 \sin(\theta) + q^2\lambda^2}{n_{eff}^2 - n_0^2 \sin^2(\theta)}},$$
$$\text{Semi minor axis} = \sqrt{\frac{q^2\lambda^2}{n_{eff}^2 - n_0^2 \sin^2(\theta)}}, \tag{4.4}$$

where q is an integer number for each grating line, θ is the emission angle, n_0 is the index of the surrounding material (air in our case), n_{eff} is the effective index of the grating and λ is the targeted wavelength for optimum operation. In order to

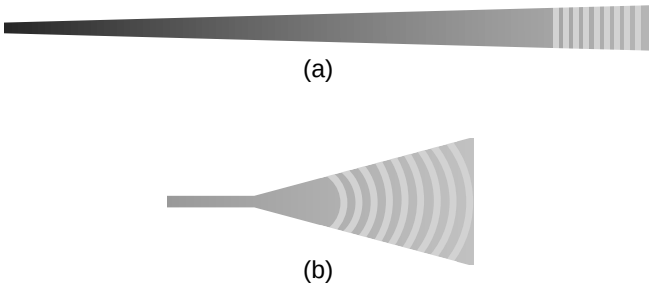

Figure 4.2: Tapering solutions for shallow-etched gratings: (a): Shallow-etched grating coupler with linear tapering section. **(b):** Focused shallow-etched grating, where the grooves are confocal ellipses.

ensure a common focal point of the ellipses, they are translated in the horizontal direction by

$$x_0 = \frac{q\lambda n_0 \sin(\theta)}{n_{eff}^2 - n_0^2 \sin^2(\theta)}. \tag{4.5}$$

Figure 4.3 shows the ellipses defined from eq. (4.4), where the left focal point of all the ellipses has been overlapped using eq. (4.5).

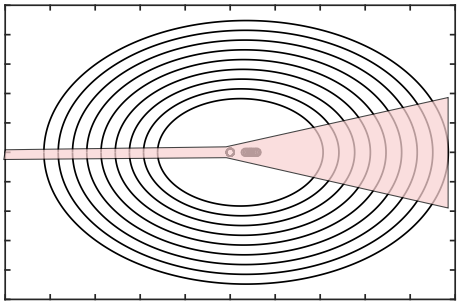

Figure 4.3: Ellipse design: Ellipses are defined according to eqs. (4.4) and (4.5). The overlapping foci are matched to the point where the tapering section of the grating starts.

4.3 Finite element model

In order to optimize the design of the grating couplers, they are simulated in the finite element (FE) software COMSOL using the RF module. A 2D model is initially employed in order to find the optimum parameters (Λ, *ff, ed*, distance to substrate). The optimum parameters are then used to set up a model in 3D. The data from the 3D model is analysed, and the transmission is evaluated as an overlap with a symmetric gaussian mode, as we are ultimately interested in coupling the light from the gratings into a fiber and thus matching the mode from the grating to the mode of the fiber. The fabrication robustness is tested by running tolerance tests in 3D. Furthermore, the bandwidth of the device is tested using the 3D model.

4.3.1 2D model

From the grating equation (4.3) and the design parameters used to define single-moded suspended waveguides (slab thickness = 160 nm, waveguide width = 300 nm) we can give initial guesses for the values of the pitch, fill factor and etch depth that ensures constructive interference in the desired direction θ at the desired wavelength $\lambda = 930\,\text{nm}$. In order to validate these initial guesses and test the tolerance of the design, a 2D model is set up in COMSOL. The model is shown in fig. 4.4(a). The leftmost boundary is set as a port, i.e., a boundary at which the electric field is initially calculated in a boundary mode analysis. This gives us the fundamental mode of the structure. The pre-calculated mode is now used to excite the input port, and the field distribution is calculated using the finite element method, which is a numerical method for the solution of the partial differential equations governing the evolution of the electric field. The computational domain is discretised using a free triangular mesh. The size of the mesh is chosen so that a full period of the wave is evaluated at minimum four distinct points. Hence the size of the mesh is given by $\delta = \frac{\lambda}{4n}$, where n is the refractive index of the material. The size of mesh is therefore approximately 3.5 times finer in the GaAs region than it is in the regions containing air as can be seen in the inset in fig. 4.4(a). The power transmitted upwards is evaluated over the boundary indicated with blue in the figure. The boundary is meshed with the same mesh size as the GaAs waveguide. The power reflected back into the waveguide is evaluated in the software using the S_{11} matrix-element of the transfer matrix. Figure 4.4(b) shows the absolute value of the field $|E_z(x,y)| = \sqrt{E_{R,z}^2(x,y) + E_{I,z}^2(x,y)}$. This figure shows the amplitude of the field, and we see how it is predominantly scattered upwards at an angle off-vertical in order to avoid backscattering as mentioned in the previous section. Figure 4.4(c) shows the real part of the z-component of the field $E_z(x,y)$, and thus contain the phase information $E_R = |E| \cdot \cos\phi$.

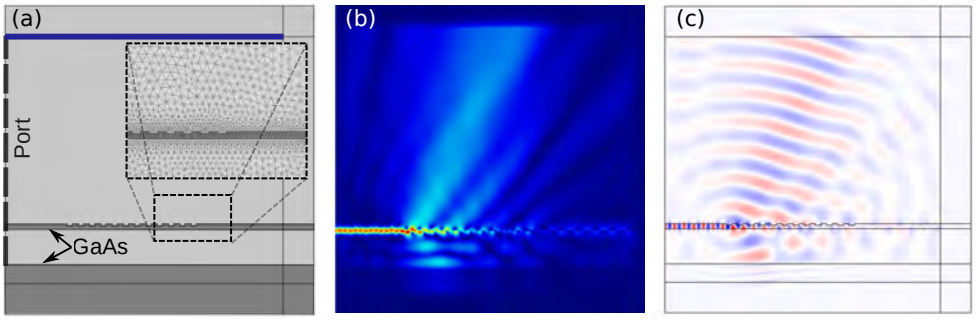

Figure 4.4: 2D COMSOL model: (a): An illustration of the 2 dimensional model used in the simulations. The leftmost boundary is defined as a port, and the transmission is evaluated through the top boundary. The computational domain is surrounded by phase matched layers (PMLs) except at the port boundary. The size of the mesh elements is chosen so that a full period of the wave is evaluated at 4 distinct points, making the mesh-size in the high index GaAs regions much smaller than in the air domains. **(b):** Electric field distribution of $|E_z(x, y)|$.**(c):** Electric field distribution of $E_{R,z}(x, y)$. In both cases the wavelength is 930 nm.

Initially the distance to the substrate is varied while keeping the remaining variables fixed: $\lambda = 930\,\text{nm}$, $\Lambda = 0.365\,\mu\text{m}$, *ff*=0.5 and *ed*= 50 nm. It is found that a substrate distance of 1.15 µm maximises the upward emission due to constructive interference.
Keeping the substrate distance fixed at this value, the wavelength is swept for different values of the pitch (Λ), etch depth (ed) and fill factor, and the transmission upwards as well as the reflections back into the structure is calculated.
An initial guess for the pitch is calculated from considerations of the target wavelength (930 nm) and emission angle (15°) and yields a value of 0.365 µm. We keep the etch depth fixed at 50 nm, and use a constant fill factor of 0.5, and then change the pitch while sweeping the wavelength.
As seen from eq. (4.3), changing the grating pitch changes the wavelength for which the grating is optimized, so we expect to see a shift of the grating spectrum towards longer wavelengths when the pitch is increased.

Figure 4.5(a) shows wavelength sweeps for five different values of the pitch. The yellow curve is the initial guess for the pitch of 0.365 µm and it shows maximised transmission between 900 nm and 950 nm as desired. Increasing the pitch by 20 nm (purple curve) has the expected effect of shifting the maximum transmission to longer wavelengths, while decreasing the pitch by 20 nm (red curve) shifts the maximum transmission to shorter wavelengths. The blue curve corresponds to a pitch 40 nm smaller than the initial guess. In this case it is difficult to determine the wavelength range with the highest transmission, but looking at the sharp transmission dip, it is evident that the decrease in pitch shifted this to shorter wavelengths. The green curve corresponds to a 40 nm increase in the pitch, leading to a significant shift towards longer wavelengths, but also an overall decrease in perfor-

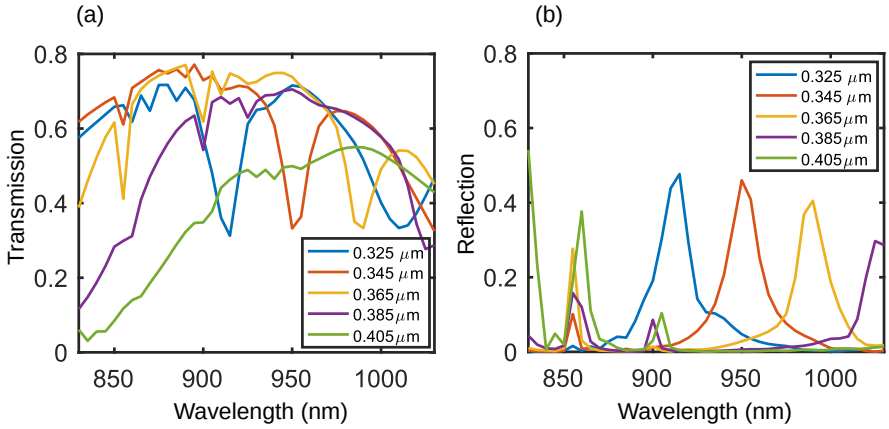

Figure 4.5: Effect of Λ on upward transmission and reflection: (a) Transmission through the top boundary indicated in fig. 4.4(a). **(b)**. Reflections back into the waveguide. Both evaluated as a function of wavelength for different values of the pitch.

mance of the grating. Figure 4.5(b) shows the reflections back into the waveguide as a function of wavelength for the five different values of the pitch. Here we see that a decrease in the pitch of 20 nm (red curve), shifts the maximum reflection to shorter wavelengths, while increasing the pitch by 20 nm (purple curve) shifts the maximum reflection to longer wavelengths. From these curves we can estimate a so called tuning coefficient for the gratings. This coefficient tells us how much a change in the pitch shifts a given feature in the transmission/reflection spectrum; $\frac{d\lambda}{d\Lambda}$. In this case, the tuning coefficient is estimated from the transmission dips in fig. 4.5(a) and the reflection peaks in fig. 4.5(b), and is approximately 2. Hence a change in the pitch of 1 nm, causes a shift in transmission dip/reflection peak of 2 nm.

Changing the etch depth changes the effective index of refraction. As the etch depth is increased the index in the etched areas decreases, meaning that the overall effective index decreases. As the central wavelength of the grating is proportional to the effective index, we assume the central wavelength of the grating to be inversely proportional to the etch depth. We keep the pitch and fill factor fixed at 0.365 µm and 0.5 respectively, and sweep the wavelength for different etch depths. From fig. 4.6(a) we see that an etch depth of 50 nm (yellow curve) gives a high transmission between 900 and 950. As expected, an increase in the etch depth causes a shift in the central wavelength towards shorter wavelengths. Reducing the etch depth to 30 nm (red curve) not only shifts the central wavelength to longer wavelength, it also reduces the efficiency of the grating. This is even more pronounced for the case of the etch depth of 10 nm (blue curve). This is because the index contrast between the waveguide and the grating section is so small, that the light is only weakly guided upwards. This also affects the reflections as can be seen from fig. 4.6(b). A very shallow etch depth will cause very weak reflections back into the structure. When the etch depth is 50 nm (yellow curve), we see pronounced reflec-

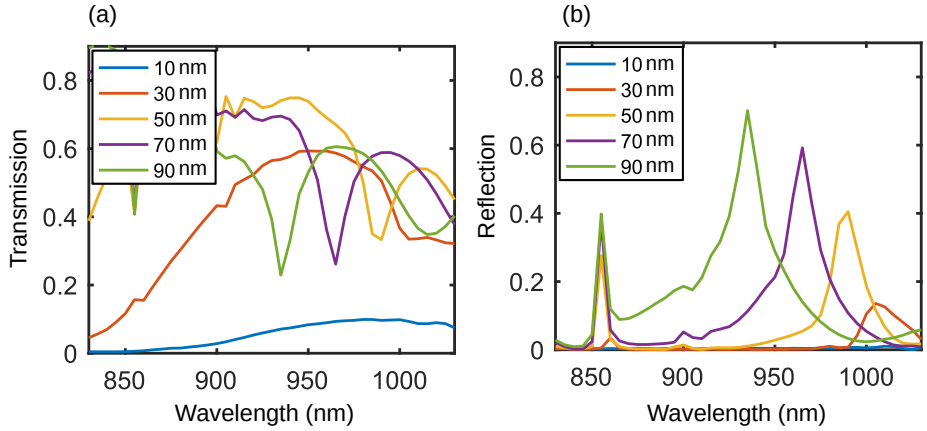

Figure 4.6: Effect of *etch depth* on upward transmission and reflection: (a): Transmission upwards through the top boundary and **(b):** reflections back into the waveguide as a function of wavelength for different values of the etch depth. As expected the spectrum blue-shifts when the etch depth is increased.

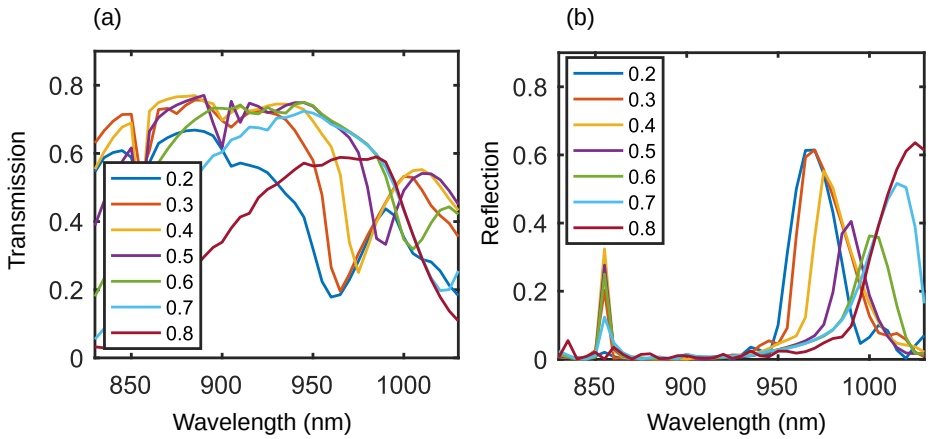

Figure 4.7: Effect of *Fill Factor* on upward transmission and reflections: (a): Upward transmission and **(b):** reflections back into the waveguide as a function of wavelength for seven different values of the fill factor. As we expect from the grating equation, the spectrum blue-shifts when the fill factor is increased.

tions at wavelengths much longer than the wavelengths we are interested in. This reflection peak shifts towards shorter wavelengths when the etch depth is increased. Hence the optimum etch depth to achieve high transmission and low reflections at 930±20 nm is 50 nm. A tuning coefficient for the etch depth was evaluated from the transmission dips and the reflections peaks, and is yields: $\frac{d\lambda}{d\mathrm{ed}} = -1.25$.
Finally we investigate the effect of the fill factor on the transmission and reflection of the grating. The fill factor affects the grating performance by affecting the effective refractive index. When the fill factor defined as $ff = \frac{w}{\Lambda}$ (see fig. 4.1(a)) increases, the effective index increases, shifting the grating spectrum towards longer wavelengths as can be seen from eq. (4.3). The behavior seen in figs. 4.7(a) and (b) correspond to the expectations based on the grating equation (eq. 4.3). The curve corresponding to a fill factor of 0.5 (purple curve in fig. 4.7(a)), has a broad plateau

in transmission between 900 nm and 950 nm. When the fill factor is increased (decreased) this plateau shifts to longer (shorter) wavelengths, and the maximum transmission decreases. The same trend is seen in the reflections (fig. 4.7(b)), where the spectral features shift with the fill factor. A tuning coefficient of $\frac{\delta\lambda}{\delta w} = 0.33$ is calculated for the fill factor.
In order to achieve high transmission and low reflections in the wavelength range around 930 nm, we use a target fill factor of 0.5 in the further simulations.
We now have a set of parameters to use as a starting point for the 3D simulations. The pitch is set to 0.365 μm, the etch depth is 50 nm and the fill factor is 0.5. These values are optimum for maximized transmission and minimized reflections in the wavelength range from 900 to 950 nm. From the tuning coefficients we can get an estimate of the effects of the unavoidable fabrication imperfections. The uncertainties in the pitch are negligible[1], however there are uncertainties related to the etch depth and the fill-factor. These two are connected as an increase in the fill-factor, caused by over-etching, will be accompanied by a slightly larger etch depth. As the tuning coefficients for the fill factor and etch depth have opposite signs, this means that a slight over- or underetching will not affect the spectrum significantly. The uncertainties related to the fill factor and etch depth are estimated to be within 10 %, which means that we can reach an accuracy of ± 5 nm for the etch depth. From the tuning coefficient we estimate that this would result in a shift of the spectrum of ± 6 nm. A 10 % uncertainty in the fill factor means that we can fabricate the target $w \pm 18$ nm. From the tuning coefficient of the fill factor, we predict a corresponding shift of ± 6 nm.

4.3.2 3D model

Now that we have a set of values to use for the initial design of the gratings, we go on to set up a 3D model for further numerical simulations. The grating is built up according to the model depicted in fig. 4.2(b). Due to symmetry considerations we only have to model half of the structure as shown in fig. 4.8. The overlapping foci of the ellipses (see fig. 4.3) are overlapped with the point where the tapering section starts. The shallow-etched regions are defined from eqs. (4.4), where the central wavelength of the grating is chosen to be 930 nm, as the quantum dots in our samples are targeted to have a central wavelength of 930 nm. The first groove of the grating corresponds to $q = 11$, followed by another 11 grooves. See fig. B.1 in the appendix for the results of sweeping q and the number of grooves. The angle of the tapering section is chosen so that the emission from the grating is as symmetric as possible, maximizing the coupling into a fiber. Figure 4.8 shows the model used for the numerical simulations. The zoomed region shows the shallow-etched regions.

[1] The uncertainties are estimated by Irina Kulkova from Sparrow Quantum, who also fabricated the samples used in the experimental characterization

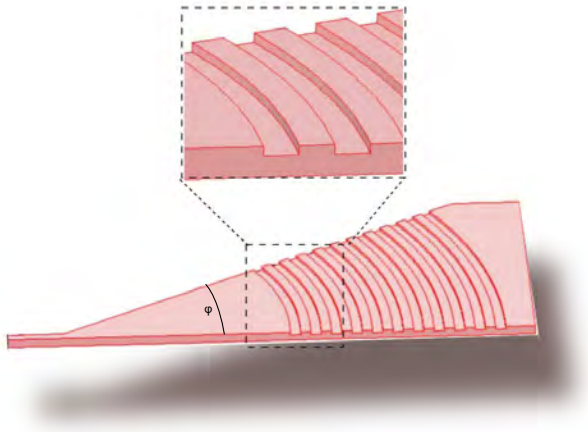

Figure 4.8: 3D model of the grating: The grating is simulated using the FE-analysis software COMSOL. Due to symmetry in the structure, only half of the grating need to be simulated. The half-angle of the tapering region is $\phi = 20°$, and the first groove of the grating corresponds to $q = 11$. The zoomed region shows the shallow-etched regions defined according to eq. (4.4). The grating is optimized for a wavelength of $\lambda = 930$ nm, and emission angle of $\theta = 9°$.

The procedure is similar to that employed for the 2D simulations; an input port is defined and a preliminary boundary mode analysis calculates the fundamental mode of the port, and subsequently uses this to excite the structure. The meshing is done in the same way as in the 2D simulations.

The GaAs substrate is neglected in these simulations due to the fact that it increases the degrees of freedom of the computation significantly as this region must be meshed with high resolution due to the large refractive index of the material. The effect of the substrate is to reflect the light that is emitted downwards, and by choosing the right distance to the substrate, we can make sure that the light emitted upwards interferes constructively with the light reflected from the substrate. A substrate-distance sweep for $\lambda = 930\,\text{nm}$ confirms the result from the 2D simulation and yields an optimum substrate distance of $1.15\,\mu\text{m}$ as is shown in fig. B.2. The overall behavior of the gratings is assumed to be independent of the presence of a substrate, and the effect is included as a scaling factor in the final results. A selected number of simulations are done with and without substrate in order to quantify the effect of the substrate, and determine the scaling factor (see fig. B.2).

Figure 4.9(a) is a top view of the grating when exciting the input port with 930 nm. It shows the y-component of the normalized electric field as it propagates in the plane of the grating. The wavefronts of the field are almost perfectly aligned with the grooves of the grating. The fact that they do not match exactly, is a result of the emission angle θ, as can be seen from eq. (4.3). Figure 4.9(b) is a side view of the field emitted from the grating. The field is predominantly scattered upwards at an angle as dictated by the design parameters. Figure 4.9(c) shows the

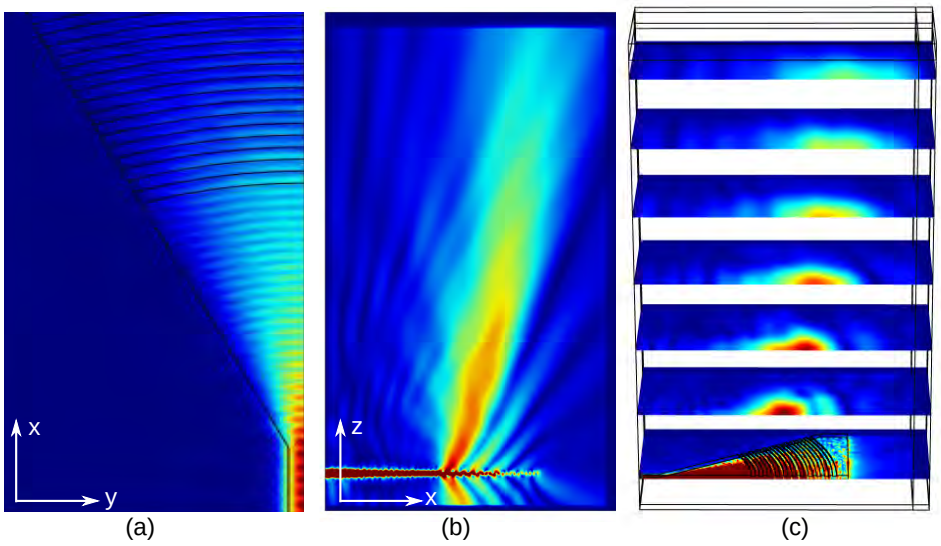

Figure 4.9: Field distribution: (a): The normalized field in the xy-plane evaluated at the grating (z=0). The wavelength of the light is 930 nm, i.e., the target wavelength for the grating design. The wavefronts of the field follow the grooves of the grating. **(b)**: The normalized field projected onto the xz-plane at y=0. The field is predominantly scattered upwards at an off-vertical angle. The fringes indicate that there is some interference due to reflections from the port boundary. **(c)**: An illustration of the horizontal planes at which the field is fitted to a Gaussian in order to evaluate the position of the beam as well as the divergence angle, which can be found from the width of the beam.

beam propagation evaluated at seven distinct planes in the z-direction. In order to evaluate the emission angle, a horizontal plane was moved upwards and the field is fitted to a Gaussian at each plane, and from the fits we determine the propagation direction. We now define a plane normal to the emission, and evaluate the overlap with a Gaussian in the xy-plane of the new tilted coordinate system. The Gaussian overlap is evaluated from the following integral [108]

$$O = \frac{|\iint E(x,y)e^{-i\phi(x,y)} * e^{-(x-x_0)^2/2\sigma_x^2-(y-y_0)^2/2\sigma_y^2}\mathrm{d}x\mathrm{d}y|^2}{\iint|e^{-(x-x_0)^2/2\sigma_x^2-(y-y_0)^2/2\sigma_y^2}|^2\mathrm{d}x\mathrm{d}y \iint|E(x,y)e^{-i\phi(x,y)}|^2\mathrm{d}x\mathrm{d}y}. \tag{4.6}$$

Hence O calculates the overlap between the electric field, $E(x,y)e^{-i\phi(x,y)}$, evaluated in the xy-plane (in the tilted coordinate system), and a 2-dimensional Gaussian with center in (x_0, y_0), and widths given by σ_x and σ_y. In the data analysis, we force the Gaussian to be symmetric, i.e., $\sigma_x = \sigma_y$, and evaluate the overlap with this symmetric Gaussian. This is because we eventually want to couple the mode emitted from the grating to a fiber with a symmetric Gaussian mode.
Figure 4.10(a) illustrates an angled plane over which the overlap in eq. (4.6) is evaluated, and the grating efficiency may now be calculated as the power emitted up through the top-plane (in analogy with the 2 dimensional case. See fig. 4.4) multiplied by, the overlap between the field projected onto the tilted plane and the fitted Gaussian, squared.

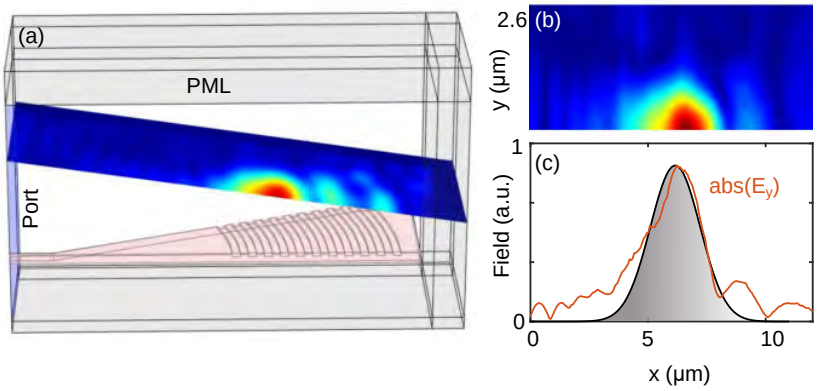

Figure 4.10: Overlapping with a Gaussian: (a): A plane normal to the beam is defined and the overlap is evaluated between the field projected onto this plane and a symmetric Gaussian. The plane is positioned sufficiently far from the grating to assure that the overlap is evaluated in the far field ($> 2 \cdot \lambda$). **(b)** Field distribution of the absolute value of the y-component of the field projected onto the tilted plane. **(c):** The grey shaded area is the Gaussian that is fitted to the y-component of the field. The red line is the absolute value of the y-component of the field.

The reason for this way of evaluating the efficiency of the gratings rather than using the built-in far-field analysis in the software, is that this version of the software[2] cannot calculate the far field from inhomogeneous media with multiple scatterers [109]. For this reason the above mentioned strategy was employed, where a careful analysis of the convergence was performed with respect to the distance from the slab to the plane over which the overlap was evaluated (see fig. B.3). Figure 4.10(b) shows the y-component of the electric field projected onto the tilted plane indicated in fig. 4.10(a). Subfigure (c) shows the absolute value of the y-component of the field evaluated at y=0 in the computational domain (red curve) overlapped with the Gaussian (solid grey area). Some initial tolerance tests of the pitch (Λ), etch depth (ed) and fill factor (ff) were performed yielding the same optimized values as the 2D-model. Using these geometrical parameters the structure is excited with different wavelengths and the efficiency of the gratings is evaluated as mentioned in the previous.

Figure 4.11 shows the wavelength sweep of the chip-to-fiber coupling efficiency of the grating. The dots correspond to the output of the simulations, where only the red dots have been fitted to a Gaussian in order to assess the bandwidth of the grating. The dashed black line indicates the reflections back into the structure. From the Gaussian fit, we get a central wavelength of 926.2 $\pm$0.8 nm, a maximum efficiency of 55.3 $\pm$1.8 %, and a full width half max (FWHM) value of 51.8 $\pm$ 2.0 nm. This is comparable to the bandwidths stated in the literature [110, 111] of 45 nm and $\sim$ 75 nm respectively. The reflections back into the structure are below 5% up until 940 nm (2.6 % at 930 nm). These results show that at the target wavelength,

[2]COMSOL 4.3b

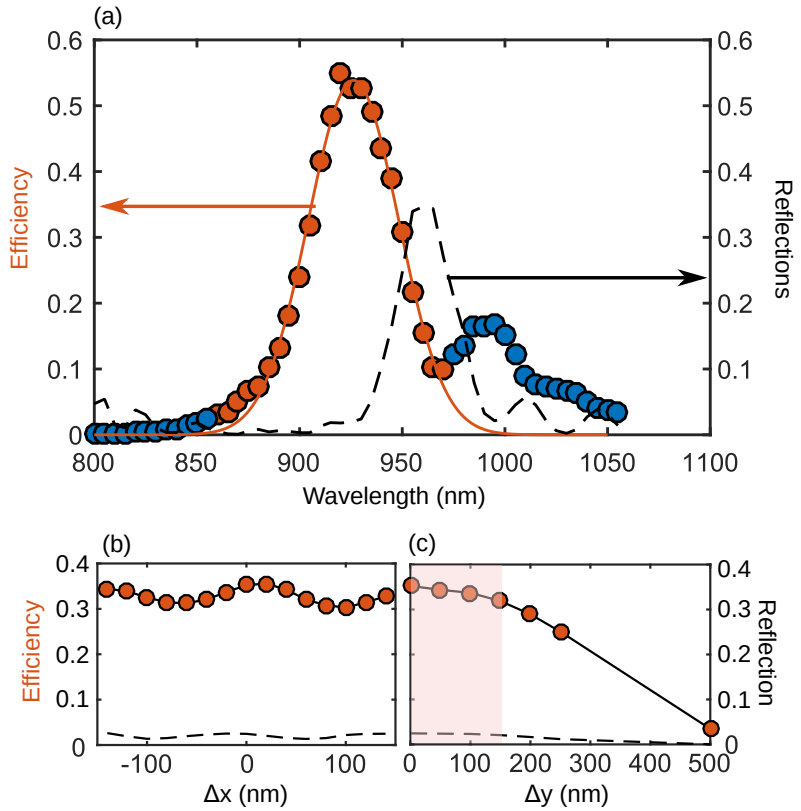

Figure 4.11: Wavelength sweep and tolerance test: (a): The dots show the calculated efficiency of the gratings evaluated as described in the main text. The red dots are fitted to a Gaussian. The black dashed line shows the reflections back into the structure. **(b):** The foci of the ellipses is shifted in the x-direction, and the efficiency of the grating is evaluated using the above mentioned procedure. **(c)**: The efficiency of the gratings as a function of the displacement of the foci in the y-direction. The shaded area indicated the waveguide width in the y-direction. In both plots, the black dashed lines show the reflections back into the structure.

the gratings have an efficiency of approximately 55%, while reflections are kept below 5%.
These results stem from simulations initially done *without* a substrate in order to increase the computational efficiency. However, the presence of the substrate will cause an increase in the efficiency due to the constructive interference of the light transmitted upwards, and the light reflected from the substrate. This has been taken into account by multiplying by a *substrate/no substrate* ratio that has been calculated from simulations done at the target wavelength of 930 nm (see fig. B.2). As the interference-effects are naturally wavelength dependent, this method is not perfectly accurate at wavelengths far detuned from the target wavelength.

The main challenge in the fabrication of the gratings is aligning the sample before the final etching step. In this last etching step, the grooves of the gratings are etched into the suspended triangular slab. The effect of misalignment in this fabrication step is evaluated, by moving the foci of the ellipses in the x- and y-directions respectively. The aim is to overlap the foci of the ellipses with the center of the wavelength at the point where the tapering section starts. The uncertainty in the position in this last etching step is estimated to be approximately 50 nm. Figure 4.11(b) shows how the efficiency depends on the position of the foci in the x-direction. Displacing the foci by 100 nm in either direction on the x-axis causes a decrease of approximately 14%. If the displacement is kept within 40 nm, the decrease is limited to around 4 %. In the y-direction we see a decrease in efficiency of 2% when the focal points of the ellipses are shifted by 50 nm (fig. 4.11(c)). These results indicate that the gratings are robust against realistic misalignment in the last fabrication step and we expect a high achievable yield of the fabrication.

Comparing to circular gratings

The gratings described in the previous sections require two etching steps in the fabrication process. We are interested in comparing their performance to the gratings that were previously used, that only require one etching step and are thus less demanding in terms of fabrication. These gratings, which we will call circular gratings in the following, are second order Bragg gratings described in [63]. They consist of a $\lambda/(2n)$ pitch circular grating that causes destructive interference in the forward propagation direction and scatters the light vertically. The model used in the simulations can be seen in fig. 4.12(a). We have used the mirror symmetry in the xz-plane to reduce the computational domain to half the structure. The circular gratings are simulated in the same way as the shallow-etched gratings, only in these simulations the substrate is included, as the performance of these gratings depends sensitively of the interference between the light transmitted upwards, and the light reflected from the substrate. This is because of the symmetry in the z-direction, which has been broken in the case of the shallow-etched gratings. Moreover, the computational domain/degrees of freedom in this model is significantly smaller than the case of the shallow-etched gratings allowing us to include the substrate, without a significant increase in computation time. When comparing the two types

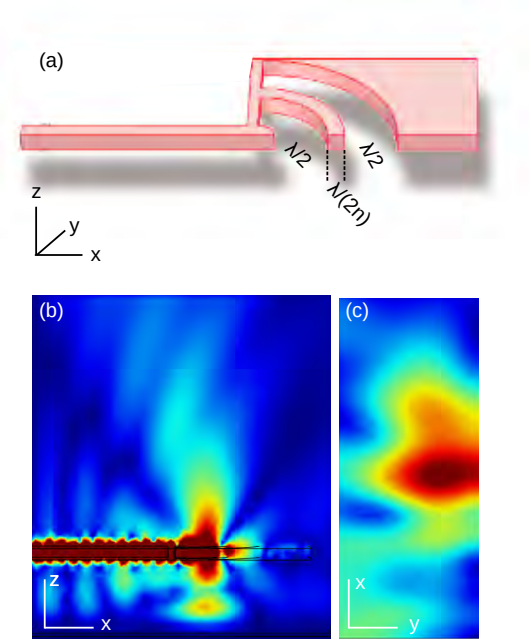

Figure 4.12: Circular grating: (a): The model used in numerical simulations of the circular gratings. The air-gaps are $\lambda/2$ wide, while the bridge is $\lambda/(2*n)$, where n is the refractive index of the material (GaAs in this case). The target wavelength is 930 nm. **(b):** Normalized field projected onto the xz-plane. The field is emitted in the vertical direction. **(c):** Normalized field projected onto the xy-plane at z=3.0μm.

of gratings, this is taken into account.
From fig. 4.12(b) we see that unlike the case of the shallow-etched gratings, the circular gratings emit in the field vertically. While this might make the collection of the light into an objective more efficient, it inadvertently introduces significant reflections back into the waveguide as explained in section 4.2. Figure 4.12(c) shows the emitted field projected onto the xy-plane evaluated 3 µm above the grating. It is evident that the emitted field is not Gaussian, making mode matching to a fiber inefficient. The evaluation of the coupling efficiency of these gratings is done in the same way as the shallow-etched gratings, only this time, the plane over which the overlap integral is evaluated is horizontal.

Figure 4.13 shows the result of the numerical simulations evaluated at different wavelengths. The Gaussian fit yields a maximum achievable efficiency of 20% at a central wavelength of 975.1 ± 3.4 nm. The bandwidth is calculated as the FWHM and is 122.7 ± 8.3 nm. The central wavelength is thus red-shifted compared to the targeted central wavelength of 930 nm. This is due to the fact that the distance to the substrate in these simulations is the same as substrate-distance used for the shallow-etched gratings, i.e., 1.15 µm, which was found to be optimum for the shallow-etched gratings. The optimum substrate-distance for the circular gratings is 1.40 µm, and the effect of the sub-optimum substrate-distance is a red-shift of the grating spectrum. This can to some extent be compensated by changing the

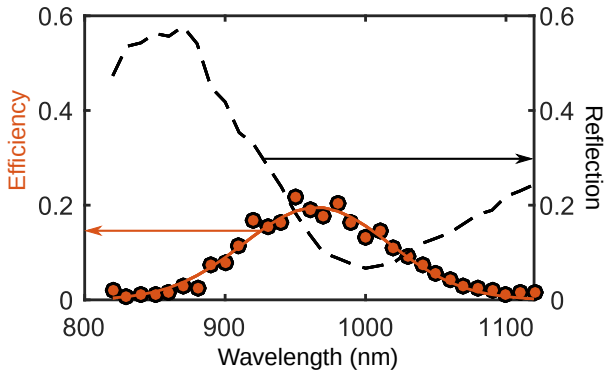

Figure 4.13: Wavelength sweep for the circular grating: The efficiency of the circular gratings is evaluated as a function of the wavelength. The dots show the result of the numerical simulations, while the solid red line shows a Gaussian fit to the data. The black dashed line shows the reflections back into the waveguide.

geometry of the circular gratings as illustrated in fig. B.4 in the appendix.
We thus compare the shallow-etched gratings with a substrate-distance of 1.15 µm to the circular gratings with a substrate-distance of 1.40 µm. However, in the experiment, a common substrate-distance of 1.15 µm is used for both types of gratings.

	Shallow-etched: Dist. = 1.15 µm	**Circular: Dist. = 1.40 µm**	**Circular: Dist. = 1.15 µm**
$\lambda_{\mathbf{central}}$	926.2 nm	930.0 nm	975.1 nm
Eff. @ $\lambda_{\mathbf{central}}$	55 %	21 %	20 %
Eff. @ 930 nm	54 %	21 %	16 %
Ref. @ $\lambda_{\mathbf{central}}$	2 %	26 %	12 %
Ref. @ 930 nm	3 %	26 %	33 %
Bandwidth	51.8 nm	122.7 nm	76.4 nm

Table 4.1: Results of simulations: Overview of the results of the simulations of the shallow-etched gratings with a distance to the substrate of 1.15 µm, as well as the circular gratings with a substrate distance of 1.40 µm, and the circular gratings with a substrate distance of 1.15 µm.

Table 4.1 shows some of the results of the simulations in the case of the shallow-etched gratings, the circular gratings with a substrate distance of 1.40 µm and the circular gratings with a substrate distance of 1.15 µm. From the two last columns we see that changing the distance to the substrate from 1.40 µm to 1.15 µm causes a decrease in the efficiency at the target wavelength of 930 nm of 5 p.p., and an increase in the reflections at 930 nm of 7 p.p.. By comparing columns one and two, we estimate an increase in transmission efficiency of 33 p.p. and a decrease in reflections of 23 p.p. at 930 nm. However, the experimental comparison will be between the structures represented by columns one and three, and comparing those we estimate an increase in transmission of 38 p.p. and a decrease in reflections of 30 p.p.. Both cases indicate that despite the added processing step in the fabrication, the increase

in performance makes the shallow-etched gratings very attractive for chip-to-fiber coupling.

4.4 Experimental results

The simulations suggest that the shallow-etched gratings offer a significant advantage over the circular gratings in terms of both transmission efficiency and reducing back-reflections. In order to experimentally verify the findings from the simulations, a sample with both circular and shallow-etched gratings is fabricated on the same wafer, and their performance is evaluated from transmission measurements. The sample is placed in a flow cryostat, and illuminated with the continuously tunable laser (CTL) (see fig. 3.7 for an illustration of the experimental setup). The structures consist of 20 µm long, 300 nm wide and 160 nm high nanobeam waveguides terminated with either shallow-etched gratings or circular gratings. The distance to the substrate is 1.15 µm, and thus optimized for the performance of the shallow-etched gratings. Some structures are terminated by a shallow-etched grating at one end, and a circular grating at the other end.

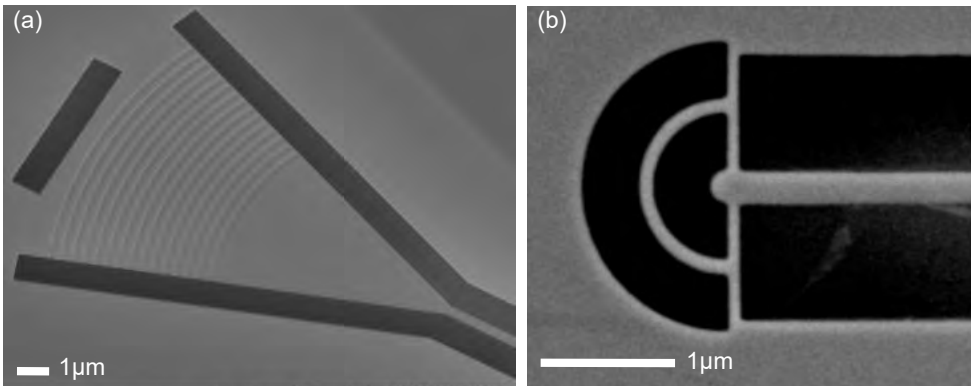

Figure 4.14: Images of the gratings: (a): SEM image of a shallow-etched grating. The square hole after the grating section ensures a full undercut of the gratings. **(b):** SEM image of the circular gratings. Note the difference in scales.

Figure 4.14(a) and (b) show SEM images of the shallow-etched and circular gratings respectively.

4.4.1 Transmission measurements

Transmission measurements are performed by focusing the CTL at one of the gratings and collecting the light from the other grating. The collected light is coupled into a fiber and sent onto a spectrometer (see fig. 3.7). The analysis of the data is done by comparing the intensity of the transmitted light to the specular reflection of the surface of the sample. The intensity is calculated as the area under the peak

evaluated from the central pixel ±5 pixels minus the background as illustrated in fig. 4.15.

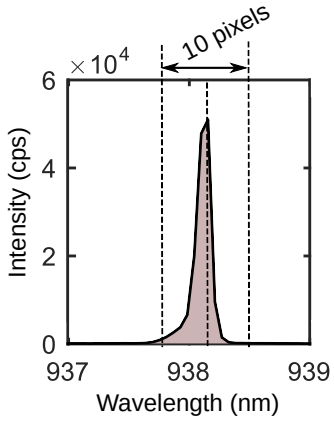

Figure 4.15: Spectrum: An example of a reference spectrum. The intensity is calculated as the area under the peak. The background is calculated as the intensity averaged over 10 pixels, 25 pixels away from the center of the peak.

The fraction of reflected power from a surface is given by the Fresnel equations.

$$R_{ref} = \left(\frac{n_1 \cos(\theta_1) - n_2 \cos(\theta_2)}{n_1 \cos(\theta_1) + n_2 \cos(\theta_2)} \right)^2 \tag{4.7}$$

In our case we have normal incidence, i.e., $\theta_1 = \theta_2 = 0$, and we can calculate the reflected power from just the indices of the two media; $n_1 = n_{\text{air}} = 1$ and $n_2 = n_{\text{GaAs}}(\lambda, T)$ which is temperature and wavelength dependent, and thus calculated for the appropriate parameters in each analysis. The intensity of the specular reflection spectrum, $refI_{total}$ is used as a reference to which the light transmitted through the structure, I_{total} is compared, and we define the total transmission as $T_{total} = \frac{I_{total}}{refI_{total}}$. The corrected single-grating-transmission efficiency is calculated as $T_{corr} = \sqrt{T_{total} * R_{ref}}$, where R_{ref} is the specular reflection as defined in eq. (4.7), and we assume equal in-coupling and out-coupling efficiencies. We thus arrive at an estimated value of the single-grating efficiency.
The wavelength of the CTL is swept from 915 nm to 980 nm, and the structures terminated with shallow-etched gratings at both ends are compared to the structures terminated by circular gratings at both ends. The first evidence of the superiority of the shallow-etched gratings is visible when looking at the image on the CCD camera. Figure 4.16(b) shows transmission through a waveguide terminated by circular gratings in both ends, whereas fig. 4.16(c) shows the transmission through a waveguide terminated by shallow-etched gratings. In both images the excitation spot is to the left. Aside from transmitting more light than the circular gratings, the field transmitted from the shallow-etched grating is more symmetric than the field transmitted from the circular gratings and is therefore more likely to match the mode of a fiber. Simulations showing the symmetry of the fields emitted from the shallow-etched and circular gratings respectively can be found in fig. B.5 in the

appendix.

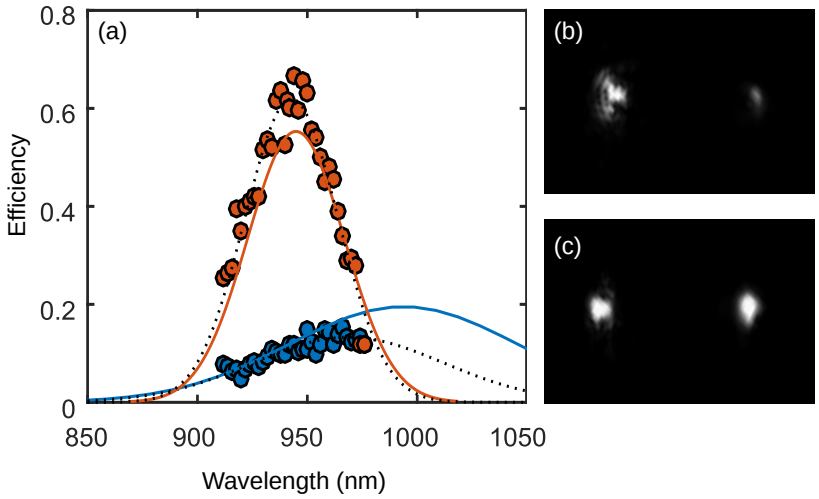

Figure 4.16: Comparing model and experiment: (a): Experimental data showing the single-grating efficiency of the shallow-etched gratings (red bullets) and the circular gratings (blue bullets) plotted together with the Gaussian fit to the simulated data (solid lines). The dotted lines are Gaussian fits to the experimental data. The measurements are done at room temperature, and the data from the simulations have been shifted accordingly (see fig. B.6). **(b):** Transmission through a structure terminated by circular gratings. The light is launched into the leftmost grating. The wavelength of the laser is 960 nm and the power on the sample is 50 nW. **(c):** Same as (b) with shallow-etched gratings rather than circular gratings.

Figure 4.16(a) clearly indicates that the shallow-etched gratings (red) outperform the circular gratings (blue). The dots show the experimentally obtained values, while the solid line is the result of the simulations described in section 4.3.2. The maximally achievable single-grating efficiency, evaluated from the Gaussian fit to the experimental data (dotted lines in fig. 4.16), of the circular gratings is 13 $\pm$ 1 %, whereas the maximally achievable single-grating efficiency, evaluated in the same way, of the shallow-etched gratings is 62 $\pm$2 %. The uncertainty stems from the 95 % confidence bounds from the Gaussian fits. Comparing the two datasets indicates that the shallow-etched gratings offer an increase of 49 p.p. in chip-to-fiber coupling efficiency compared to circular gratings.

The fit to the experimental data from the shallow-etched gratings yields a central wavelength of 943 $\pm$ 1 nm, and the central wavelength of the simulated data is 945 $\pm$ 1 nm. As the experiment is done at room temperature, the data from the simulations have been shifted to longer wavelengths in accordance with a temperature-tuning-coefficient calculated from two sets of simulated data (fig. B.6). In the case of the circular gratings, the central wavelength estimated from the experimental data is 969 $\pm$ 12 nm, where the data from the simulations suggest a central wavelength of 993 $\pm$ 3 nm. Hence the simulations of the shallow-etched gratings show better agreement with the experimental data in terms of central wavelength than

the circular gratings.
Table 4.2 gives an overview of the data obtained from the simulations as well as experiments.

	Central λ	Max. efficiency	Bandwidth
Sim. Shallow	$944.8 \pm 1\,\text{nm}$	$55.3 \pm 2\,\%$	$51.8 \pm 2\,\text{nm}$
Exp. 1	$940.2 \pm 2\,\text{nm}$	$52.9 \pm 3\,\%$	$54.4 \pm 8\,\text{nm}$
Exp. 2	$948.0 \pm 2\,\text{nm}$	$53.7 \pm 4\,\%$	$55.2 \pm 7\,\text{nm}$
Exp. 3	$942.8 \pm 1\,\text{nm}$	$61.9 \pm 3\,\%$	$50.1 \pm 3\,\text{nm}$
Exp. Average	$943.7 \pm 2\,\text{nm}$	$56.2 \pm 3\,\%$	$53.2 \pm 6\,\text{nm}$
Sim. Circular	$993.1 \pm 3\,\text{nm}$	$19.5 \pm 1\,\%$	$122.7 \pm 8\,\text{nm}$
Exp. 1	$959.1 \pm 20\,\text{nm}$	$6.0 \pm 1\,\%$	$94.2 \pm 61\,\text{nm}$
Exp. 2	$968.7 \pm 12\,\text{nm}$	$13.3 \pm 1\,\%$	$102.1 \pm 27\,\text{nm}$
Exp. Average	$963.9 \pm 16\,\text{nm}$	$9.7 \pm 1\,\%$	$98.2 \pm 44\,\text{nm}$

Table 4.2: Results: An overview of the result obtained from simulations as well as experiment. The average values from the experimental data from the shallow-etched gratings match the simulated results well, whereas the data from the circular gratings differ significantly from the simulated data.

The simulations of the shallow-etched gratings slightly underestimate the maximally achievable efficiency (55 % from simulations vs. 56.2 % averaged from three repetitions of the experiment), while the simulations of the circular gratings overestimate the performance (19 % from simulations vs. 9.7 % from experiments). The only difference in the way the analysis of the simulations is done is the tilt of the plane over which the overlap integral, eq. (4.6) is evaluated in the case of the shallow-etched gratings. If this is not perfectly normal to the emission, then the electric field projected onto the plane will be underestimated. Another possible explanation for the discrepancy between the two cases, is that the circular gratings are more sensitive to the excitation angle than the shallow-etched gratings. In these experiments the collection is aligned to the output grating, and the excitation beam is walked to the input grating. Despite the fact that we use two mirrors in order to compensate for the angle introduced in this way, there could be small deviations from perfectly vertical excitation, that may inadvertently affect the coupling efficiency to the circular gratings. In the case of the shallow-etched gratings, the optimum excitation angle is $\approx 9°$. We optimized the in-coupling using two mirrors, but found that the in-coupling to these gratings was much less sensitive to the position and angle of the incoming beam than the circular gratings. This may be the reason for the discrepancy between the deviations from the the simulated performance in the two cases.

In the previous data analysis it is assumed that the in-coupling and out-coupling efficiencies are equal. In order to separate the two, measurements on structures terminated by a shallow-etched grating at one end, and a circular grating at the other end are performed. By comparing the total transmission obtained when

coupling into a circular (shallow-etched) grating and out from a shallow-etched (circular) grating to the total transmission obtained when coupling in and out from circular gratings we get an estimate of the achievable improvement in out-coupling (in-coupling) when replacing circular- with shallow-etched gratings.
Referring to the in-coupling efficiency of the shallow-etched and circular gratings as $\mathrm{SEG_{in}}(\lambda)$ and $\mathrm{CG_{in}}(\lambda)$ respectively, and the out-coupling efficiencies as $\mathrm{SEG_{out}}(\lambda)$ and $\mathrm{CG_{out}}(\lambda)$, we can calculate the in-coupling- and out-coupling-efficiency ratio between the shallow-etched and circular gratings

$$\frac{\mathrm{SEG_{in}}(\lambda)}{\mathrm{CG_{in}}(\lambda)} = \frac{\mathrm{SEG_{in}}(\lambda)\cdot\mathrm{CG_{out}}(\lambda)}{\mathrm{CG_{in}}(\lambda)\cdot\mathrm{CG_{out}}(\lambda)},$$

$$\frac{\mathrm{SEG_{out}}(\lambda)}{\mathrm{CG_{out}}(\lambda)} = \frac{\mathrm{CG_{in}}(\lambda)\cdot\mathrm{SEG_{out}}(\lambda)}{\mathrm{CG_{in}}(\lambda)\cdot\mathrm{CG_{out}}(\lambda)}. \tag{4.8}$$

Here we have neglected propagation loss, which is reasonable as has been shown in Ref. [112].
Figures 4.17(a) and (b) show the results of the measurements where we couple in and out from shallow-etched- and circular gratings respectively, as indicated by the cartoon models above the figures.
The data is filtered using a moving-average filter that slides a window of length α along the data and computes the average value of the data points within the window. Hence the vector $\mathbf{x}$ containing the raw data points, can be filtered to yield a new vector $\mathbf{y}$ with entries

$$y(n) = \frac{1}{\alpha}\Big[x(n) + x(n-1) + ... + x(n-(\alpha-1))\Big]. \tag{4.9}$$

This is a way of smoothing noisy data, and the filtered data is shown in the figures as the dashed-dotted lines. The window size used is $\alpha = 3$. The red data points in figs. 4.17(a) and (b) correspond to $\mathrm{CG_{in}}\cdot\mathrm{SEG_{out}}$ and $\mathrm{SEG_{in}}\cdot\mathrm{CG_{out}}$ respectively. The blue data points in both figures represent $\mathrm{CG_{in}}\cdot\mathrm{CG_{out}}$.
The ratios are calculated from the filtered data and plotted in fig. 4.17(c). It shows that the shallow-etched gratings offer an advantages over the circular gratings in the whole wavelength range spanning from 914 nm to 975 nm. The advantage is most pronounced in the short wavelength range, which is expected as the central wavelength of the shallow-etched gratings (943 nm) is lower than the central wavelength of the circular gratings (968 nm). For this reason we expect that the ratio calculated here is slightly overestimated in the short wavelength range, while it is slightly underestimated in the long-wavelength range. At approximately 955 nm, the curve representing the in-coupling-ratio goes up while the curve representing the out-coupling ratio goes down. This behavior stems from the $\mathrm{CG_{in}}\cdot\mathrm{SEG_{out}}$ and $\mathrm{SEG_{in}}\cdot\mathrm{CG_{out}}$ data, where it is clear that the increase in out-coupling efficiency is more pronounced at short wavelengths whereas the increase in in-coupling efficiency

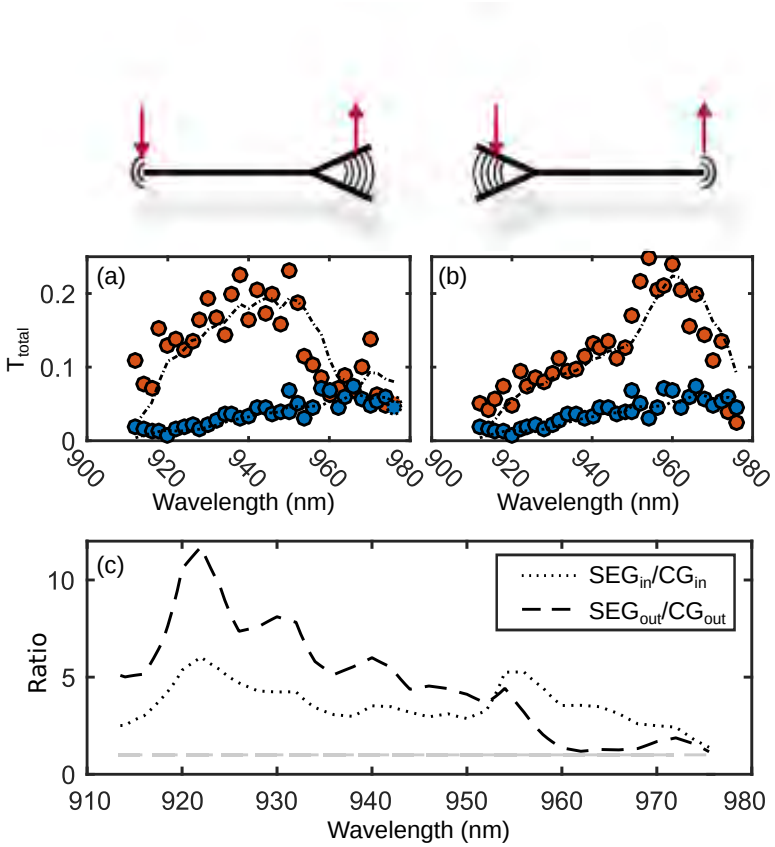

Figure 4.17: Separating in- and out-coupling: (a): Coupling in through a circular grating and collecting from a shallow-etched grating: $CG_{in} \cdot SEG_{out}$, (red data points) and coupling in and out from circular gratings: $CG_{in} \cdot CG_{out}$ (blue data points). The dotted lines are the filtered values found using the moving average method. **(b):** Coupling in through a shallow-etched grating and collecting from a circular grating: $SEG_{in} \cdot CG_{out}$, (red data points) and coupling in and out from circular gratings: $CG_{in} \cdot CG_{out}$, (blue data points). **(c):** The dashed line shows the ratio between the interpolated values of the curves in (a), and thus gives the ratio between the out-coupling efficiency of the shallow-etched gratings (SEG) and the circular gratings (CG). The dotted line is the ratio between the in-coupling efficiencies of the shallow-etched and circular gratings.

is maximized at long wavelengths.
The advantage of the shallow-etched gratings is significant, and we see an average increase in the performance of a factor of 3.8 in the in-coupling and 4.8 in the out-coupling evaluated over the whole wavelength range.
The experiments described in this section compares shallow-etched and circular gratings fabricated on the same wafer with a substrate distance that was optimized for the shallow-etched gratings. The direct comparison between the two types of gratings can thus be argued to be unfair, and the data representing $CG_{in} \cdot SEG_{out}$ and $SEG_{in} \cdot CG_{out}$ are therefore compared to simulated data representing $CG_{in} \cdot CG_{out}$, where the substrate distance in the simulation is optimized for the circular gratings.

4.4.2 Comparison with simulated circular gratings

As evidenced by the above data analysis, the central wavelength of the circular gratings is shifted to longer wavelengths compared to the target wavelength of 948 nm (at 300 K). This is because of the sub-optimum distance to the substrate. This distance was chosen as it is optimum for the shallow-etched gratings, and the circular gratings were fabricated on the same wafer in order to make the above mentioned comparative analysis.
It can be argued that the experimental comparison is not fair, as the circular gratings were sub-optimum, however, it is not practically feasible to grow a wafer with two different thicknesses of the sacrificial layer, and for this reason we cannot fabricate shallow-etched gratings and circular gratings on the same wafer, ensuring optimal designs for both. For this reason, the data analysis of the data presented in fig. 4.17(a) and (b) has been repeated using simulated data of circular gratings with the optimal substrate distance of 1.4 μm.
The ratios are calculated using the experimentally obtained data for $CG_{in} \cdot SEG_{out}$ and $SEG_{in} \cdot CG_{out}$ and the simulated data for $CG_{in} \cdot CG_{out}$. The experimental data thus still contain a contribution from the sub optimum circular gratings and the result of this analysis yields a lower bound on the achievable increase in performance. The result of the analysis is shown in fig. 4.18. As expected, the advantage of the shallow-etched gratings over the circular gratings is slightly less pronounced in the short wavelength range than suggested in fig. 4.17(c). However, we still see an average factor of 5.3 increase in the out-coupling efficiency and an average factor of 4.0 increase in the in-coupling efficiency when comparing the shallow-etched- to the circular gratings evaluated over the whole wavelength region. The average advantage calculated in this way is greater than the advantage indicated by the purely experimental data, yet the advantage is more evenly distributed over the wavelength-range in this case. This is most likely due to the fact that the central wavelength of the two data sets in this analysis overlap, whereas they were shifted with respect to each other in the purely experimental case, due to the common

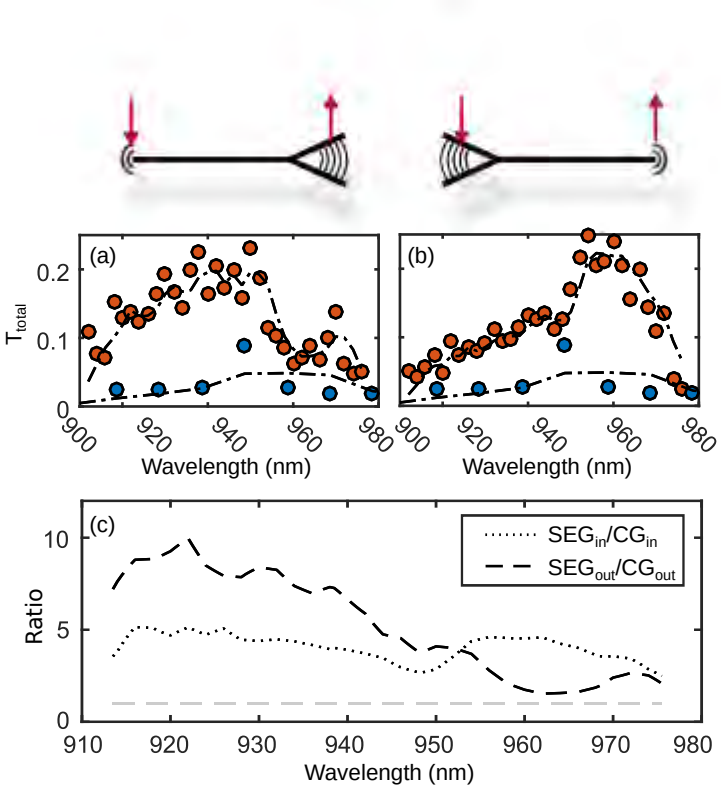

Figure 4.18: Separating in- and out-coupling: Comparing the experimentally obtained data: **(a):** $CG_{in} \cdot SEG_{out}$ and **(b):** $SEG_{in} \cdot CG_{out}$ (red points) to simulations of $CG_{in} \cdot CG_{out}$ (blue points). **(c):** The dashed line shows the ratio between the interpolated values of the curves in (a), and thus give the ratio between the out-coupling efficiency of the shallow-etched gratings (SEG) and the circular gratings (CG). The dotted line is the ratio between the in-coupling efficiencies of the shallow-etched and circular gratings extracted from (b).

substrate-thickness.

The reason for the smaller advantage in the in-coupling is most likely the mentioned issue that we misalign the excitation beam slightly in order to excite and collect at two distinct positions, and the small angle introduced in this way is tilted opposite of the angle introduced in the grating design.

We are ultimately interested in the out-coupling efficiency of the gratings as we wish to excite quantum dots in the chip, and couple the light from these out for subsequent analysis. Previous work done in this group involving a quantum dot in a photonic crystal waveguide terminated by a nanobeam waveguide with a circular grating [87] has shown that the grating throughput of the circular grating fabricated on a wafer with a substrate distance of 1.4 μm, i.e., optimum for the circular gratings, is as low as η_g =7.2%. Furthermore, it was estimated that the efficiency into a single-mode fiber was η_{fc} =31% (see table 4.3). The low coupling efficiency to the fiber is most likely due to the non-Gaussian far field of the circular gratings. This means that the total efficiency of the gratings in this work is: $\eta_g \cdot \eta_{fc} = 0.072 \cdot 0.31 = 2.2\%$. If we assume that we can replace this efficiency with

Measured efficiency	Definition
$\eta_{pr} = 100\%$	Preparation eff. of QD transition
$\beta \geq 97.5\%$	β-factor
$\eta_{qd} \geq 97.5\%$	Efficiency of SP generation
$\eta_{sw} = 71.0 \pm 0.4\%$	Throughput of slow PCW
$\eta_{fw} = 93.6 \pm 9\%$	Throughput of fast PCW
$\eta_{dw} \sim 100\%$	Throughput of DW
$\eta_{s-d} = 88 \pm 1\%$	slow-fast-dielectric transition
$\eta_g = 7.2 \pm 0.6\%$	**Grating throughput**
$\eta_l = 4.2 \pm 0.4\%$	Coupling efficiency into first lens
$\eta_{obj} = 87 \pm 2\%$	Objective throughput
$\eta_{fc} = 31 \pm 2\%$	**Collection into SM fiber**
$\eta_{sf} = 53 \pm 3\%$	Throughout of coarse filter
$\eta_{apd} = 26 \pm 2\%$	APD efficiency
$\eta_s = 3.7 \pm 0.4\%$	Setup efficiency
$\eta_{tot} = 0.15 \pm 0.02\%$	**Total efficiency**

Table 4.3: Efficiency table from [87]: A carefull analysis of the loss mechanisms was carried out by Marta Arcari et. al. They carried out an experiment involving a quantum dot situated in the slow-light section of a waveguide. They followed the photons path from emitter to APD, and evaluated the transmission efficiency off the individual components. The values that would be affected by replacing the circular gratings with shallow-etched gratings are highlighted.

the average single grating efficiency (56%) we measured, this would mean an increase in the overall efficiency of the whole setup from 0.15% to 3.8%. This assumes that all the light in the gaussian mode is coupled to the single-mode fiber with unit efficiency. This is unlikely which is why this number is an optimistic upper bound to the achievable total efficiency in a similar experiment. A more conservative way of estimating the overall gain in efficiency is to use the ratio found from figs. 4.17 and 4.18. Keeping in mind that the ratios were calculated at room temperature we estimate that the shallow-etched gratings offer a fivefold increase in efficiency in the quantum dot emission wavelength-range. This would yield a fivefold increase in the overall efficiency of the above mentioned experiment, i.e., 0.75%. This is a lower bound on the achievable increase in efficiency due to the above mentioned considerations.

4.5 Conclusion and outlook

We demonstrate how a new type of out-coupling gratings will yield a fivefold increase in the chip-to-fiber coupling efficiency, as well as a significant reduction in back-reflections into the waveguides.
We have presented a simulation-based optimization of a shallow-etched grating design. The design is inspired by a well-known design in silicon photonics, and is adopted for the typical emission wavelength of InAs quantum dots. This design is implementable with planar technologies and allows for high chip-to-fiber coupling efficiencies without putting constraints on the position of the structure on the wafer, or requiring complex fiber-based out-coupling schemes. From simulations the chip-to-fiber coupling efficiency is predicted to be $\sim 55\,\%$, while the average experimental chip-to-fiber efficiency is found to be $\sim 56\,\%$. The robustness to fabrication imperfections is evaluated from the simulations and indicates that within the achievable fabrication accuracy of $10\,\%$, the effect of the deviation from the targeted value is a shift in the grating spectrum which, due to the large bandwidth of the gratings, doesn't imply a significant decrease in efficiency. When comparing the performance of the shallow-etched gratings to the circular gratings used previously, experiments indicate an increase in chip-to-fiber efficiency of 49 p.p. at the target wavelength of 930 nm. An attempt to separate the in-from out-coupling efficiencies is presented, and yields an approximate fivefold increase in both in- and out-coupling when comparing the shallow-etched- to the circular gratings. This indicates that, despite the added complexity in the fabrication caused by an additional etching step, the achievable improvement is significant. The improvement stems mainly from the emitted field being mode-matched to a symmetric Gaussian. Aside from the increase in coupling efficiency, a major advantage of the shallow-etched gratings is the reduced back-scattering. Simulations show that the back-scattering can be reduced from $\sim 26\,\%$ to $\sim 3\,\%$ when replacing circular gratings with shallow-etched gratings. It was shown in chap. 3 that the reflections lead to unwanted Fabry-Pérot modes that are detrimental to the performance of the routing device.
It has been suggested that the improvement in coupling efficiency might be even more pronounced by apodizing the first grooves in the grating [110]. The purpose of the apodization is to shape the output beam and make it more Gaussian along the propagation direction. This is done by tailoring the so called leakage factor α defined from $P(x) = P_0 e^{-2\alpha x}$, where $P(x)$ is the power evaluated at x along the grating, P_0 is the power immediately before the grating, and x is the propagation direction. By tailoring the leakage factor such that $2\alpha(x) = \frac{G^2(x)}{1-\int_0^x G^2(t)dt}$ where $G(x)$ is a normalised Gaussian profile, the overlap with the optical fiber is improved. The x-dependence of α is achieved by varying the fill factor or etch depth along the propagation direction. According to [110], this will increase the maximum theoretical efficiency by $15\,\%$. For our gratings, this would result in a theoretical efficiency of $63\,\%$ rather than the current $55\,\%$. This approach was not

investigated further in this work, but is currently being examined by Irina Kulkova from Sparrow Quantum.
To sum up, we have demonstrated that by adding another etching step in the fabrication process of grating out-couplers we can improve the grating throughput by a factor of ~ 5. This is in itself a significant increase that can be pushed even further by introducing an apodization in the first grooves of the grating.
Recently the shallow-etched gratings have been tested on a sample containing quantum dots and the expected five-fold increase in single-photon count-rates on the APD is confirmed.

Chapter 5

Chiral quantum optics and single-photon nonlinearities

This chapter describes two experiments that illuminate the rich physics associated with the platform consisting of a single quantum dot coupled to a photonic-crystal waveguide.
The first part of the chapter presents an introduction to nanophotonics and provides the basis on which the described experiments are developed.
The first experiment described is a demonstration of how engineering of the crystal geometry leads to propagation-direction-dependent, or chiral, light-matter interaction with applications ranging from spin-readout, to quantum non-demolition measurement of single photons, and deterministic cNOT gates.
Subsequently we describe how a quantum dot strongly coupled to the propagating mode of a standard W1 waveguide will exhibit strong nonlinear behavior at the single-photon level. This means that a single-photon state interacts differently with the emitter than a two- or more-photon state, which can find applications within quantum information [113, 114]. The articles on which this chapter is based are

- I. Söllner, S. Mahmoodian, **S. L. Hansen**, L. Midolo, A. Javadi, G. Kiršanskė, T. Pregnolato, H. El.Ella, E. H. Lee, J. D. Song, S. Stobbe and P. Lodahl. "Deterministic phton-emitter coupling in chiral photonic circuits". *Nat. Nanotechnology, vol.* **10**, p. 775 (2015) [115]

- A. Javadi, I. Söllner, M. Arcari. **S. L. Hansen**, L. Midolo, S. Mahmoodian, G. Kiršanskė, T Pregnolato, E. H. Lee, J. D. Song, S. Stobbe and P. Lodahl. "Single-photon nonlinear optics with a quantum dot in a waveguide". *Nat. Communications, vol.* **6**, p. 8655 (2015) [116]

The Chiral experiment is based on a proposal developed by Immo Söllner and Sahand Mahmoodian. The analysis of the data was predominantly carried out by Immo Söllner. I contributed to the acquisition of the data included in the article, as well as discussions of the results. For the sake of cohesion, the following is a description of all the work leading up to the publication including the theoretical background, experimental procedure, data analysis, and an example of a practical application.
The nonlinearity experiment was driven forth by Alisa Javadi who acquired the final dataset and carried out the data analysis. My contribution to this work involves preliminary transmission measurements as well as continuous discussions in the process. This chapter presents an outline of the experiment, including theory, experimental procedure and application.

5.1 Theoretical background

5.1.1 Photonic nanostructures

The optical properties of quantum emitters may be modified strongly by tailoring the dielectric environment around the emitter. The number of optical modes per unit volume and frequency bandwidth available to an emitter at position $\mathbf{r_0}$ and frequency ω_0, is quantified through the local density of optical states (LDOS) [34], $\rho(\mathbf{r_0}, \omega_0, \hat{e}_d)$, where $\hat{e}_d$ is a unit vector oriented along the transition dipole moment. The LDOS is a central quantity in the local light-matter interaction as it affects the radiative decay-rate of quantum dots through

$$\gamma_{\mathrm{rad}}(\mathbf{r}, \omega, \hat{e}_d) = \frac{\pi\omega}{\hbar\epsilon}|\mathbf{p}|^2\rho(\mathbf{r}, \omega, \hat{e}_d), \tag{5.1}$$

where $|\mathbf{p}|$ is the magnitude of the transition dipole moment. Equation (5.1) assumes that the LDOS varies slowly over the linewidth of the emitter. This approximation, known as the Wigner-Weisskopf approximation, is valid in the structures examined in this thesis. Employing this approximation, the decay dynamics of the emitter may be altered by either engineering the LDOS via the local environment, or by changing magnitude of the dipole moment in order to reach the weak-confinement regime. In Ref. [34] it was shown that controlling the magnitude of the dipole moment is not straight forward and we will henceforth focus on the manipulation of the LDOS.

5.1.2 Photonic crystals

A photonic crystal is a structure where the dielectric permitivity is spatially periodic. It can be realized by etching airholes into a high-index material such as GaAs. In this work we consider a quasi-two-dimensional photonic crystal where

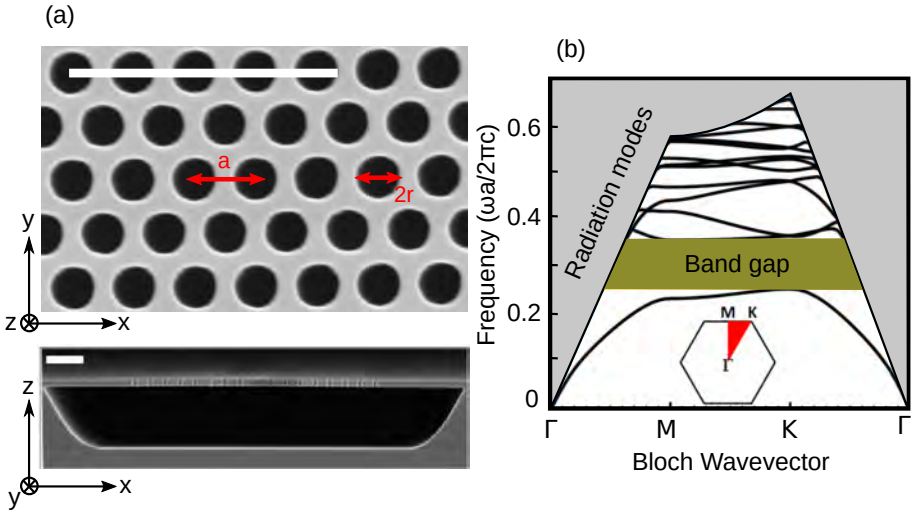

Figure 5.1: Photonic crystal: (a): Scanning electron microscope image of a photonic crystal realized by defining air holes arranged in a triangular lattice (top). The crystal is defined on a suspended membrane (bottom). The scale bar in both images is 1 µm. **(b):** Dispersion relation for wave-vectors along the high symmetry directions in the first Brillouin zone. Figures reproduced from Refs. [119] and [29].

the airholes are arranged as a triangular lattice defined on a 160 nm thick suspended membrane. The details of the fabrication process may be found in [46]. A scanning electron microscope (SEM) image of a photonic crystal is depicted in fig. 5.1(a). The periodicity of the holes leads to the formation of a photonic band gap, i.e., a range of frequencies where no optical modes are allowed to propagate, which is why a photonic crystal can be considered as the optical analogue of a semiconductor [117]. The position of the band gap is fully determined from the hole radius (r) and the lattice constant (a) at a fixed membrane thickness. The finite thickness of the membrane confines light in the slab via total internal reflection. The radiation modes above the light line defined by $\omega = k_x c$, are not confined to the membrane by total internal reflection (see fig. 5.1(b)).
Within the band gap of the photonic crystal, spontaneous emission is strongly suppressed as there are no available states into which the emitter may decay. Experiments have demonstrated inhibition factors of up to 70 in photonic crystals [118].

5.1.3 Nanophotonic waveguides

Introducing a line-defect into the photonic crystal lattice by omitting a row of air holes, opens up allowed modes within the bandgap. This is known as a W1 waveguide and is illustrated in fig. 5.2(a). Three guided modes are supported by the line-defect and are allowed to propagate within the bandgap in the dispersion diagram seen in fig. 5.2(b). The in-plane confinement is provided by Bragg-reflections, and the out-of-plane confinement is provided by total internal reflection. The slab

modes are extended into the membrane.
The waveguide-modes propagate with a group velocity given by the slope of the mode in the dispersion relation, i.e., $v_g = \partial\omega/\partial k$. In the following we only consider the fundamental mode, M0. From the dispersion of this mode, we see that close to the band edge, the group velocity goes to zero, and from theory we would expect the group index $n_g = c/v_g$ to go to infinity and exhibit a Van Hove Singularity. In experiments the unavoidable fabrication imperfections induce random scattering resulting in localized modes. Previous work suggests that group indices on the order of $n_g \sim 60$ is attainable close to the band edge in photonic crystal waveguides [120]. The low group velocity in W1 waveguide enhances the light-matter interaction through the LDOS

$$\rho_{wg}(\omega, \mathbf{r}, \hat{e}_d) = \frac{a}{\pi v_g} \frac{f(\mathbf{r})}{\epsilon(\mathbf{r}) V_{\text{eff}}} |\hat{\mathbf{e}}_k^*(\mathbf{r}) \hat{\mathbf{e}}_d|^2, \tag{5.2}$$

where ω is the frequency of the emitter, $\mathbf{r}$ is the position of the dipole, $\hat{\mathbf{e}}_d$ is a unit vector pointing in the direction of the transition dipole moment, $\mathbf{e}_k^*(\mathbf{r})$ is the orientation of the polarization of the light in the waveguide, and V_{eff} is the effective mode volume of the unit cell. The function $f(\mathbf{r})$ quantifies the spatial mismatch between the emitter and maximum of the field inside the waveguide, while the term $|\hat{\mathbf{e}}_k^*(\mathbf{r})\hat{\mathbf{e}}_d|$ quantifies the alignment of the dipole moment of the quantum dot and the polarization of the waveguide mode. The influence of the group velocity on the light-matter interaction is evident from eq. (5.2). Close to the band edge, where the group velocity goes to zero we expect a very high density of optical states, and thus an enhanced coupling between the emitter and the propagating mode of the waveguide. The degree of enhancement is quantified via the Purcell factor $F_P(\omega) = \gamma_{\text{rad}}(\omega)/\gamma_{\text{rad}}^{\text{hom}}(\omega)$, that compares the decay rate of the considered emitter to that of an identical emitter placed in a homogeneous medium [121]. A quantum dot sitting spatially and spectrally at an optimum position in the waveguide, will emit photons predominantly into the propagating mode of the waveguide. The coupling between the emitter and the waveguide mode is quantified through the β-factor, comparing the decay rate into the waveguide mode γ_{wg} to the total decay rate of the emitter including the decay rate to the waveguide mode, the decay rate to non-guided modes γ_{ng}, and the non-radiative decay rate γ_{nrad}

$$\beta = \frac{\gamma_{\text{wg}}}{\gamma_{\text{wg}} + \gamma_{\text{ng}} + \gamma_{\text{nrad}}}. \tag{5.3}$$

The remarkable feat of the photonic crystal waveguide is that it enhances the coupling to the waveguide mode, while inhibiting the coupling to non-guided and non-radiative modes, thus ensuring very high β-factors. It has been experimentally demonstrated that β-factors up to 98.4 % can be achieved for InAs quantum dots embedded in a W1 waveguide [36]. This near unity coupling efficiency between the emitter and the propagating mode constitute an ideal platform for the development of deterministic single-photon sources. Furthermore, the realization of quantum

information protocols that involve interaction between a propagating mode and an emitter, such as the chiral-interactions and single-photon nonlinearity, described in this chapter, depend upon a high β-factor.

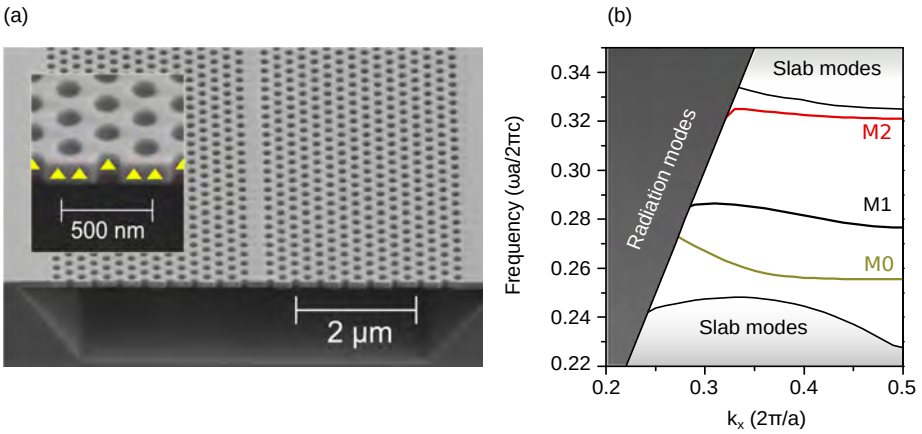

Figure 5.2: Photonic crystal waveguide: (a) Photonic crystal defined on a suspended membrane. The W1 waveguide is realized by omitting a row of holes. A single layer of self-assembled quantum dots are embedded in the center of the slab. **(b):** Dispersion relation of the W1 waveguide. Three waveguide modes are supported within the otherwise forbidden band gap of the photonic crystal. The waveguide is designed such that the slow section of the M0 mode is overlapped with the typical quantum dot emission. Reproduced from Refs. [34] and [122] respectively.

The slow-down of light in a W1 waveguide has the adverse effect of increasing the sensitivity to fabrication imperfections leading to unwanted coupling to Anderson-localized modes [123].
Another disadvantage of the slow light is that it is not readily coupled out from the in-plane propagating mode, and must therefore be translated through a so-called fast section before it can efficiently be coupled out from the chip. The fast section is realized by stretching the lattice constant by 7 % in the propagation direction. This translates the waveguide mode towards lower frequencies, and thus converts light at a certain frequency to propagate with a higher group velocity as illustrated in fig. C.1 in the appendix. For this reason, the photonic crystal waveguides are often composed of an interaction- or slow-light section, where the slow-light region is overlapped with the typical emission frequency of the quantum dots, and a fast-light section, where the light travels with a higher group velocity. Finally, the light is efficiently (88 % [84]) coupled to a suspended nanobeam waveguide, before out-coupling through a diffraction grating [63].

5.2 Chiral quantum optics

The word *chirality* comes from the Greek word $\chi\epsilon\iota\rho$ meaning hand, and denotes objects or systems that has the property that they are non-superimposable on their own mirror images. In quantum optics the word denotes a light-matter interaction that is propagation-direction-dependent [124]. Chiral quantum optics offer many new and interesting functionalities with applications in quantum information processing [125].

5.2.1 Theory

In regular W1 waveguides such as the one depicted in fig. 5.3(a), a quantum emitter will interact with photons independent of their propagation direction along the waveguide.
The mirror symmetry around $y = 0$ in a regular W1 waveguide restricts the symmetry of the propagating modes so that the **x**-projection of the electric field has odd symmetry while the **y**-projection has even symmetry [117]. From fig. 5.3(b), (c) and (d) we see that the right propagating mode is linearly polarized at the field maximum. Figures 5.3(e) and (f) show the same mode projected onto the right- and left-hand circular basis, and we see that *both* of the circular polarizations are present at the field maximum. In order to overlap the field maximum with *pure* circular polarization components, the symmetry about the $y = 0$ plane is broken leading to the eigenstates no longer being purely odd or even, but rather a linear combination of the odd and even eigenstates. If the phase difference between the odd and even eigenstates is $\pi/2$, the resulting mode will have in-plane circular polarization. A Glide Plane Waveguide (GPW) is designed by shifting the lattice on one side of the waveguide by $a/2$ and changing the hole-to-hole center width of the waveguide to $0.8a\sqrt{3}$, as depicted in fig. 5.3(g). This breaking of the up-dowm symmetry has the desired consequence of ensuring a predominantly circular polarization at the field maximum as can be seen in figs. 5.3(i),(j),(k) and (l). The left-propagating mode can be found by complex conjugating the right-propagating mode.

A quantum dot with a circularly polarized transition dipole, sitting at a position where the mode is predominantly circularly polarized, will emit into one propagation direction, while the orthogonal dipole will emit into the opposite propagation direction. This is illustrated in fig. 5.4 where the quantum dot transitions, in the presence of a magnetic field, are shown in (a), and the corresponding propagation directions are shown in (b). The directionality is quantified by calculating a directionality factor F_{dir} which is the ratio between photons emitted into the desired direction, Γ_{dir}, and the photons emitted into both propagating modes of the waveguide, $\Gamma_{\text{L}} + \Gamma_{\text{R}} = \Gamma_{\text{wg}}$. The directional β-factor, i.e., the probability that a photon from the emitter, is channelled to the correct propagation direction, can now

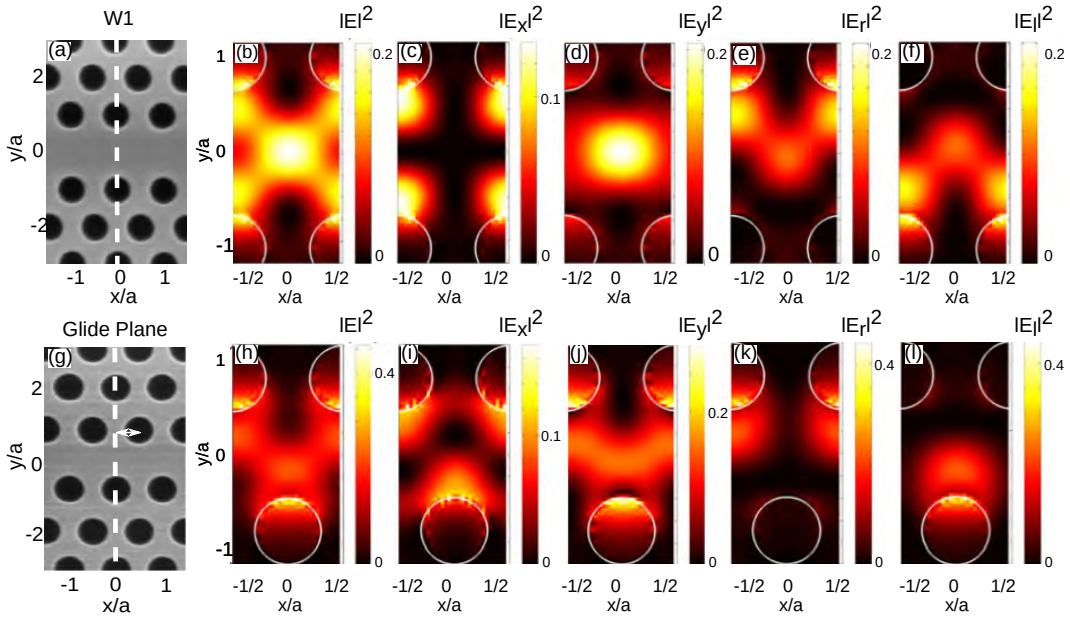

Figure 5.3: Symmetry and right-propagating-field projections: (a): SEM image of a regular W1 waveguide, which exhibits up-down symmetry about $y = 0$. **(b):** Intensity of the total electric field for a W1 waveguide, $|\mathbf{E}|^2$. **(c)** and **(d)**: The intensities of the x and y components of the electric field of the W1 waveguide respectively. **(e)** and **(f):** The intensities of the right- and left-hand circular polarized components of the field in the W1 waveguide. **(g):** SEM image of a GPW, where the up-down symmetry is broken. **(h):** Total field intensity for the GPW, $|\mathbf{E}|^2$. **(i)** and **(j):** Intensities of the x and y components of the electric field in a GPW. **(k)** and **(l):** Right- and left-hand circular polarization components of the electric field of the GPW. Reproduced from supplementary information of Ref. [115].

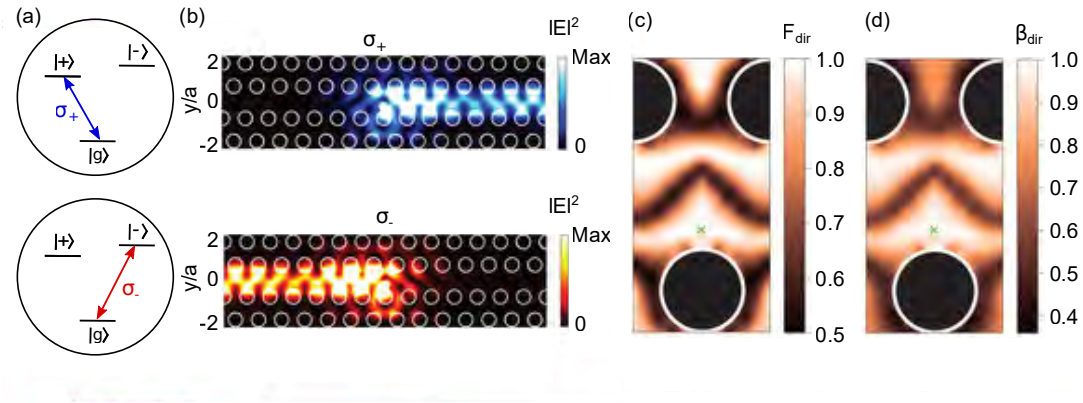

Figure 5.4: Operational principle: (a): Quantum dot level scheme in the presence of a magnetic field in the growth direction that splits the otherwise degenerate circularly polarised transitions $\sigma_{\pm}$ where the splitting is controlled by the magnetic field. **(b):** Modelled directional emission patterns of the σ_+ and σ_- transitions in the GPW. The emitter is positioned at the point where F_{dir} and β_{dir} are maximized as indicated by the crosses in **(c)** and **(d)**. The spatial dependence of the directionality factor and the directional β-factor are shown in **(c)** and **(d)** respectively. Figure from Ref. [115].

be calculate as the product of the radiative β-factor (eq. 5.3) and the directionality factor

$$\beta_{\text{dir}} = \beta F_{\text{dir}}. \tag{5.4}$$

Figures 5.4(c) and (d) show the spatial dependence of F_{dir} and β_{dir} within a unit cell of the GPW. From simulations, the maximally achievable $\beta_{\text{dir}} = 98\,\%$ which corresponds to the spatial position indicated by the green cross in fig. 5.4(c) and (d). From these figures we see that the coupling is highly directional in a large section of the unit cell which means that there is a high probability of finding a quantum dot in the desired spatial position. The spectral dependence evaluated at the cross in fig. 5.4(c) and (d) is depicted in fig. C.2 in the appendix and shows that as we approach the band edge of the structure, the β-factor increases as the slope of the mode decreases. However, the directionality drops as we approach the band edge as a result of the waveguide no longer being single-moded [126].

5.2.2 Experiment

The sample is fabricated with a GPW section, adiabatically transitioned to two standard W1 waveguide sections as indicated in the zoomed sections of fig. 5.5(b). The standard W1 waveguide serves as out-coupling waveguides and have been designed specifically to have a mode with a low group index (n_g) at the frequency of operation of the GPW ($a/\lambda = 0.26$). The W1 waveguides are terminated by suspended nanobeam waveguides with circular grating couplers. The orientation of the two grating couplers is orthogonal allowing for the subsequent separation of light collected from the two ends by means of a half-wave-plate and a polarizing

beam splitter as shown in fig. 5.5(a).
The sample is placed in an Attocube attoLIQUID1000 helium bath cryostat and cooled to 4.2 K. The excitation spot is aligned to the center of the sample containing the GPW section (green spot in fig. 5.5(b)) and two independent collection paths are aligned to the two circular couplers (red and blue spots in fig. 5.5(b)). The light from the two out-couplers is sent to two independent spectrometers and the emission lines in the collected spectra are fitted with Lorentzians. The sample is sitting in the center of a superconducting solenoid 9 Tmagnet, allowing us to change the magnetic field and observe the effect on the spectra collected from the two ends of the sample. From the spectrometers the light can be sent to two avalanche photo diodes (APD) for time-resolved measurements from which we extract the decay rates of the quantum dots, as well as the single-photon purity of the emission.

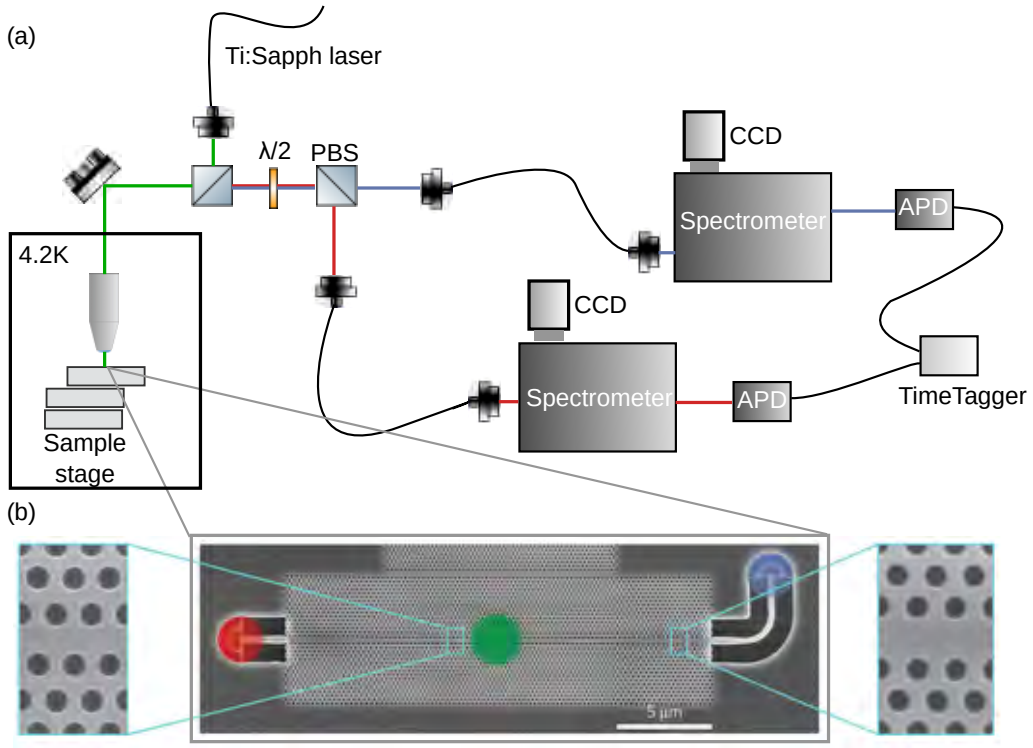

Figure 5.5: Sample and experimental setup: (a): The sample is cooled to $4.2\,\mathrm{K}$ in a liquid Helium bath cryostat. The microscope objective has an NA $= 0.65$. A 90:10 beam splitter directs $10\,\%$ of the excitation laser (green) to the sample, while transmitting $90\,\%$ of the emission from the sample. The red and blue areas and lines indicate the emission collected from the two ends of the waveguide, which can be separated using a $\lambda/2$-plate and a PBS as they have orthogonal polarizations due to the orientation of the out-couplers. The emission from the two ends is coupled into polarization maintaining (PM) fibers and sent to two independent spectrometer setups. A single wavelength component can be sent to an Avalanche Photo Diode (APD). Second order correlation measurements are performed using the signal from the two APDs sent to a time-tagger comprising a HBT-setup. **(b):** The GPW is gradually transitioned to a standard W1 waveguide and coupled to a nanobeam waveguide terminated by a circular grating. A quantum dot in the GPW section is excited above the bandgap with a Ti:Sapph laser. Part of this figure is reproduced from Ref. [115].

5.2.3 Results

In the absence of a magnetic field, the spectra recorded from the two ends of the GPW are practically identical as shown in fig. 5.6(a). When a magnetic field is applied, the quantum dot lines split into pairs corresponding to the two circular transitions indicated in fig. 5.4(a). Figure 5.6(b) shows the spectra recorded at a magnetic field of 3.1 T. The magentic field lifts the degeneracy of the σ_+ and σ_- transitions, and we see that the σ_+ transition is predominantly collected from the left out-coupler, while the σ_- transition is mainly collected from the right out-coupler. Changing the polarity of the magnetic field swaps the spectral position of the transitions, but the directionality is preserved. This illustrates that the directionality is in fact related to the helicity of the dipole transition.

The directionality factor is extracted from the spectra like the ones presented in fig. 5.6(a)-(c). The integrated count rates are calculated and used to evaluate the directionality for photons coupled out from the left (L) or right (R) of the GPW.

$$F_{\mathrm{dir},L/R} = \frac{I_{+,L/-,R}}{I_{-,L/R} + I_{+,L/R}}, \tag{5.5}$$

where $I_{-,\mathrm{R/L}}$ and $I_{+,\mathrm{R/L}}$ denote the count rates for the σ_- and σ_+ transitions into the right (R) or left (L) propagating modes. Figure 5.6(d) displays $F_{\mathrm{dir}} = (F_{\mathrm{dir},L} + F_{\mathrm{dir},R})/2$ extracted from both quantum dots A and B as a function of the applied magnetic field. The values at magnetic fields below 1 T should be ignored as the directionality cannot be extracted reliably at these fields. This is due to the resolution of the spectrum used to extract the directionality, but could also result from the fact that neutral excitons have linear dipole moments at low magnetic fields. The dipole moments only become circular at elevated field strengths. At ~ 1 T the directionality levels off and we extract $F_{\mathrm{dir}} = 90 \pm 1.3\,\%$ for quantum dot B. The lower directionality of quantum dot A is attributed to the spatial variation of the directionality within a unit cell of the GPW as depicted in fig. 5.4(c). The directional β-factor is evaluated from

$$\beta_{\mathrm{dir}} = \frac{\max[\Gamma_R, \Gamma_L]}{\gamma_{\mathrm{wg}} + \gamma_{\mathrm{ng}} + \gamma_{\mathrm{nrad}}}, \tag{5.6}$$

where Γ_R and Γ_L are the decay rates into right- and left propagating modes, $\Gamma_{\mathrm{wg}} = \Gamma_L + \Gamma_R$. The rates γ_{ng} and γ_{nrad} represent the coupling to non-guided and non-radiative modes. β_{dir} thus quantifies the fraction of emission into the waveguide mode propagating in a single direction to all other optical modes.

The single-photon purity is extracted from second order correlation measurements. When splitting the signal from either quantum dot A or B, using a beam splitter and plotting the coincidence counts as a function of time delay, we see a clear anti-bunching at 0 time delay, indicating a very high degree of single-photon purity. When cross-correlating signals from quantum dot A *and* B, we observe no

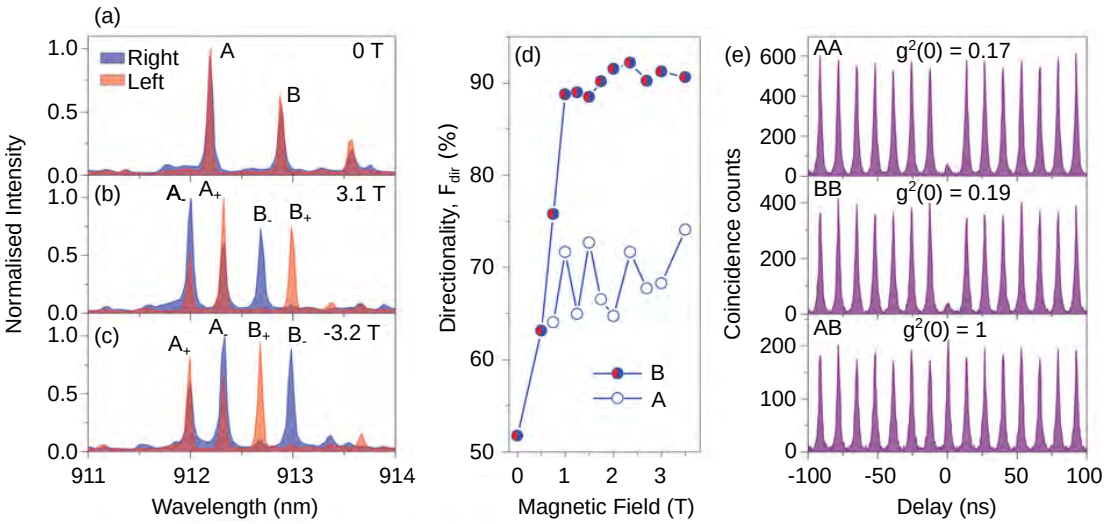

Figure 5.6: Directional emission: (a): Spectra recorded from the left (red spectrum) and right (blue spectrum) out-couplers. Two quantum dot lines, denoted A and B, are visible at $0\,\mathrm{T}$. **(b):** Applying $3.1\,\mathrm{T}$ in the growth direction breaks the degeneracy of the σ_+ and σ_- transitions, and the σ_+ transition emits predominantly into the left-propagating mode, whereas the σ_- transition emits into the opposite direction of propagation. **(c):** At $-3.2\,\mathrm{T}$ the exciton lines have swapped spectral position, but the directionality is the same as observed at positive magnetic field. **(d):** Directionality of the two quantum dots as a function of applied magnetic field. An average directionality factor $F_{\mathrm{dir}} = 90 \pm 1.3\%$ is extracted from the spectra of quantum dot B above $1\,\mathrm{T}$. **(e):** Second order correlation measurements: AA and BB denotes correlation measurements obtained when coupling emission from quantum dot A (B) out from both ends of the GPW. AB denotes the second order correlation between quantum dot A and B. Reproduced from Ref. [115].

correlation between the two signals meaning that the peaks originate from two independent quantum dots.

5.2.4 Applications

By integrating the GPW into a Mach-Zehnder interferometer (MZI) as illustrated in fig. 5.7(d), a number of intriguing applications, such as non-demolition measurements and photon sorters can be realized, as is meticulously explained in Ref. [125]. This section will focus on the implementation of a controlled not (cNOT) gate requiring a chiral interaction region, provided by the GPW, and reconfigurable beam splitters.

A cNOT gate is an essential component in quantum computing, as a cNOT gate combined with single qubit rotations constitute a universal set of gates [127]. A cNOT gate flips the target qubit depending on the state of the control qubit, and transforms the state

$$a\,|0_c0_t\rangle + b\,|0_c1_t\rangle + c\,|1_c0_t\rangle + d\,|1_c1_t\rangle \tag{5.7}$$

into the state

$$a\,|0_c0_t\rangle + b\,|0_c1_t\rangle + c\,|1_c1_t\rangle + d\,|1_c0_t\rangle \tag{5.8}$$

The applicability of the GPW for the realization of a cNOT-gate stems from the high degree of directionality as quantified by β_{dir} combined with the π phase shift imparted on the transmitted photon (for more details see Ref. [125]). In the following we assume $\beta_{\mathrm{dir}} \to 1$, and utilize the level structure of a singly charged exciton (a trion) placed in an external magnetic field, as depicted in fig. 5.7(c). The branching ratio indicated by the diagonal lines can be suppressed to 1:1000 by the presence of an external magnetic field, B_{ext}, on the order of 300 mT [128, 129]. For $B_{\mathrm{ext}} > 2\,\mathrm{T}$ the spin relaxation time starts to decrease as B_{ext}^{-5} [130] limiting the range of external magnetic fields for the suggested application. An in-plane oscillating magnetic field, $B_{\mu w}$, allows for the preparation of an arbitrary superposition of the single-spin ground states [115, 131].

A controlled not gate can be realized as follows:

The trion is initialized in the spin up state [129], and the reconfigurable beam splitter is set to 100:0. A $\pi/2$ microwave pulse prepares an equal superposition of the spin-up and spin-down state

$$|\uparrow\rangle \xrightarrow{\pi/2} \frac{1}{\sqrt{2}}(|\uparrow\rangle + |\downarrow\rangle). \tag{5.9}$$

A control photon on resonance with the σ_--transition (k_r) is sent in right to left, in either of the two control arms 1' or 2' in fig. 5.7(d),

$$\frac{1}{\sqrt{2}}(|\uparrow\rangle + |\downarrow\rangle) \xrightarrow{k_r} \frac{1}{\sqrt{2}}(|\uparrow, k_r\rangle + t_k\,|\downarrow, k_r\rangle), \tag{5.10}$$

where the transmission coefficient; $t_k = \pm 1$ depending on whether the photon passed in the interaction region (-1) or not (+1). The photon-matter state is separable, and we can thus write the state as a product of the photon state $|k_r\rangle$ and the coherent superposition of the spin ground states. Applying a second $\pi/2$ microwave pulse yields

$$\frac{1}{\sqrt{2}}(|\uparrow\rangle + t_k\,|\downarrow\rangle)\,|k_r\rangle \xrightarrow{\pi/2} \frac{1}{2}\Big((|\uparrow\rangle + |\downarrow\rangle) + t_k(|\downarrow\rangle - |\uparrow\rangle)\Big)\,|k_r\rangle \tag{5.11}$$

$$= \frac{1}{2}\Big((1 - t_k)\,|\uparrow\rangle + (1 + t_k)\,|\downarrow\rangle\Big)\,|k_r\rangle \tag{5.12}$$

Hence, if the control photon k_r is sent through arm 2', then the transmission coefficient $t_k = -1$ and the final spin state is mapped to $|\uparrow\rangle$, whereas the final spin state is $|\downarrow\rangle$ is the control photon entered arm 1'.
Now the reconfigurable beams splitters are set to 50:50, and the target photon is sent into arm 1 (left to right). Depending on the spin state of the trion in the GPW, i.e., depending on the path traversed by the control photon, the target photon entering arm 1(2) will exit through arm 4(3) or 3(4) as derived in sec. C.1, and hence the action on the target photon depends on the state of the control photon as dictated by the cNOT gate and depicted in fig. 5.7(a).

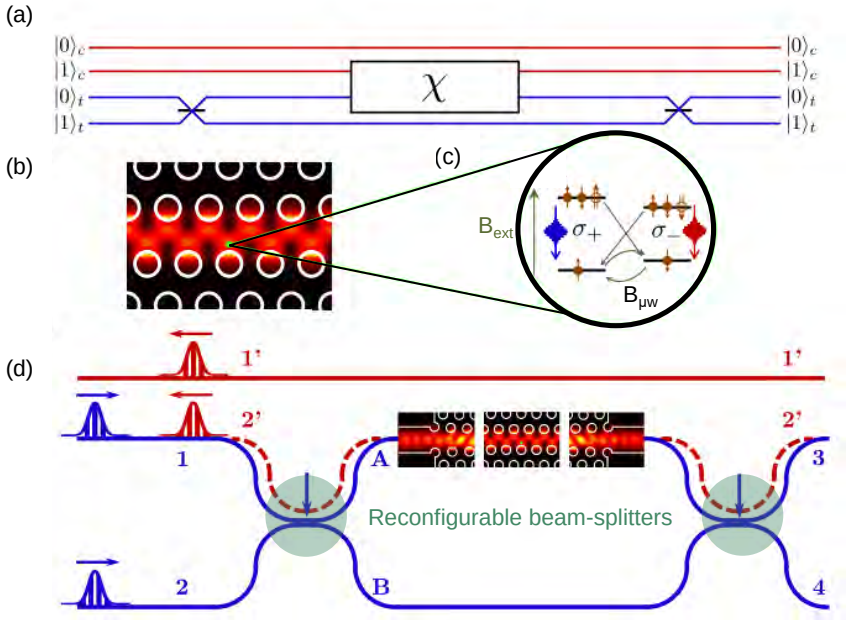

Figure 5.7: cNOT gate using a GPW: (a): Illustration of how the cNOT gate works. The interaction section χ is placed in one arm of the MZI, but can also be traversed by the control photon if this is in the state $|1\rangle_c$. In this case the target photon is swapped from $|0\rangle_t$ to $|1\rangle_t$ or the other way around. If the control photon is in the state $|0\rangle_c$, nothing happens to the target photon. **(b):** Schematic of a GPW with the emitter sitting at the point where β_{dir} is maximised. **(c):** Level structure of the trion in the presence of an external magnetic field. **(d):** Schematic of the MZI with the GPW in one of the arms. The beam splitters are reconfigurable and are to be used in the 100:0 or 50:50 mode in this application. Figure reproduced from Ref. [132]

5.2.5 Conclusion

A novel type of chiral light-matter interaction has been demonstrated using a photonic crystal waveguide with broken symmetry in the up-down direction. This type of interface is expected to find widespread applications in quantum information processing, and has been proposed for on-chip spin readout, single-photon transistor, quantum non-demolition measurements and a cNOT gate [125, 115]. The functionality of the device presented here depends on the position of the emitter in the waveguide which at present is random and relies on chance. Deterministic positioning of quantum dots [133] will boost the yield of structures applicable for the mentioned functionalities.
The principle of engineering chiral interactions can be extended to platforms beyond the one considered here, and may be implemented in suspended nanobeam waveguides (NWG) that exhibit larger areas of chiral behavior [134].

5.3 Single-photon nonlinearity

The fact that photons rarely interact with each other, makes them suited for communicating information over long distances. However, if one is to optically process the information, this requires some form of interaction between signals, and this interaction can be enabled by nonlinear optical processes [18]. A two-level emitter deterministically coupled to a one-dimensional propagating mode can mediate such an interaction, as each photon will inevitably interact with the emitter. Hence, such a system constitutes a platform for the realization of a giant nonlinearity sensitive at the single-photon level [135]. In order for the single-photon nonlinear interaction to be fully deterministic, the mode overlap between the propagating mode, and the emission profile of the emitter must be perfect, leading to a β-factor of unity. Such a system is referred to as a 1D atom.

We know that is it possible to achieve near-unity coupling between an emitter and the propagating mode of a photonic crystal waveguide (PCW) [36], making this platform highly suited for the investigation of nonlinearities at the single-photon level. Furthermore, it can be naturally incorporated in integrated photonic circuits, making this approach particularly attractive. Other approaches to explore the nonlinear response of a quantum emitter include the use of atoms [136], single molecules [137] or ions [138]. A few-photon nonlinearity in the reflection spectrum of a quantum dot strongly coupled to a cavity was demonstrated in Ref. [139].
Here we demonstrate a single-photon nonlinearity induced by a quantum dot in a PCW, by measuring the transmission spectrum of the PCW around the resonance frequency of a well-coupled quantum dot.

5.3.1 Theory

Classically, an optical nonlinearity refers to the case where a sufficiently intense light beam alters the materials refractive index, making light propagation power-dependent. The quantum analogy is when one photon and two photons interact differently with an optical system, and is an important ingredient in quantum information processing [140].

A quantum dot coupled to a PCW is a suited platform to investigate nonlinearities at the single photon level, due to the high achievable β-factor. A photon propagating in the waveguide will, with near unity probability, interact with the quantum dot.
The input state is that of a nearly single-frequency laser and is well described as a coherent state

$$|\alpha\rangle = e^{-\frac{|\alpha|^2}{2}} \sum_{n=0}^{\infty} \frac{\alpha^n}{\sqrt{n!}} |n\rangle \tag{5.13}$$

where $|\alpha|^2$ is the average photon number of the state. At low excitation powers, i.e., $|\alpha|^2 \ll 1$, the system is in the coherent scattering regime, referred to as the

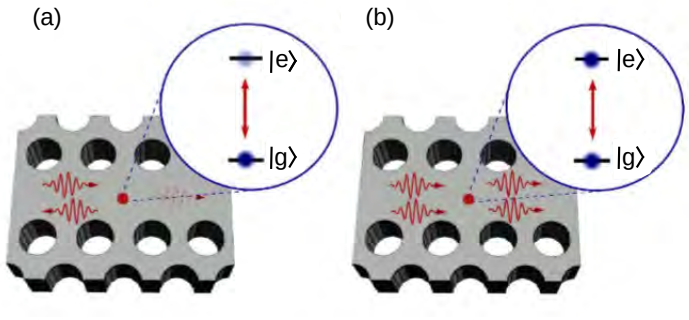

Figure 5.8: Single-photon nonlinearity: (a): Coherent scattering off the quantum dot. At low excitation-power the there will be destructive interference between the photon scattered in the forward-propagating direction and the incident photon leading to an ideally vanishing transmission probability. **(b):** The multi-photon states have a higher transmission probability leading to bunching in the second order correlation. Figure from Ref. [122].

Heitler regime [141, 142] where the scattering is dominated by elastic scattering processes. In this regime, the coherence properties of the driving field is preserved, and there is therefore a fixed phase relationship between the driving field and the field scattered off the emitter and thus a high mutual coherence [143]. A photon scattered in the forward direction will interfere destructively with photons from the driving field, and in the ideal case the transmission probability goes to zero. Higher photon-number states saturate the emitter, and are thus transmitted with a higher probability. This is illustrated in fig. 5.8. Hence, the manifestation of a nonlinearity is found in the transmission spectrum and the photon statistics of the transmitted field.

We start by investigating the transmission spectrum of the transmitted field. A meticulous investigation of the dynamic can be found in Refs. [144, 145, 146]. When the power of the driving field is low, we can assume $|\alpha|^2 \ll 1$. In this case the transmission amplitude is given by [125]

$$t = \frac{(\omega - \Omega) + i\frac{\gamma}{2}}{(\omega - \Omega) + i(\frac{\Gamma}{2} + \frac{\gamma}{2})}, \tag{5.14}$$

where ω is the frequency of the driving field, $\Omega = E_{ge}/\hbar$ is the transition frequency of the emitter, and hence the the detuning can be expressed as $\delta = \omega - \Omega$. The decay rate into loss modes is denoted γ, and the decay rate into the waveguide mode is Γ. The β-factor in terms of γ and Γ is $\beta = \frac{\Gamma}{\Gamma+\gamma}$. The transmission as a function of the detuning, in units of Γ is shown in fig. 5.9(a) for three different β-factors. From this figure it is clear that the transmission dip depends on the coupling between the emitter and the waveguide-mode. Figure 5.9(b) shows how the dip at $\delta = 0$ depends on the β-factor. So far we have only considered the case of weak driving fields and we have ignored pure dephasing. The effect of dehapsing

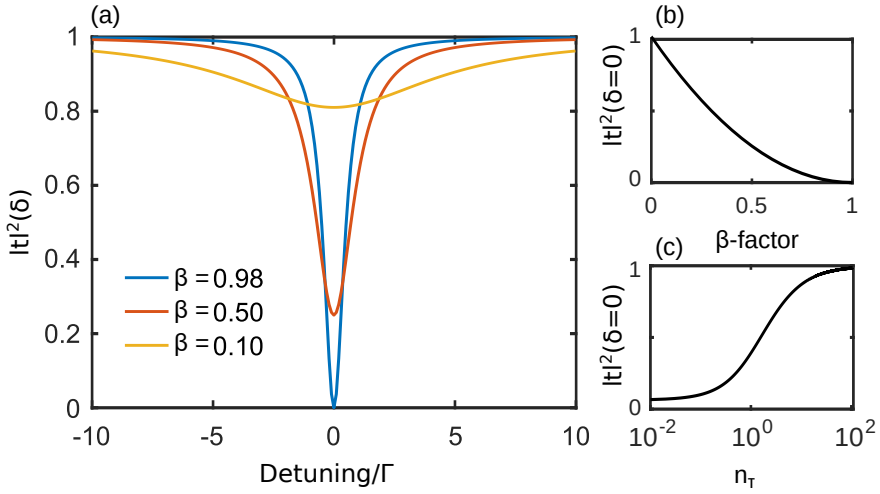

Figure 5.9: Predicted transmission: (a): The transmission probability predicted by eq. (5.14) as a function of detuning ($\delta = \omega - \Omega$), in units of Γ, for three different β-factors. **(b):** Transmission probability at $\delta = 0$ as a function of the β-factor predicted from eq. (5.14). Here we have neglected dephasing, and assumed a weak driving field ($n_\tau < n_c$). **(c):** Transmission probability as a function of the mean photon flux in the input field per lifetime of the emitter, n_τ, for $\beta = 1$ and $\gamma_0 = 0.1\Gamma$ in eq. (5.15).

and the driving field strength can be extracted from [122]

$$t(\delta = 0) = 1 - \frac{\Gamma\beta}{(\Gamma + 2\gamma_0\beta)(1 + n_\tau/n_c)} \tag{5.15}$$

where γ_0 is the pure dephasing rate, n_τ is the mean photon flux in the input field per lifetime of the emitter, and n_c is the critical photon number required to saturate the emitter. Figure 5.9(c) shows the transmission at $\delta = 0$ as a function of n_τ. The pure dephasing ($\gamma_0 = 0.1\Gamma$) manifests itself as the curves failure to go to 0 even for very low driving field strength ($n_\tau \approx 0$).
Hence, the signature of the nonlinearity, namely the transmission dip at $\delta = 0$ depends on the β-factor, the pure dephasing γ_0 and the number of photons in the input field n_τ.

Another signature of the nonlinearity is found in the photon statistics of the transmitted field [147]. The second order correlation function of the field transmitted through a 1D atom is comparable to the case of a bad-cavity as investigated in [135], if we make the substitution

$$2C = \frac{\beta}{1 - \beta}, \tag{5.16}$$

where C is the cooperativity of the cavity denoting the interaction-to-decay ratio, $C = \frac{g^2}{\kappa_c \gamma_c}$. Here g is the coupling constant, and κ_c and γ_c are the atomic and cavity damping rates respectively. The derivation and comparison is explained in greater detail in Ref. [120].
In the bad-cavity limit, assuming a weak driving field, the second order correlation

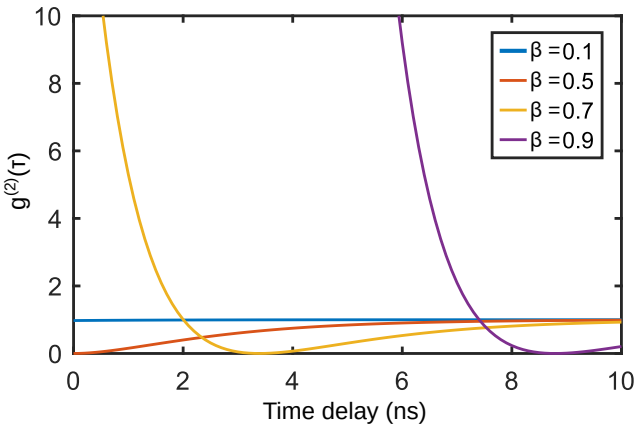

Figure 5.10: Second order correlation of the transmitted field: The second order correlation as predicted by eq. (5.18) for four different values of β. The driving field is assumed to be weak, we have neglected pure dephasing, and $\Gamma = 1$.

function is given by

$$g^{(2)}(\tau') = (1 - 4C^2 e^{-\tau'/2})^2, \tag{5.17}$$

where τ' is the dimensionless time $\tau' = \gamma_c(1 + 2C)\tau$.
Making the substitution suggested in eq. (5.16), allows us to write the second order correlation for the right going field in a 1D atom in the case of zero detuning and a low driving field

$$g^{(2)}_{1D}(\tau) = e^{-\Gamma\tau}\left(\left(\frac{\beta}{1-\beta}\right)^2 - e^{\Gamma\tau/2}\right)^2. \tag{5.18}$$

This is plotted as a function of the delay-time τ in fig. 5.10 for four different values of β. In the limit of very poor coupling between the emitter and the waveguide-mode ($\beta = 0.1$), the field is unaffected by the presence of the emitter, and we observe the expected behavior for a coherent input field. At moderate coupling ($\beta = 0.5$) we observe anti-bunching at zero time delay. This situation is not to be compared to the situation where detection of the first photon sets a time-origin when the emitter is in the ground state and cannot fluoresce. The situation investigated here is different, and thus the interpretation of anti-bunching is also different [135]. The detection of a photon in this case does not signify that the emitter has returned to the ground state, as we are looking at the superposition of the forward re-radiated field from the emitter with the weak coherent driving field. For high, but realistic values of β (> 0.7), there is a clear bunching at zero time delay, meaning that there is a high probability to detect a second photon, conditioned on the detection of a first photon at $\tau = 0$. This is a signature of a weak coherent state, where the single-photon component has been removed. The subsequent anti-bunching takes place at $\tau_a = 2\ln\left(\frac{\beta^2}{(1-\beta)^2}\right)$. Understanding of the anti-bunching can be gained by inspecting the state prepared by the first photo-detection. This was done for the case of a bad-cavity in Ref. [135], and the interpretation they offer is the following. The mean field amplitude will experience a phase change of π as the quantum state

is reduced (the reduced quantum state is prepared by the detection of the first photon), and during relaxation back to the steady state, there will be a time, when the mean field exactly cancels the driving field. At this time, τ_a, no second photon can be detected. For $\beta = 0.5 \rightarrow \tau_a = 0$ explaining the anti-bunching at zero time delay in fig. 5.10 (red curve). The full derivation as presented in Ref. [120] can be found in the appendix; section C.2 and C.3.
The effect of pure dephasing, and driving field strength has been examined in detail elsewhere [122, 119], and only a brief summary of the findings is presented here:
Dephasing has the expected effect of degrading the coherence of the system, and for a pure dephasing rate of $\gamma_0 = 2\Gamma$ the statistics of the light in the transmitted field is unaffected by the emitter, and the $g^{(2)}(\tau)$ resembles that of a coherent field [119].
The dependence on the driving field strength can be predicted from fig. 5.9(c) where we see that for large n_τ i.e., strong driving field, the transmission dip vanishes as the emitter saturates, and thus the $g^{(2)}(\tau)$ is that of the coherent input field [122].
To sum up; the nonlinearity at the single-photon level is revealed as a dip at $\delta = 0$ in the transmission spectrum and as a bunching at $\tau = 0$ in the second order correlation of the transmitted field. The observation of these features requires a large coupling strength between the emitter and the waveguide mode quantified by the β-factor, relatively low dephasing and a weak driving field; $n_\tau < n_c$.

5.3.2 Experiment

The sample used to demonstrate the single-photon nonlinearity consists of a photonic crystal waveguide with a slow-light section in the middle, indicated by the yellow waveguide section in fig. 5.11(b) and (c). In this section the slow-down factor is $n_g \approx 30$, and we can reach β-factors close to unity. The quantum dot is placed in the slow section as indicated in fig. 5.11(a). The slow light is translated to fast light ($n_g \approx 5$) in the red waveguide sections indicated in fig. 5.11(b) and (c) in order to achieve maximum out-coupling from the gratings.
The green spot in the center of the slow section indicates the presence of a re-pump laser used to stabilize and initiate the emitter before the scattering process. The red spots indicate the excitation and collection areas. The gratings are oriented at 90° in order to separate the input light from the output light by polarization-filtering.
The sample is mounted in the flow cryostat (see fig. 3.7), and cooled to 10 K. For the second-order correlation measurements, the emission is sent to a HBT-setup, like the one illustrated in fig. 5.5(a).
The light from a toptica DLPro 940 laser is launched into the structure from one of the gratings, and the transmission is collected from the other grating (red circles in fig. 5.11(b)). A Ti:Sapph laser operated at 850 nm in CW is used as a re-pump laser. The purpose of the re-pump is to initialize the system in the ground state and minimize spectral wandering, which is a broadening mechanism that stems from the fluctuating charge environment. The effect of this type of broadening is explained

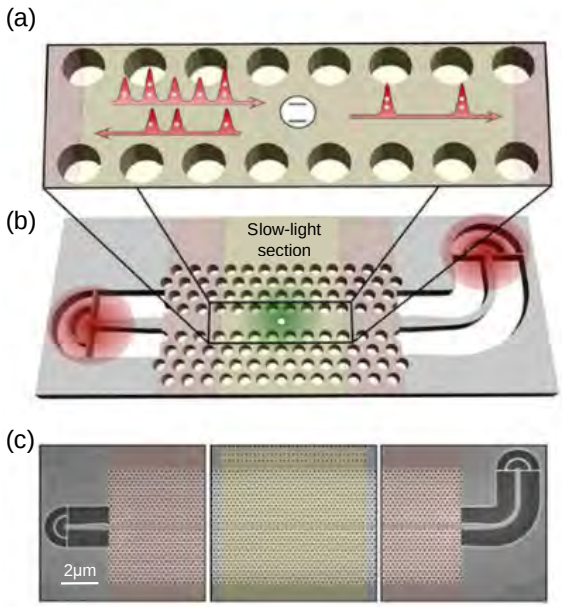

Figure 5.11: Operational principle: (a): Illustration of the operational principle, where the single-photon components of the driving field are reflected, whereas the the two- and higher-photon states are transmitted past the two level system. **(b)** Model and **(c)** SEM image of the device consisting of a slow-light section (yellow) terminated by fast-light sections (red), suspended nanobeam waveguides and circular gratings. The central green spot in (b) indicates the illumination region of the repump laser. The red areas indicate the excitation and collection spots respectively. Figure reproduced from Ref. [116]

in great detail in Ref. [122]. The intensity of the re-pump can be modulated using a chopper-wheel with adjustable rotation frequency.

5.3.3 Results

We choose a quantum dot located in the slow light section emitting at $\sim 914\,\mathrm{nm}$. The single-photon nature of the emission from the dot is verified through a second order correlation measurement performed by exctiting the dot above band, below- but close to saturation-power and sending the emission to a HBT setup, (fig. 5.5(a)). Figure 5.12(a) shows the result of the measurement under pulsed excitation.

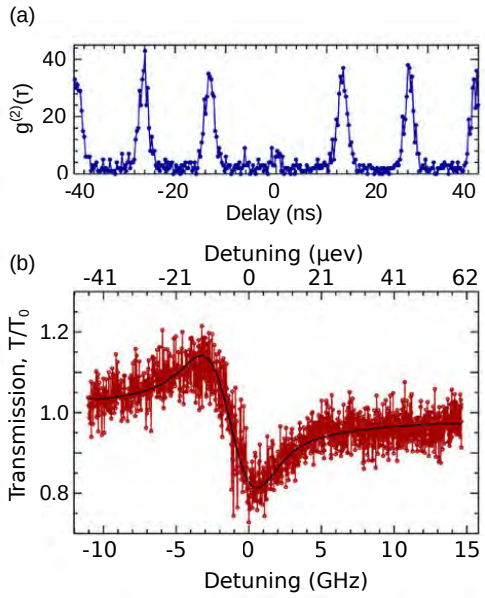

Figure 5.12: Second order correlation measurement and transmission: (a): Result of second-order correlation measurement under pulsed wetting-layer excitation. **(b):** Transmission spectrum as a function of detuning recorded by scanning the weak ($\sim 50\,\mathrm{pW}$ on the sample) DLPro laser across the quantum dot transition. Figure from Ref. [116]

The antibunching at zero time delay is a clear signature of the single-photon emission from the quantum dot. Figure 5.12(b) shows the transmission through the waveguide as a function of the detuning between the quantum dot and the weak coherent laser. Reflections from the ends of the waveguide causes weak Fabry-Pérot resonances to form, leading to a Fano resonance [148] manifested by the asymmetrical shape of the transmission dip.

Next we investigate the behavior of the transmission spectrum as a function of the excitation power quantified by n_τ. From theory we expect the transmission dip to vanish for large n_τ due to saturation of the emitter, (fig. 5.9(c)). This is verified experimentally as witnessed in figs. 5.13(a) and (b) where fig. 5.13(a) corresponds

to the situation where $n_\tau \sim 0.11$ and fig. 5.13(b) shows the behavior at $n_\tau \sim 1.3$. Figure 5.13(c) shows the transmission at zero detuning as a function of n_τ. The results are fitted with a model, based on eq. (5.15) that also includes the effect of blinking (Appendix C in Ref. [122]) and where the spectral wandering is included in the model as a random jittering in the transition frequency of the quantum dot, $\omega_{sw} = \omega + \delta_0$, where ω is the quantum dot transition frequency and δ_0 is a random variable with a Gaussian probability distribution. From fig. 5.13(c) we recognise three different regimes. At low input-power, the value of the transmission dip is independent of the power. This regime is called the coherent scattering regime as the mutual coherence of the driving field and the field scattered off the emitter is preserved. At intermediate input-power, the transmission dip depends on the input power and the transmitted field now contain a contribution from the incoherent scattering, and this regime is therefore referred to as the incoherent scattering regime. At high input power, the emitter saturates and the transmission shows no dependence on the detuning. These results indicate that the transmission dip depends on the input power as suggested by theory, and we thus conclude that the transmission dip stems from the nonlinear interaction between the coherent driving field and the field scattered off the emitter.
From the fit, a critical average number of photons of $n_c = 0.81$ is extracted, meaning that the nonlinearity is in fact operating at the single-photon level.

Additionally, the power dependence of the photon statistics is experimentally investigated. From theory we expect to see a bunching at zero time-delay as depicted in fig. 5.10. The bunching in the second order correlation being a signature of a weak coherent field with the single-photon component removed. The experiments are performed at $n_\tau \sim 0.11$ and $n_\tau \sim 1.3$ depicted in figs. 5.13(d) and (e) respectively. As expected, the data show a bunching behavior at zero time delay. Moreover, this behavior is power-dependent, as the bunching is less pronounced for the larger n_τ (fig. 5.13(e)). Figure 5.13(f) shows the peak value at zero time-delay as a function of n_τ, and shows that the nonlinearity signature is diminished for large values of n_τ leaving a constant $g^{(2)}(\tau) \approx 1$ corresponding to the Poissonian statistics expected for a coherent field.
The degree of bunching is limited by the driving field, the β-factor of the system, the dephasing and spectral wandering of the emitter.

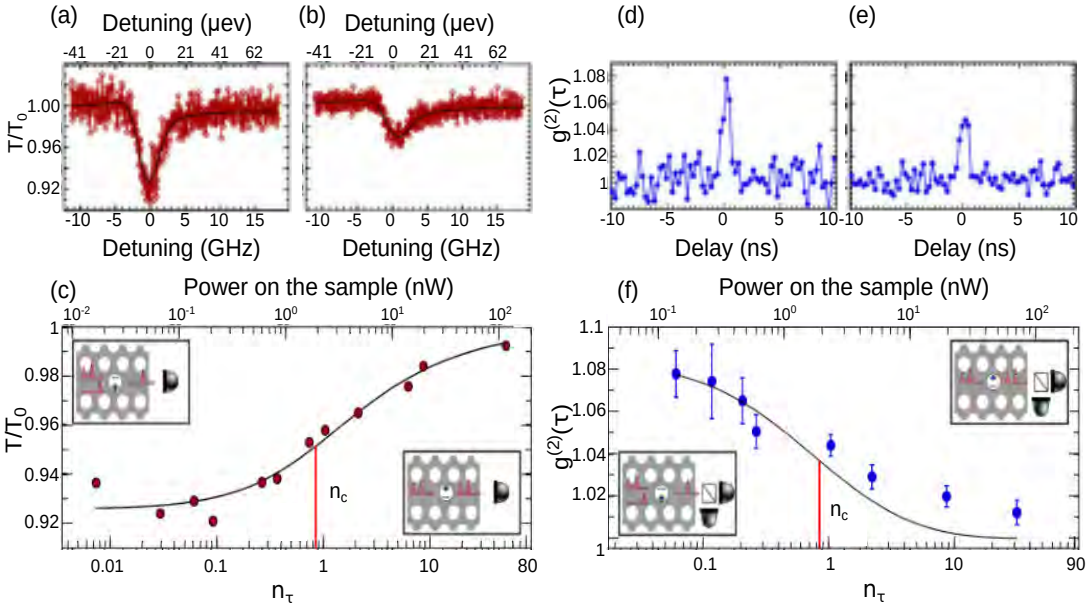

Figure 5.13: Single-photon nonlinearity: (a): Transmission as a function of detuning at $n_\tau = 0.11$, and **(b)** $n_\tau = 1.3$. **(c):** Power dependence of the transmission dip. The critical photon flux is indicated by the red line. **(d):** and **(e):** Second order correlation histograms of the transmitted field for $n_\tau = 0.11$ and $n_\tau = 1.3$ respectively. **(f):** Power dependence of the bunching at $g^{(2)}(0)$. The critical photon flux is indicated by the red line. The black lines are fits to the data, that takes into a account spectral wandering and blinking (see eq. (5.26) in Ref. [122] where the figure is taken from).

5.3.4 Conclusion

In conclusion, we have experimentally demonstrated that a single quantum dot modulates the transmission of a waveguide and alters the photon statistics of the transmitted field. We observe a maximum of 30 % contrast in the transmission dip (see fig. 5.12(b)), and an 8 % bunching at zero time-delay (see fig. 5.13(d)) indicating that the interaction with the quantum dot generates correlated multi-photon states in the transmitted field.

The factors that influence the performance of the device are the β-factor, pumping power, dephasing and spectral wandering. The data presented here was modelled (see Ref. [122] and supplementary information in Ref. [116]) and yields a β-factor of 85 %, broadening by spectral wandering of $\sigma/\Gamma = 3.6$, blinking probability of $\alpha = 0.43$, and a pure dephasing rate describing the broadening of the zero-phonon line of $\gamma_0/\Gamma = 0.79$. The decay rate of the emitter is measured to be $\Gamma = 2.5\,\mathrm{ns}^{-1}$. More recent experiments by Henri Thyrrestrup, Gabija Kiršanskė, Hanna le Jeannic and Alisa Javadi, with a gated sample show a significant increase in the contrast of the transmission dip. They report a transmission dip of approximately 60 %. This improvement is attributed to the fact that the applied electric field stabilizes the electrostatic environment reducing the temporal fluctuations leading to spectral wandering.

The experiment described in this section has paved the way towards realizing fully deterministic nonlinearities at the single-photon level in a solid-state platform. This allows for the development of on-chip single-photon switches [149], transistors [113] and photon-sorters [114, 150].

Chapter 6

Conclusion and outlook

In this thesis we have presented an experimental demonstration of a photon router in a photonic circuit with integrated single-photon sources. The integration of single-photon emitters and optical routers constitutes a fundamental step towards developing scalable quantum photonic devices for quantum information processing. In the device presented in this work, the photons emitted by single self-assembled quantum dots can be routed actively into one of two outputs. The $V_\pi L$ of the device is as small as 0.1 V cm which is a significant reduction in the footprint compared to the cm-long electro-optic modulators known from literature [103]. The sub-microsecond response time of the device makes this platform feasible for the implementation of protocols where two photons interact with an emitter at different times, but still within the coherence time of the emitter.

From modelling we found that the performance of the device was adversely affected by the cavity modes formed by the out-coupling gratings used for chip-to-fiber coupling. For this reason we set out to develop an alternative out-coupler with reduced back-scattering and with the added advantage of a much higher chip-to-fiber coupling efficiency. We adopted the shallow-etched grating design from silicon photonics and optimized it for a working wavelength of 930 nm. From simulations and experiments we found that this type of grating offers a five-fold increase in chip-to-fiber coupling efficiency while significantly reducing the reflections back into the waveguide.

Finally, two experiments are presented that underline the rich physics associated with quantum dots in photonic crystal waveguides. Firstly, a demonstration of how engineered nanostructures can lead to propagation-direction-dependent light-matter interactions known as chiral interactions. The presented platform offers a high degree of directionality, and this light-matter interface is expected to find applications within quantum information processing. Secondly, we present an ex-

perimental demonstration of a single-photon nonlinearity realized in a photonic crystal waveguide. The presented experimental data exhibits a transmission modulation of $\sim 30\,\%$, which has recently been pushed further by introducing gates on the sample to stabilize the charge environment. The single-photon nonlinearity finds numerous applications in quantum information processing [149, 113, 114, 150]. The diversity of the work presented in this thesis is a testament to the versatility of the field of quantum nanophotonics as well as the material platform used in this work. The work presented here is based on the expertise developed in the community over the last years, and while writing up this thesis the work continues in the lab. The work on single-photon routing is continued by Leonardo Midolo and Camille Papon, and they strive to reduce the $V_\pi L$ even further in a mechanically actuated system. The out-couplers have been experimentally verified to offer a five-fold increase in count-rates in single-photon experiments, and are now implemented on many new samples.

Bibliography

[1] T. S. Kuhn, *Black-body Theory and the Quantum Discontinuity.* University of Chicago Press, 1987.

[2] A. Einstein, "Concerning an heuristic point of view toward the emission and transformation of light," *Americal Journal of Physics*, vol. 33, p. 367, 1965.

[3] N. Bohr, "On the constitution of atoms and molecules," *Philosophical Magazine*, vol. 26, no. 151, p. 476, 1913.

[4] L. de Broglie, *Matter and Light: The new Physics.* W. W. Norton and Company INC, 70 Fifth Avenue, New York, 1939.

[5] W. Heisenberg, "Quantum-theoretical re-interpretation of kinematic and mechanical relations," *Z. Phys*, vol. 33, p. 879, 1925.

[6] E. Schrödinger, "Quantisierung als eigenwertproblem," *Annalen der physik*, vol. 385, no. 13, p. 437, 1926.

[7] A. Einstein, B. Podolsky, and N. Rosen, "Can quantum-mechanical description of physical reality be considered complete?," *Phys. Rev.*, vol. 47, p. 777, 1935.

[8] N. Bohr, "Can quantum-mechanical description of physical reality be considered complete?," *Phys. Rev.*, vol. 48, p. 696, 1935.

[9] W. Shockley *Bell System Technical journal*, vol. 28, no. 3, p. 335, 1949.

[10] G. E. Moore, "Cramming more components onto integrated circuits," *Electronics*, vol. 38, no. 8, p. 114, 1965.

[11] P. Shor, "Algorithms for quantum computation: discrete logarithms and factoring," *2013 IEEE 54th Annual Symposium on Foundations of Computer Science*, vol. 00, p. 124, 1994.

[12] L. K. Grover, "From schrödinger's equation to the quantum search algorithm," *Pramana*, vol. 56, no. 2, p. 333, 2001.

[13] C. H. Bennett and G. Brassard, "Quantum cryptography: Public key distribution and coin tossing," *Theoretical Computer Science*, vol. 560, Part 1, p. 7, 2014. Theoretical Aspects of Quantum Cryptography – celebrating 30 years of {BB84}.

[14] V. Giovannetti, S. Lloyd, and L. Maccone, "Advances in quantum metrology," *Nat. Photon.*, vol. 5, p. 222, 2011.

[15] H. Lee, P. Kok, and J. P. Dowling, "A quantum rosetta stone for interferometry," *Journal of Modern Optics*, vol. 49, no. 14/15, p. 2325, 2002.

[16] R. P. Feynman, "Simulating physics with computers," *International Journal of Theoretical Physics*, vol. 21, no. 6, p. 467, 1982.

[17] P. Kok, W. J. Munro, K. Nemoto, T. C. Ralph, J. P. Dowling, and G. J. Milburn, "Linear optical quantum computing with photonic qubits," *Rev. Mod. Phys.*, vol. 79, p. 135, 2007.

[18] D. E. Chang, V. Vuletic, and M. Lukin, "Quantum nonlinear optics - photon by photon," *Nat Photon*, vol. 8, p. 685, 2014.

[19] R. Hanson, L. P. Kouwenhoven, J. R. Petta, S. Tarucha, and L. M. K. Vandersypen, "Spins in few-electron quantum dots," *Rev. Mod. Phys.*, vol. 79, p. 1217, 2007.

[20] H. J. Kimble, "The quantum internet," *Nature*, vol. 453, p. 1023, 2008.

[21] M. H. Devoret and R. J. Schoelkopf, "Superconducting circuits for quantum information: An outlook," *Science*, vol. 339, p. 1169, 2013.

[22] S. M. Albrecht, A. P. Higginbotham, M. Madsen, F. Kuemmeth, T. S. Jespersen, J. Nygård, P. Krogstrup, and C. M. Marcus, "Exponential protection of zero modes in majorana islands," *Nature*, vol. 531, p. 206, 2016.

[23] S. Debnath, N. M. Linke, C. Figgatt, K. A. Landsman, K. Wright, and C. Monroe, "Demonstration of a small programmable quantum computer with atomic qubits," *Nature*, vol. 536, p. 63, 2016.

[24] S. Kocsis, G. Y. Xiang, T. C. Ralph, and G. J. Pryde, "Heralded noiseless amplification of a photon polarization qubit," *Nat Phys*, vol. 9, p. 23, 2013.

[25] M. Fox, *Optical Properties of Solids*. Oxford University press, 2010.

[26] J. A. Venables, *Introduction to Surface and Thin Film Processes*. Cambridge University press, 2000.

[27] D. M. Bruls, P. M. Koenraad, H. W. M. Salemink, J. H. Wolter, M. Hopkinson, and M. S. Skolnick, "Stacked low-growth-rate inas quantum dots studied at the atomic level by cross-sectional scanning tunneling microscopy," *Applied Physics Letters*, vol. 82, no. 21, p. 3758, 2003.

[28] S. Ruvimov, P. Werner, K. Scheerschmidt, U. Gösele, J. Heydenreich, U. Richter, N. N. Ledentsov, M. Grundmann, D. Bimberg, V. M. Ustinov, A. Y. Egorov, P. S. Kop'ev, and Z. I. Alferov, "Structural characterization of (in,ga)as quantum dots in a GaAs matrix," *Phys. Rev. B*, vol. 51, p. 14766, 1995.

[29] G. Kiršanskė, *Electrical control of excitons in semiconductor nanostructures*. PhD thesis, University of Copenhagen, Jan. 2016.

[30] H. Ibach and H. Lüth, *Solid-State Physics*. Springer-Verlag Berlin Heidelberg, 1995.

[31] A. N. Vamivakas and M. Atatüre, "Photons and (artificial) atoms: an overview of optical spectroscopy techniques on quantum dots," *Contemporary physics*, vol. 51, no. 1, p. 17, 2009.

[32] M. Bayer, G. Ortner, O. Stern, A. Kuther, A. A. Gorbunov, A. Forchel, P. Hawrylak, S. Fafard, K. Hinzer, T. L. Reinecke, S. N. Walck, J. P. Reithmaier, F. Klopf, and F. Schäfer, "Fine structure of neutral and charged excitons in self-assembled In(Ga)As/(Al)GaAs quantum dots," *Phys. Rev. B*, vol. 65, p. 195315, 2002.

[33] P. Tighineanu, *Electric and Magnetic Interaction between Quantum Dots and Light*. PhD thesis, University of Copenhagen, Feb. 2015.

[34] P. Lodahl, S. Mahmoodian, and S. Stobbe, "Interfacing single photons and single quantum dots with photonic nanostructures," *Rev. of Modern Physics*, vol. 87, no. 2, p. 347, 2015.

[35] B. Urbaszek, X. Marie, T. Amand, O. Krebs, P. Voisin, P. Maletinsky, A. Högele, and A. Imamoğlu, "Nuclear spin physics in quantum dots: An optical investigation," *Rev. Mod. Phys.*, vol. 85, p. 79, 2013.

[36] M. Arcari, I. Söllner, A. Javadi, S. Lindskov Hansen, S. Mahmoodian, J. Liu, H. Thyrrestrup, E. H. Lee, J. D. Song, S. Stobbe, and P. Lodahl, "Near-unity coupling efficiency of a quantum emitter to a photonic crystal waveguide," *Phys. Rev. Lett.*, vol. 113, p. 093603, 2014.

[37] A. V. Kuhlmann, J. H. Prechtel, J. Houel, A. Ludwig, D. Reuter, A. D. Wieck, and R. J. Warburton, "Transform-limited single photons from a single quantum dot," *Nat. Comm.*, vol. 6, p. 8204, 2015.

[38] G. Kiršanskė, H. Thyrrestrup, R. S. Daveau, C. L. Dreeßen, T. Pregnolato, L. Midolo, P. Tighineanu, S. Stobbe, R. Schott, A. Ludwig, A. D. Wieck, S. I. Park, J. D. Song, A. V. Kuhlmann, I. Söllner, M. C. Löbl, R. J. Warburton, and P. Lodahl, "Indistinguishable and efficient single photons from a quantum dot in a planar nanobeam waveguide," *arXiv:1701.08131v1*.

[39] D. Huber, M. Reindl, Y. Huo, H. Huang, J. S. Wildmann, O. G. Schmidt, A. Rastelli, and R. Trotta, "Highly indistinguishable and strongly entangled photons from symmetric GaAs quantum dots," *Nat Comm*, vol. 8, p. 15506, 2017.

[40] J.-W. Pan, Z.-B. Chen, C.-Y. Lu, H. Weinfurter, A. Zeilinger, and M. Żukowski, "Multiphoton entanglement and interferometry," *Rev. Mod. Phys.*, vol. 84, p. 777, 2012.

[41] P. Tighineanu, C. L. Dreeßen, C. Flindt, P. Lodahl, and A. S. Sørensen, "Phonon decoherence of quantum dots in photonic structures: Broadening of the zero-phonon line and the role of dimensionality," *arXiv:1702.04812v1.*

[42] A. Kiraz, M. Atatüre, and A. Imamoğlu, "Quantum-dot single-photon sources: Prospects for applications in linear optics quantum-information processing," *Phys. Rev. A*, vol. 69, p. 032305, 2004.

[43] A. D. Ferguson, A. Kuver, J. M. Heaton, Y. Zhou, C. M. Snowden, and S. Iezekiel, "Low-loss, single-mode GaAs/AlGaAs waveguides with large core thickness," *IEE Proceedings - Optoelectronics*, vol. 153, no. 2, p. 51, 2006.

[44] K. D. Jöns, U. Rengstl, M. Oster, F. Hargart, M. Heldmaier, S. Bounouar, S. M. Ulrich, M. Jetter, and P. Michler, "Monolithic on-chip integration of semiconductor waveguides, beamsplitters and single-photon sources," *Journal of Physics D: Applied Physics*, vol. 48, no. 8, p. 085101, 2015.

[45] K. Prindal-Nielsen, "Light matter interaction in nanobeam waveguides- numerical simulations and optimizations," Master's thesis, University of Copenhagen, June 2017.

[46] L. Midolo, T. Pregnolato, G. Kiršanskė, and S. Stobbe, "Soft-mask fabrication of gallium arsenide nanomembranes for integrated quantum photonics," *Nanotechnology*, vol. 26, no. 48, p. 484002, 2015.

[47] J. B. Spring, B. J. Metcalf, P. C. Humphreys, W. S. Kolthammer, X.-M. Jin, M. Barbieri, A. Datta, N. Thomas-Peter, N. K. Langford, D. Kundys, J. C. Gates, B. J. Smith, P. G. R. Smith, and I. A. Walmsley, "Boson sampling on a photonic chip," *Science*, vol. 339, no. 6121, p. 798, 2013.

[48] H. Wang, Y. He, Y.-H. Li, Z.-E. Su, B. Li, H.-L. Huang, X. Ding, M.-C. Chen, C. Liu, J. Qin, J.-P. Li, Y.-M. He, C. Schneider, M. Kamp, C.-Z. Peng, S. Höfling, C.-Y. Lu, and J.-W. Pan, "High-efficiency multiphoton boson sampling," *Nat Photon*, vol. 11, p. 361, 2017.

[49] N. Prtljaga, C. Bentham, J. O'Hara, B. Royall, E. Clarke, L. R. Wilson, M. S. Skolnick, and A. M. Fox, "On-chip interference of single photons from an embedded quantum dot and an external laser," *Applied Physics Letters*, vol. 108, no. 25, p. 251101, 2016.

[50] U. Rengstl, M. Schwartz, T. Herzog, F. Hargart, M. Paul, S. L. Portalupi, M. Jetter, and P. Michler, "On-chip beamsplitter operation on single photons from quasi-resonantly excited quantum dots embedded in GaAs rib waveguides," *Applied Physics Letters*, vol. 107, no. 2, p. 021101, 2015.

[51] N. Sherwood-Droz, H. Wang, L. Chen, B. G. Lee, A. Biberman, K. Bergman, and M. Lipson, "Optical 4×4 hitless silicon router for optical networks-on-chip (noc)," *Opt. Express*, vol. 16, no. 20, p. 15915, 2008.

[52] T. J. Seok, N. Quack, S. Han, R. S. Muller, and M. C. Wu, "Large-scale broadband digital silicon photonic switches with vertical adiabatic couplers," *Optica*, vol. 3, no. 1, p. 64, 2016.

[53] S. Han, T. J. Seok, N. Quack, B.-W. Yoo, and M. C. Wu, "Large-scale silicon photonic switches with movable directional couplers," *Optica*, vol. 2, no. 4, p. 370, 2015.

[54] F. Flamini, L. Magrini, A. S. Rab, N. Spagnolo, V. D'Ambrosio, P. Mataloni, F. Sciarrino, T. Zandrini, A. Crespi, R. Ramponi, and R. Osellame, "Thermally reconfigurable quantum photonic circuits at telecom wavelength by femtosecond laser micromachining," *Light Sci. Appl.*, vol. 4, no. 4, p. e354, 2015.

[55] C. Bentham, I. E. Itskevich, R. J. Coles, B. Royall, E. Clarke, J. O'Hara, N. Prtljaga, A. M. Fox, M. S. Skolnick, and L. R. Wilson, "On-chip electrically controlled routing of photons from a single quantum dot," *Applied Physics Letters*, vol. 106, no. 22, p. 221101, 2015.

[56] P. Lodahl, "Quantum-dot based photonic quantum networks," *arXiv:1707.02094v1*.

[57] G. Ghosh, "Temperature dispersion of refractive indices in semiconductors," *Journal of Applied Physics*, vol. 79, no. 12, p. 9388, 1996.

[58] M. R. Watts, J. Sun, C. DeRose, D. C. Trotter, R. W. Young, and G. N. Nielson, "Adiabatic thermo-optic mach-zehnder switch," *Opt. Lett.*, vol. 38, no. 5, p. 733, 2013.

[59] J. Carolan, C. Harrold, C. Sparrow, E. Martín-López, N. J. Russell, J. W. Silverstone, P. J. Shadbolt, N. Matsuda, M. Oguma, M. Itoh, G. D. Marshall, M. G. Thompson, J. C. F. Matthews, T. Hashimoto, J. L. O'Brien, and A. Laing, "Universal linear optics," *Science*, vol. 349, p. 711, 2015.

[60] T. Chu, H. Yamada, S. Ishida, and Y. Arakawa, "Compact 1 × n thermo-optic switches based on silicon photonic wire waveguides," *Opt. Express*, vol. 13, no. 25, p. 10109, 2005.

[61] M. W. Pruessner, T. H. Stievater, M. S. Ferraro, and W. S. Rabinovich, "Thermo-optic tuning and switching in soi waveguide fabry-perot microcavities," *Opt. Express*, vol. 15, no. 12, p. 7557, 2007.

[62] M. A. Dundar, F. Bordas, T. J. Eijkemans, N. Chauvin, A. Y. Silov, R. Notzel, F. Karouta, A. Fiore, and R. W. Van der Heijden, "Lithographic and optical tuning of InGaAsP membrane photonic crystal nanocavities with embedded inas quantum dots," *Journal of Nanophotonics*, vol. 3, no. 1, p. 031765, 2009.

[63] A. Faraon, I. Fushman, D. Englund, N. Stoltz, P. Petroff, and J. Vučković, "Dipole induced transparency in waveguide coupled photonic crystal cavities," *Opt. Express*, vol. 16, no. 16, p. 12154, 2008.

[64] J. W. Silverstone, D. Bonneau, K. Ohira, N. Suzuki, H. Yoshida, N. Iizuka, M. Ezaki, C. M. Natarajan, M. G. Tanner, R. H. Hadfield, V. Zwiller, G. D. Marshall, J. G. Rarity, J. L. O'Brien, and M. G. Thompson, "On-chip quantum interference between silicon photon-pair sources," *Nature Photonics*, vol. 8, no. 2.

[65] J. S. Blakemore, "Semiconducting and other major properties of gallium arsenide," *Journal of Applied Physics*, vol. 53, no. 10, p. R123, 1982.

[66] B. R. Bennett, R. A. Soref, and J. A. D. Alamo, "Carrier-induced change in refractive index of InP, GaAs and InGaAsP," *IEEE Journal of Quantum Electronics*, vol. 26, no. 1, p. 113, 1990.

[67] J. G. Mendoza-Alvarez, F. D. Nunes, and N. B. Patel, "Refractive index dependence on free carriers for GaAs," *Journal of Applied Physics*, vol. 51, no. 8, p. 4365, 1980.

[68] T. A. Ibrahim, W. Cao, Y. Kim, J. Li, J. Goldhar, P. T. Ho, and C. H. Lee, "All-optical switching in a laterally coupled microring resonator by carrier injection," *IEEE Photonics Technology Letters*, vol. 15, no. 1, p. 36, 2003.

[69] I. Fushman, E. Waks, D. Englund, N. Stoltz, P. Petroff, and J. Vučković, "Ultrafast nonlinear optical tuning of photonic crystal cavities," *Applied Physics Letters*, vol. 90, no. 9, p. 091118, 2007.

[70] L. Midolo, *Electromechanical Tuning of Photonic Crystal Cavities*. PhD thesis, Eindhoven University of Technology, May 2013.

[71] L. Midolo, A. Schliesser, and A. Fiore, "Nano-opto-electro-mechanical systems," *In preparaion*, 2017.

[72] C. P. Dietrich, A. Fiore, M. G. Thompson, M. Kamp, and S. Höfling, "GaAs integrated quantum photonics: Towards compact and multi-functional quantum photonic integrated circuits," *Laser & Photonics Reviews*, vol. 10, no. 6, p. 870, 2016.

[73] J. Shin, Y.-C. Chang, and N. Dagli, "0.3V drive voltage GaAs/AlGaAs substrate removed mach–zehnder intensity modulators," *Applied Physics Letters*, vol. 92, no. 20, p. 201103, 2008.

[74] T. H. Stievater, D. Park, W. S. Rabinovich, M. W. Pruessner, S. Kanakaraju, C. J. K. Richardson, and J. B. Khurgin, "Enhanced electro-optic phase shifts in suspended waveguides," *Opt. Express*, vol. 18, no. 2, p. 885, 2010.

[75] W. Franz, "Einfluß eines elektrischen feldes auf eine optische absorptionskante," *Z. Naturforschung*, no. 13a, p. 484, 1958.

[76] L. Keldysh, "The effect of a strong electric field on the optical properties of insulating crystals," *Soviet Physics JETP*, vol. 34, no. 5, p. 788, 1958.

[77] E. Rosencher and V. Borge, *Optoelectronics*. Cambridge University press, 2002.

[78] D. A. B. Miller, D. S. Chemla, T. C. Damen, A. C. Gossard, W. Wiegmann, T. H. Wood, and C. A. Burrus, "Electric field dependence of optical absorption near the band gap of quantum-well structures," *Phys. Rev. B*, vol. 32, p. 1043, 1985.

[79] A. Högele, S. Seidl, M. Kroner, K. Karrai, R. J. Warburton, B. D. Gerardot, and P. M. Petroff, "Voltage-controlled optics of a quantum dot," *Phys. Rev. Lett.*, vol. 93, p. 217401, 2004.

[80] J. Houel, A. V. Kuhlmann, L. Greuter, F. Xue, M. Poggio, B. D. Gerardot, P. A. Dalgarno, A. Badolato, P. M. Petroff, A. Ludwig, D. Reuter, A. D. Wieck, and R. J. Warburton, "Probing single-charge fluctuations at a GaAs/AlAs interface using laser spectroscopy on a nearby InGaAs quantum dot," *Phys. Rev. Lett.*, vol. 108, p. 107401, 2012.

[81] R. J. Warburton, "Single spins in self-assembled quantum dots," *Nat Mater*, vol. 12, p. 483, 2013.

[82] N. Somaschi, V. Giesz, L. De Santis, J. C. Loredo, M. P. Almeida, G. Hornecker, S. L. Portalupi, T. Grange, C. Antón, J. Demory, C. Gómez, I. Sagnes, N. D. Lanzillotti-Kimura, A. Lemaítre, A. Auffeves, A. G. White, L. Lanco, and P. Senellart, "Near-optimal single-photon sources in the solid state," *Nat. Photonics*, vol. 10, no. 5, p. 340, 2016.

[83] X. Ding, Y. He, Z.-C. Duan, N. Gregersen, M.-C. Chen, S. Unsleber, S. Maier, C. Schneider, M. Kamp, S. Höfling, C.-Y. Lu, and J.-W. Pan, "On-demand single photons with high extraction efficiency and near-unity indistinguishability from a resonantly driven quantum dot in a micropillar," *Phys. Rev. Lett.*, vol. 116, p. 020401, 2016.

[84] R. S. Daveau, *Efficient fiber-coupled single-photon sources based on quantum dots*. PhD thesis, University of Copenhagen, Nov. 2016.

[85] R. S. Daveau, K. C. Balram, T. Pregnolato, J. Liu, E. H. Lee, J. D. Song, V. Verma, R. Mirin, S. W. Nam, L. Midolo, S. Stobbe, K. Srinivasan, and P. Lodahl, "Efficient fiber-coupled single-photon source based on quantum dots in a photonic-crystal waveguide," *Optica*, vol. 4, no. 2, p. 178, 2017.

[86] T. G. Tiecke, K. P. Nayak, J. D. Thompson, T. Peyronel, N. P. de Leon, V. Vuletić, and M. D. Lukin, "Efficient fiber-optical interface for nanophotonic devices," *Optica*, vol. 2, no. 2, p. 70, 2015.

[87] M. Arcari, L. Midolo, M. Matthiae, T. Pregnolato, T. Pregnolato, G. Kiršanskė, S. Mahmoodian, E. H. Lee, J. D. Song, S. Stobbe, and P. Lodahl, "Efficiency and coherence of a photonic-crystal waveguide single-photon source," *arXiv:1701.08131v1*.

[88] D. Taillaert, F. V. Laere, M. Ayre, W. Bogaerts, D. V. Thourhout, P. Bienstman, and R. Baets, "Grating couplers for coupling between optical fibers and nanophotonic waveguides," *Japanese Journal of Applied Physics*, vol. 45, no. 8R, p. 6071, 2006.

[89] L. Midolo, S. L. Hansen, W. Zhang, C. Papon, R. Schott, A. Ludwig, A. D. Wieck, P. Lodahl, and S. Stobbe, "Electro-optic routing of photons from single quantum dots in photonic integrated circuits," *arXiv:1707.06522v1*.

[90] R. Syms and J. Cozens, *Optical Guided Waves and Devices*. McGraw-Hill, 1992.

[91] A. J. Bennett, R. B. Patel, J. Skiba-Szymanska, C. A. Nicoll, I. Farrer, D. A. Ritchie, and A. J. Shields, "Giant stark effect in the emission of single semiconductor quantum dots," *Applied Physics Letters*, vol. 97, no. 3, p. 031104, 2010.

[92] Y. A. Vlasov, M. O'Boyle, H. F. Hamann, and S. J. McNab, "Active control of slow light on a chip with photonic crystal waveguides," *Nature*, vol. 438, no. 7064.

[93] L. Soldano and E. Pennings, "Optical multi-mode interference devices based on self-imaging: Principles and applications," *Journal of Lightwave Technology*, vol. 13, no. 4, p. 615, 1995.

[94] G. R. Simpson, "A generalized n-port cascade connection," in *1981 IEEE MTT-S International Microwave Symposium Digest*, p. 507, 1981.

[95] H. C. Casey, D. D. Sell, and K. W. Wecht, "Concentration dependence of the absorption coefficient for n- and p-type GaAs between 1.3 and 1.6 ev," *Journal of Applied Physics*, vol. 46, no. 1, p. 250, 1975.

[96] G. E. Stillman, C. M. Wolfe, C. O. Bozler, and J. A. Rossi, "Electroabsorption in GaAs and its application to waveguide detectors and modulators," *Applied Physics Letters*, vol. 28, no. 9, p. 544, 1976.

[97] K. Tharmalingam, "Optical absorption in the presence of a uniform field," *Phys. Rev.*, vol. 130, p. 2204, 1963.

[98] J. Callaway, "Optical absorption in an electric field," *Phys. Rev.*, vol. 134, p. A998, 1964.

[99] D. Press, K. De Greve, P. L. McMahon, T. D. Ladd, B. Friess, C. Schneider, M. Kamp, S. Höfling, A. Forchel, and Y. Yamamoto, "Ultrafast optical spin echo in a single quantum dot," *Nature Photonics*, vol. 4, no. 6.

[100] K. De Greve, P. L. McMahon, D. Press, T. D. Ladd, D. Bisping, C. Schneider, M. Kamp, L. Worschech, S. Höfling, A. Forchel, and Y. Yamamoto, "Ultrafast coherent control and suppressed nuclear feedback of a single quantum dot hole qubit," *Nat Phys*, vol. 7, p. 872, 2011.

[101] J. H. Prechtel, A. V. Kuhlmann, J. Houel, A. Ludwig, S. R. Valentin, A. D. Wieck, and R. J. Warburton, "Decoupling a hole spin qubit from the nuclear spins," *Nat Mater*, vol. 15, p. 981, 2016.

[102] H. Wang, Z.-C. Duan, Y.-H. Li, S. Chen, J.-P. Li, Y.-M. He, M.-C. Chen, Y. He, X. Ding, C.-Z. Peng, C. Schneider, M. Kamp, S. Höfling, C.-Y. Lu, and J.-W. Pan, "Near-transform-limited single photons from an efficient solid-state quantum emitter," *Phys. Rev. Lett.*, vol. 116, p. 213601, 2016.

[103] J. Wang, A. Santamato, P. Jiang, D. Bonneau, E. Engin, J. W. Silverstone, M. Lermer, J. Beetz, M. Kamp, S. Höfling, M. G. Tanner, C. M. Natarajan, R. H. Hadfield, S. N. Dorenbos, V. Zwiller, J. L. O'Brien, and M. G. Thompson, "Gallium arsenide (GaAs) quantum photonic waveguide circuits," *Optics Communications*, vol. 327, p. 49, 2014. Special Issue on Nonlinear Quantum Photonics.

[104] R. H. Hadfield, "Single-photon detectors for optical quantum information applications," *Nat. Photon.*, vol. 3, p. 696, 2009.

[105] D. Vermeulen and W. Bogaerts, "Off-chip coupling," in *Handbook of Silicon Photonics* (L. Vivien and L. Pavesi, eds.), ch. 3, p. 97, Taylor and Francis, 2013.

[106] X. Chen and H. K. Tsang, "Polarization-independent grating couplers for silicon-on-insulator nanophotonic waveguides," *Opt. Lett.*, vol. 36, no. 6, p. 796, 2011.

[107] F. V. Laere, T. Claes, J. Schrauwen, S. Scheerlinck, W. Bogaerts, D. Taillaert, L. O'Faolain, D. V. Thourhout, and R. Baets, "Compact focusing grating couplers for silicon-on-insulator integrated circuits," *IEEE Photonics Technology Letters*, vol. 19, no. 23, p. 1919, 2007.

[108] W. K. Burns and G. B. Hocker, "End fire coupling between optical fibers and diffused channel waveguides," *Appl. Opt.*, vol. 16, no. 8, p. 2048, 1977.

[109] J. Yang, J.-P. Hugonin, and P. Lalanne, "Near-to-far field transformations for radiative and guided waves," *ACS Photonics*, vol. 3, no. 3, p. 395, 2016.

[110] X. Chen, C. Li, C. K. Y. Fung, S. M. G. Lo, and H. K. Tsang, "Apodized waveguide grating couplers for efficient coupling to optical fibers," *IEEE Photonics Technology Letters*, vol. 22, no. 15, p. 1156, 2010.

[111] D. Taillaert, P. Bienstman, and R. Baets, "Compact efficient broadband grating coupler for silicon-on-insulator waveguides," *Opt. Lett.*, vol. 29, no. 23, p. 2749, 2004.

[112] S. Christensen, "Characterization of quantum photonic circiuts," Master's thesis, University of Copenhagen, Jan. 2017.

[113] D. E. Chang, A. S. Sørensen, E. A. Demler, and M. D. Lukin, "A single-photon transistor using nanoscale surface plasmons," *Nat. Phys.*, vol. 3, p. 807, 2007.

[114] D. Witthaut, M. D. Lukin, and A. S. Sørensen, "Photon sorters and qnd detectors using single photon emitters," *EPL (Europhysics Letters)*, vol. 97, no. 5, p. 50007, 2012.

[115] I. Söllner, S. Mahmoodian, S. L. Hansen, M. Midolo, A. Javadi, G. Kiršanskė, T. Pregnolato, E. H. El-Ella, H. Lee, J. D. Song, S. Stobbe, and P. Lodahl, "Deterministic photon–emitter coupling in chiral photonic circuits," *Nat. Nanotechnology*, vol. 10, p. 775, 2015.

[116] A. Javadi, I. Söllner, M. Arcari, S. L. Hansen, L. Midolo, S. Mahmoodian, G. Kiršanskė, T. Pregnolato, E. H. Lee, J. D. Song, S. Stobbe, and P. Lodahl, "Single-photon non-linear optics with a quantum dot in a waveguide," *Nat. Communications*, vol. 6, p. 8655, 2015.

[117] J. D. Joannopoulos, S. G. Johnson, J. N. Winn, and R. D. Meade, *Photonic crystals: Molding the flow of light.* Princeton University Press, Princeton University Press, 2008.

[118] Q. Wang, S. Stobbe, and P. Lodahl, "Mapping the local density of optical states of a photonic crystal with single quantum dots," *Phys. Rev. Lett.*, vol. 107, p. 167404, 2011.

[119] M. Arcari, *Efficiency and Coherence of Quantum-Dot Single-Photon Sources*. PhD thesis, University of Copenhagen, Sept. 2015.

[120] S. L. Hansen, "Decay dynamics of quantum dots coupled to a photonic crystal waveguide," Master's thesis, University of Copenhagen, Sept. 2013.

[121] E. M. Purcell, *Spontaneous Emission Probabilities at Radio Frequencies*, p. 839. Boston, MA: Springer US, 1995.

[122] A. Javadi, *Quantum electrodynamics with 1D artificial atoms: from Purcell enhancement to single-photon nonlinearities*. PhD thesis, University of Copenhagen, Feb. 2015.

[123] Z. V. Vardeny and A. Nahata, "Slow light: Anderson localization of slow light," *Nat Photon*, vol. 2, p. 75, 2008.

[124] P. Lodahl, S. Mahmoodian, S. Stobbe, A. Rauschenbeutel, P. Schneeweiss, J. Volz, H. Pichler, and P. Zoller, "Chiral quantum optics," *Nature*, vol. 541, p. 473, 2017.

[125] I. N. Söllner, *Quantum Dots in Photonic Crystal Waveguides: from efficient single photon sources to deterministic photon-photon interaction*. PhD thesis, University of Copenhagen, Apr. 2014.

[126] S. Mahmoodian, K. Prindal-Nielsen, I. Söllner, S. Stobbe, and P. Lodahl, "Engineering chiral light-matter interaction in photonic crystal waveguides with slow light," *Opt. Mater. Express*, vol. 7, no. 1, p. 43, 2017.

[127] M. A. Nielsen and I. L. Chuang, *Quantum Computation and Quantum information*. Cambridge University Press, Cambridge University Press, 2010.

[128] J. Dreiser, M. Atatüre, C. Galland, T. Müller, A. Badolato, and A. Imamoğlu, "Optical investigations of quantum dot spin dynamics as a function of external electric and magnetic fields," *Phys. Rev. B*, vol. 77, p. 075317, 2008.

[129] S. T. Y ılmaz, P. Fallahi, and A. Imamoğlu, "Quantum-dot-spin single-photon interface," *Phys. Rev. Lett.*, vol. 105, p. 033601, 2010.

[130] C.-Y. Lu, Y. Zhao, A. N. Vamivakas, C. Matthiesen, S. Fält, A. Badolato, and M. Atatüre, "Direct measurement of spin dynamics in InAs/GaAs quantum dots using time-resolved resonance fluorescence," *Phys. Rev. B*, vol. 81, p. 035332, 2010.

[131] M. Kroner, K. M. Weiss, B. Biedermann, S. Seidl, S. Manus, A. W. Holleitner, A. Badolato, P. M. Petroff, B. D. Gerardot, R. J. Warburton, and K. Karrai, "Optical detection of single-electron spin resonance in a quantum dot," *Phys. Rev. Lett.*, vol. 100, p. 156803, 2008.

[132] I. Söllner, S. Mahmoodian, A. Javadi, and P. Lodahl, "A chiral spin-photon interface for scalable on-chip quantum-information processing," *arXiv:1406.4295v1*.

[133] L. Sapienza, M. Davanço, A. Badolato, and K. Srinivasan, "Nanoscale optical positioning of single quantum dots for bright and pure single-photon emission," *Nat. Communications*, vol. 6, p. 7833, 2015.

[134] R. J. Coles, D. M. Price, J. E. Dixon, B. Royall, E. Clarke, P. Kok, M. S. Skolnick, A. M. Fox, and M. N. Makhonin, "Chirality of nanophotonic waveguide with embedded quantum emitter for unidirectional spin transfer," *Nat. Communications*, vol. 7, p. 11183, 2016.

[135] P. R. Rice and H. J. Carmichael, "Single-atom cavity-enhanced absorption. I. Photon statistics in the bad-cavity limit," *IEEE Journal of Quantum Electronics*, vol. 24, no. 7, p. 1351, 1988.

[136] M. K. Tey, Z. Chen, S. A. Aljunid, B. Chng, F. Huber, G. Maslennikov, and C. Kurtsiefer, "Strong interaction between light and a single trapped atom without the need for a cavity," *Nat Phys*, vol. 4, p. 924, 2014.

[137] S. Faez, P. Türschmann, H. R. Haakh, S. Götzinger, and V. Sandoghdar, "Coherent interaction of light and single molecules in a dielectric nanoguide," *Phys. Rev. Lett.*, vol. 113, p. 213601, 2014.

[138] G. Hétet, L. Slodička, M. Hennrich, and R. Blatt, "Single atom as a mirror of an optical cavity," *Phys. Rev. Lett.*, vol. 107, p. 133002, 2011.

[139] D. Englund, A. Faraon, I. Fushman, N. Stoltz, P. Petroff, and J. Vuckovic, "Controlling cavity reflectivity with a single quantum dot," *Nature*, vol. 450, p. 857, 2007.

[140] L.-M. Duan and H. J. Kimble, "Scalable photonic quantum computation through cavity-assisted interactions," *Phys. Rev. Lett.*, vol. 92, p. 127902, 2004.

[141] C. Matthiesen, A. N. Vamivakas, and M. Atatüre, "Subnatural linewidth single photons from a quantum dot," *Phys. Rev. Lett.*, vol. 108, p. 093602, 2012.

[142] K. Konthasinghe, J. Walker, M. Peiris, C. K. Shih, Y. Yu, M. F. Li, J. F. He, L. J. Wang, H. Q. Ni, Z. C. Niu, and A. Muller, "Coherent versus incoherent light scattering from a quantum dot," *Phys. Rev. B*, vol. 85, p. 235315, 2012.

[143] P. Michler and S. L. Portalupi, *Resonantly Excited Quantum dots: Superior Non-classical Light Sources for Quantum Information*, p. 77. Springer International Publishing AG, 2017.

[144] S. Fan, i. m. c. E. Kocabaş, and J.-T. Shen, "Input-output formalism for few-photon transport in one-dimensional nanophotonic waveguides coupled to a qubit," *Phys. Rev. A*, vol. 82, p. 063821, 2010.

[145] J.-T. Shen and S. Fan, "Coherent single photon transport in a one-dimensional waveguide coupled with superconducting quantum bits," *Phys. Rev. Lett.*, vol. 95, p. 213001, 2005.

[146] J.-T. Shen and S. Fan, "Strongly correlated two-photon transport in a one-dimensional waveguide coupled to a two-level system," *Phys. Rev. Lett.*, vol. 98, p. 153003, 2007.

[147] E. Kocabaş, Şükrü, E. Rephaeli, and S. Fan, "Resonance fluorescence in a waveguide geometry," *Phys. Rev. A*, vol. 85, p. 023817, 2012.

[148] A. Auffèves-Garnier, C. Simon, J.-M. Gérard, and J.-P. Poizat, "Giant optical nonlinearity induced by a single two-level system interacting with a cavity in the purcell regime," *Phys. Rev. A*, vol. 75, p. 053823, 2007.

[149] T. Volz, A. Winger, Martin andBadolato, K. J. Hennessy, E. L. Hu, and A. Imamoğlu, "Ultrafast all-optical switching by single photons," *Nat Photon*, vol. 6, p. 605, 2012.

[150] A. J. Bennett, J. P. Lee, D. J. P. Ellis, I. Farrer, D. A. Ritchie, and A. J. Shields, "A semiconductor photon-sorter," *Nat Nano*, vol. 11, p. 857.

[151] S. Gehrsitz, F. K. Reinhart, C. Gourgon, N. Herres, A. Vonlanthen, and H. Sigg, "The refractive index of al(x)ga(1-x)as below the band gap: Accurate determination and empirical modeling," *Journal of Applied Physics*, vol. 87, no. 11, p. 7825, 2000.

[152] C. C. Gerry and P. L. Knight, *Introductory Quantum Optics*. Cambridge University press, 2002.

[153] L. Childress, *Lecture notes for Quantum Optics 2. Taught at the Niels Bohr Institute*. 2011.

[154] H. J. Carmichael, *Statistical Methods in Quantum Optics 1: Master equations and Fokker-Planck Equations*. Springer-Verlag Berlin Heidelberg, 1999.

[155] A. A. Budini, "Quantum regression theorem for non-markovian lindblad equations," *arXiv:quant-ph/0601140v2 [physics, physics:quant-ph]*.

Appendix A

Electro-optic routing

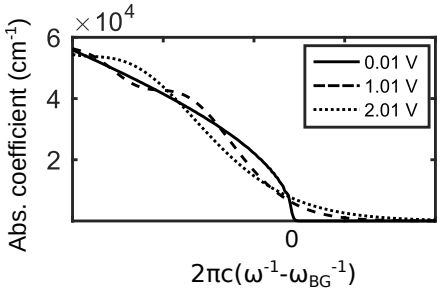

Figure A.1: The Franz-Keldysh effect: Absorption coefficient α as a function of wavelength $\left(\frac{2\pi c}{\omega}\right)$, where the band-gap energy is given by $\hbar\omega_{BG}$. At ~ 0 field, the absorption coefficient drops to zero at the band-gap, but the presence of a field extends α into the band-gap and causes oscillations above the band-gap.

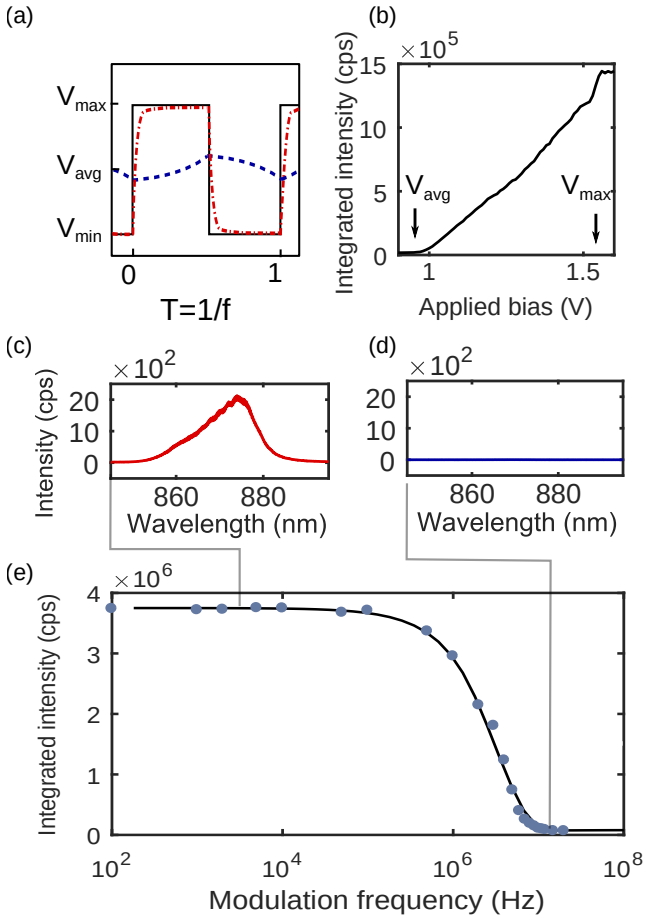

Figure A.2: Switching speed evaluated from the wetting layer emission from the waveguide. From [89]: (a): A square-wave voltage is applied to the sample, where V_{max} and V_{min} are chosen so that the wetting layer emission is maximized at V_{max} and completely turned off at $V_{avg} = \frac{V_{max} + V_{min}}{2}$. The red dash-dotted (blue dashed) line indicates the system response below (above) cut-off. **(b):** Integrated intensity from the wetting layer as a function on the applied bias.
(c): Emission spectrum recorded at $10\,\mathrm{kHz}$. **(d):** Emission spectrum recorded at $10\,\mathrm{MHz}$. **(e):** Integrated intensity of the wetting layer as a function of the modulation frequency of the square wave voltage (dots). The solid black line is the simulated response. The 3 dB cut-off is $\sim 2.8\,\mathrm{MHz}$.

Appendix B

Out-coupling

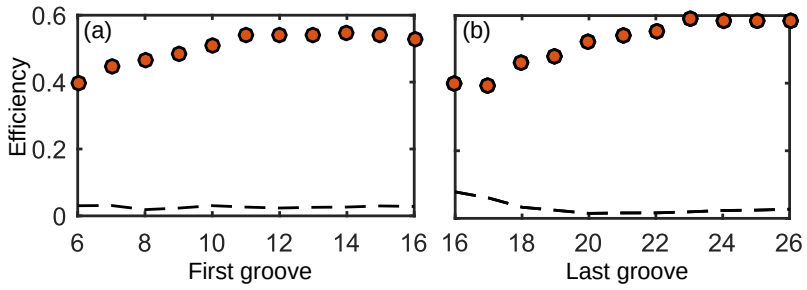

Figure B.1: Sweeping initial groove and number of grooves: (a): Effect of changing the first groove from $q = 6$ to $q = 16$ (see eqs. 4.4). At $q = 11$ the efficiency is maximized, and there's no advantage in starting the grating at $q > 11$. For all the simulations, the number of grooves is kept fixed ($N_{grooves} = 11$). **(b):** The first groove corresponds to $q = 11$, and the number of grooves is swept from 5 to 25. The reflections are minimized and the chip-to-fiber efficiency saturates when the last groove corresponds to $q = 21$, and this value is used in the fabricated samples.

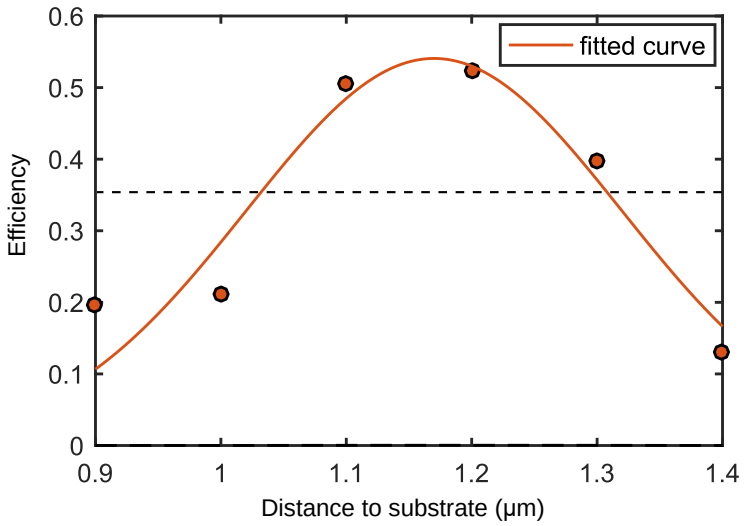

Figure B.2: Sweeping the substrate distance: For $\lambda = 930\,\mathrm{nm}$, the distance is swept from $0.9\,\mu\mathrm{m}$ to $1.4\,\mu\mathrm{m}$ in steps of $0.1\,\mu\mathrm{m}$. The Gaussian overlap is evaluated and the efficiency into a symmetric Gaussian mode is plotted versus the distance to the substrate. The fit yields an optimum distance to the substrate of $1.17\,\mu\mathrm{m}$. The wafer on which the experimentally tested gratings are defined has a targeted substrate distance of $1.15\,\mu\mathrm{m}$. The efficiency at this value is $54\,\%$. Comparing this to the value obtained from the simulations run without a substrate (dashed line: $35\,\%$) we calculate a substrate factor of $\sim \frac{54}{35} = 1.54$. This factor is used to scale the data from the simulations run without a substrate to the experimental data obtained with a substrate.

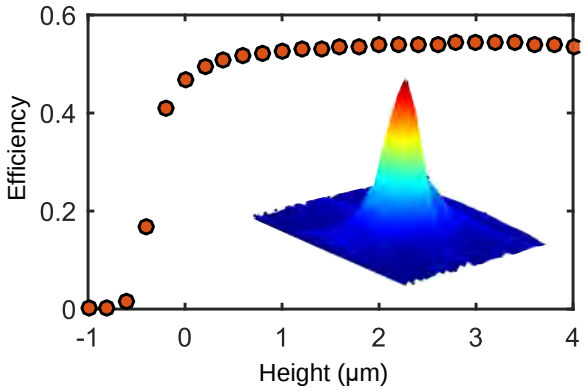

Figure B.3: Convergence test: By evaluating the Gaussian overlap at different heights above the gratings slab, we find that at $2\,\mu\mathrm{m}$ above the slab, the value has converged and we thus evaluate all the overlaps at this distance from the slab. As the plane is tilted we choose the lowest point on the plane to be $2\,\mu\mathrm{m}$ above the grating. The inset shows the absolute value of the field evaluated $2\,\mu\mathrm{m}$ above the slab.

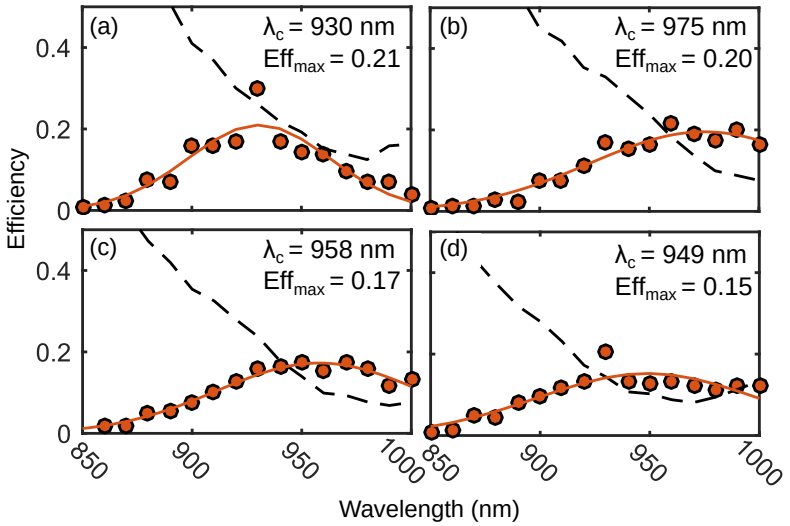

Figure B.4: Simulations of the circular gratings: (a): Using a target wavelength of $930\,\mathrm{nm}$ and a distance to the substrate of $1.40\,\mu\mathrm{m}$ **(b):** Using a target wavelength of $930\,\mathrm{nm}$ and changing the distance to the substrate to $1.15\,\mu\mathrm{m}$ **(c):** Keeping the distance to the substrate of $1.15\,\mu\mathrm{m}$ and changing the target wavelength to $890\,\mathrm{nm}$ **(d):** Using a target wavelength of $850\,\mathrm{nm}$ and a substrate distance of $1.15\,\mu\mathrm{m}$. The substrate distance of $1.15\,\mu\mathrm{m}$ must be used to optimize the performance of the shallow-etched gratings, however this causes the central wavelength of the spectrum for the circular gratings to shift to longer wavelengths as witnessed by comparing **(a)** and **(b)**. For this reason it is advisable to change the design of the circular gratings if they are to be fabricated on a wafer with a substrate distance of $1.15\,\mu\mathrm{m}$ rather than $1.40\,\mu\mathrm{m}$. From figures **(c)** and **(d)** we see that the effect of changing the target wavelength to shorter wavelengths is to shift the spectrum to shorter wavelengths, but we pay the price of lower chip-to-fiber coupling efficiency. However, it seems that the reflections back into the waveguide (black dashed lines) are smaller at the quantum dot emission wavelength than in the case of the optimum design (fig. **(a)**)

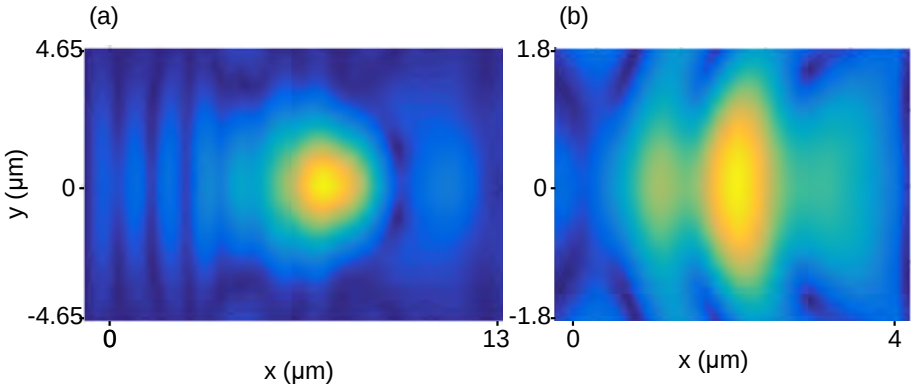

Figure B.5: Symmetry of the emitted field: (a): Absolute value of the y-component of the emitted electric field from a shallow-etched grating. The field is projected onto a plain tilted by $9°$. **(b):** Absolute value of the y-component of the emitted electric field from a circular grating. The field is projected onto a horizontal plain. Note the different scales.

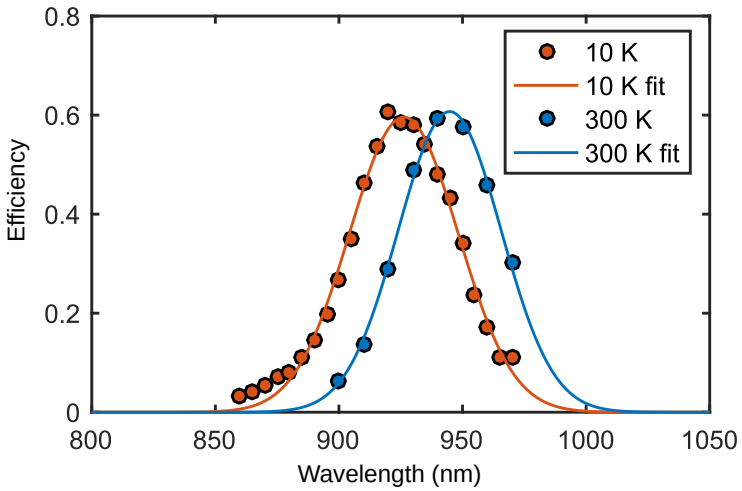

Figure B.6: Temperature shift: The effect of changing the temperature from $10\,\mathrm{K}$ to $300\,\mathrm{K}$ in the simulations. The red data-points correspond to simulations done with a temperature of $10\,\mathrm{K}$, and the red solid line is a Gaussian fit to the data. The blue points correspond to simulations done using a temperature of $300\,\mathrm{K}$, and the solid blue line as the Gaussian fit to the data. From the fits we calculate a temperature shift coefficient of $0.064\,\mathrm{nm}/\,\mathrm{K}$. This coefficient has been used to compare the simulated data done at the target temperature of $10\,\mathrm{K}$ to the experimental data collected at $300\,\mathrm{K}$. The reason for the shift is the temperature dependent refractive index calculated from [151].

Appendix C

Chiral quantum optics and nonlinearities

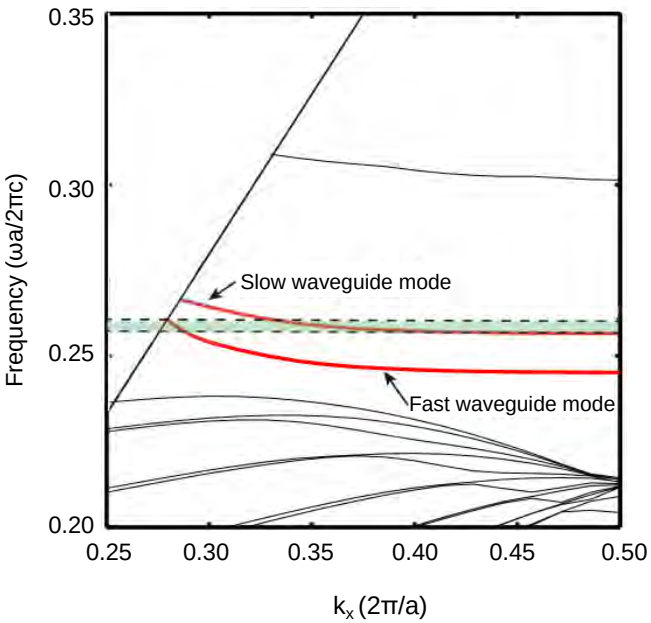

Figure C.1: Illustration of the dispersion relation for the two waveguide-sections. The green shaded area corresponds to the frequencies that can propagate in both sections.

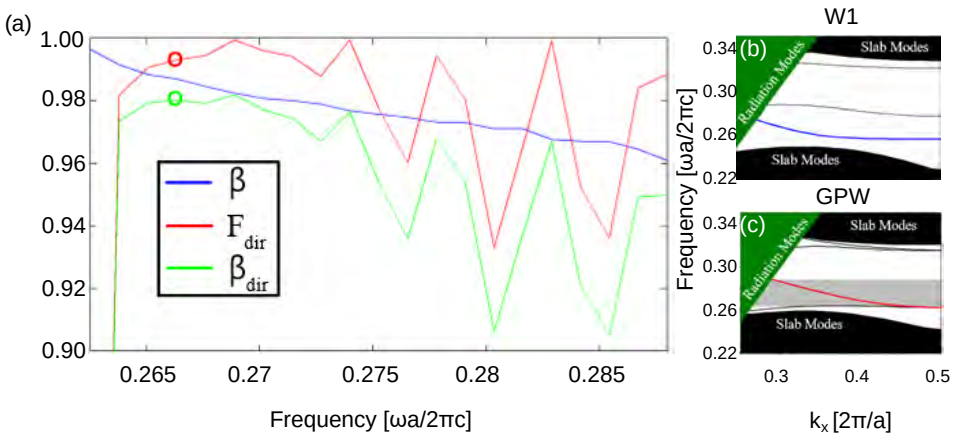

Figure C.2: Spectral dependence: (a): Frequency sweep of β, F_{dir} and β_{dir} at the position of the cross in fig. 5.4 (c) and (d). **(b):** Band diagram of a W1 waveguide (top) and a GPW (bottom). The gray region indicates the frequency range investigated in (a). Figure from [125].

C.1 Derivation of output from MZI with GPW

In the following the output states are calculated for the two different input states: $|0\rangle|1\rangle$ and $|1\rangle|0\rangle$ sent into a circuit like the one in fig. 5.7 (d) in the main text. The following derivation assumes a variable phase shifter in the lower arm.
First we consider the case on the input state $|1\rangle|0\rangle$:
The effect of the first beam splitter is to create a superposition with an imparted π-phase shift on the reflected photon

$$|1\rangle|0\rangle \xrightarrow{BS1} \frac{1}{\sqrt{2}}\Big(|1\rangle|0\rangle + i|0\rangle|1\rangle\Big), \tag{C.1}$$

The interaction with the quantum dot in the GPW imparts a π-phase shift depending on the spin-state of the quantum dot. Meanwhile, the phase-shifter in the other path imparts a ϕ-phase shift on the transmitted photon

$$\frac{1}{\sqrt{2}}\Big(|1\rangle|0\rangle + i|0\rangle|1\rangle\Big) \xrightarrow{QD,\phi} \frac{1}{\sqrt{2}}\Big(e^{i\phi}|1\rangle|0\rangle + it_k|0\rangle|1\rangle\Big) \tag{C.2}$$

Now the effect of the second beam splitter can be written

$$\frac{1}{\sqrt{2}}\Big(e^{i\phi}|1\rangle|0\rangle + it_k|0\rangle|1\rangle\Big) \xrightarrow{BS2} \frac{1}{\sqrt{2}}\left[e^{i\phi}\left(\frac{1}{\sqrt{2}}(|1\rangle|0\rangle + i|0\rangle|1\rangle)\right) + it_k\left(\frac{1}{\sqrt{2}}(|0\rangle|1\rangle + i|1\rangle|0\rangle)\right)\right] \tag{C.3}$$

This last state can be rewritten as:

$$\frac{1}{2}(e^{i\phi} - t_k)|1\rangle|0\rangle + \frac{i}{2}(e^{i\phi} + t_k)|0\rangle|1\rangle \tag{C.4}$$

Going through the same calculations for the other input state yields

$$|0\rangle|1\rangle \xrightarrow{BS1} \frac{1}{\sqrt{2}}\Big(i|1\rangle|0\rangle + |0\rangle|1\rangle\Big), \tag{C.5}$$

The interaction with the quantum dot in the GPW imparts a π-phase shift depending on the spin-state of the quantum dot. Meanwhile, the phase-shifter in the other path imparts a ϕ-phase shift on the transmitted photon

$$\frac{1}{\sqrt{2}}\Big(i|1\rangle|0\rangle + |0\rangle|1\rangle\Big) \xrightarrow{QD,\phi} \frac{1}{\sqrt{2}}\Big(ie^{i\phi}|1\rangle|0\rangle + t_k|0\rangle|1\rangle\Big) \tag{C.6}$$

Now the effect of the second beam splitter can be written

$$\frac{1}{\sqrt{2}}\Big(ie^{i\phi}|1\rangle|0\rangle + t_k|0\rangle|1\rangle\Big) \xrightarrow{BS2} \frac{1}{\sqrt{2}}\left[ie^{i\phi}\Big(\frac{1}{\sqrt{2}}(|1\rangle|0\rangle + i|0\rangle|1\rangle)\Big) + t_k\Big(\frac{1}{\sqrt{2}}(|0\rangle|1\rangle + i|1\rangle|0\rangle)\Big)\right] \tag{C.7}$$

In this case the last state can be rewritten as

$$\frac{i}{2}(e^{i\phi} + t_k)|1\rangle|0\rangle + \frac{1}{2}(-e^{i\phi} + t_k)|0\rangle|1\rangle \tag{C.8}$$

The probability of an output state is given by the absolute-square value of the prefactor in eqs. (C.4) and (C.8). We call the input states $|0\rangle|1\rangle$ and $|1\rangle|0\rangle$, 1 and 2 respectively. The output states are referred to as 3 ($|0\rangle|1\rangle$) and 4 ($|1\rangle|0\rangle$).
The probability of the photon leaving port 4, given that it entered port 1 is thus given by

$$\begin{aligned}\text{Prob.}_{31} = \left|\frac{1}{2}(ie^{i\phi} + it_k)\right|^2 &= \frac{1}{4}(ie^{i\phi} + it_k)(-ie^{-i\phi} - it_k)\\ &= \frac{1}{4}(1 + t_k e^{i\phi} + t_k e^{-i\phi} + t_k^2)\\ &= \frac{1}{2}(1 + t_k\cos\phi)\end{aligned} \tag{C.9}$$

Similarly

$$\begin{aligned}\text{Prob.}_{41} &= \frac{1}{2}(1 - t_k\cos\phi)\\ \text{Prob.}_{32} &= \frac{1}{2}(1 + t_k\cos\phi)\\ \text{Prob.}_{42} &= \frac{1}{2}(1 - t_k\cos\phi)\end{aligned} \tag{C.10}$$

The value $t_k = \pm 1$ depending on whether or not the control photon interacted with the quantum dot. Balancing the interferometer so that $\phi = 2n\pi$, we can write the probabilities of the two outputs in the case of the two inputs as

in \out	3	4
1	$\frac{1}{2}(1-t_k)$	$\frac{1}{2}(1+t_k)$
2	$\frac{1}{2}(1+t_k)$	$\frac{1}{2}(1-t_k)$

Hence, if we know the in- and output states of the system, we can deduce the spin-state of the emitter.

C.2 Photon statistics in the Bad-Cavity limit

The following is taken from Ref. [120] and follows the derivation presented in Ref. [135].

We are interested in the dynamics of a two-level system interacting with the electromagnetic radiation confined in a cavity.
The ideal case of a two-level system interacting with a cavity field is described by the Jaynes-Cummings model [152] where the interaction is given by the Hamiltonian

$$\hat{H}_I = -\hat{\mathbf{d}} \cdot \hat{\mathbf{E}} = A(\hat{\sigma}_+ + \hat{\sigma}_-)(\hat{a} + \hat{a}^\dagger), \tag{C.11}$$

where $\hat{\mathbf{d}}$ is the dipole moment operator of the emitter associated with the transition from the ground state to the excited state; $\hat{\sigma}_+ = |e\rangle\langle g|$ and the transition from the excited state to the ground state; $\hat{\sigma}_- = |g\rangle\langle e|$. $\hat{\mathbf{E}}$ is the field associated with creation operator $\hat{a}^\dagger$ and annihilation operator $\hat{a}$, and A denotes the coupling strength between field and emitter.
The non-energy conserving terms $\sigma_+ a^\dagger$ and $\sigma_- a$ corresponding to the non-physical situations of; creating a photon in the field while the atom undergoes a transition from the ground to the excited state, or the other way around can be discarded yielding

$$\hat{H}_I = A(\hat{\sigma}_+ \hat{a} + \hat{\sigma}_- \hat{a}^\dagger). \tag{C.12}$$

This model is only valid in the case where we neglect the systems interaction with the environment. A more realistic model can be achieved by allowing the environment to influence the evolution of the system.
In the following we will consider a two-level emitter with a number of decay channels, other than the one into the cavity mode, in a lossy cavity, thus allowing dissipation of both the emitter and the cavity. Furthermore, we will add a coherent driving field on resonance with the emitter and the cavity. In this case the behavior of the system can be explained in term of the driving field amplitude ε, the coupling constant g, the atomic damping rate γ and the cavity damping rate; κ. From these, a saturation parameter can be defined as

$$n_s = \frac{\gamma^2}{8g^2} = \frac{\gamma}{8C\kappa}, \tag{C.13}$$

where

$$C = \frac{g^2}{\kappa\gamma}, \tag{C.14}$$

is the cooperativity that denotes an interaction-to-decay ratio. Another usefull parameter turns out to be

$$Y = \frac{\varepsilon}{\kappa\sqrt{n_s}} \tag{C.15}$$

i.e., a measure of the relation between the coherent driving field strength and the cavity decay rate.

As we are interested in a system that inevitably interacts with the environment, but not explicitly in the evolution of the environment, we use a density operator formalism suited for treating a system composed of two subsystems of which only one is of interest [153].

Given that the total system can be in a number of quantum states $|\psi_i\rangle$ with probability p_i, then the density operator is given by

$$\hat{\rho} = \sum_i p_i \left|\psi_i\right\rangle \left\langle\psi_i\right| . \tag{C.16}$$

As we are only interested in the subsystem comprised of the atom and the cavity, we trace out the environment, thus obtaining the reduced density operator for the atom-cavity system as influenced by the environment

$$\hat{\rho}_S = \mathrm{Tr}_E[\hat{\rho}]. \tag{C.17}$$

It is this interaction with the environment that gives rise to the dissipative behavior of the system.

The evolution of the total system is governed by the Hamiltonian $\hat{H} = \hat{H}_S + \hat{H}_E + \hat{H}_{SE}$, where $\hat{H}_S$ is the system Hamiltonian; $\hat{H}_E$ is the Hamiltonian for the environment, and $\hat{H}_{SE}$ governs the interaction between system and environment. The evolution of the emitter-cavity system is given by

$$\dot{\hat{\rho}}_S = \mathrm{Tr}_E[\dot{\hat{\rho}}]. \tag{C.18}$$

The time evolution of the system is given by

$$\dot{\hat{\rho}} = \frac{i}{\hbar}[\hat{H}, \hat{\rho}]. \tag{C.19}$$

This yields

$$\dot{\hat{\rho}}_S = \frac{i}{\hbar}\Big[[\hat{H}_S, \hat{\rho}_S] + \mathrm{Tr}_E[\hat{H}_E, \hat{\rho}_S] + \mathrm{Tr}_E[\hat{H}_{SE}, \hat{\rho}]\Big]. \tag{C.20}$$

In our case of a subsystem consisting of a two-l evel emitter in a cavity, the first term in eq. (C.20) describes the free evolution of the emitter and the field as well as the interaction between the emitter and the field, the second term is zero, and the last term describes the system-environment interaction and consequently the

dissipation of the emitter and cavity respectively. The system under investigation can be described by the master equation

$$\dot{\hat{\rho}}_S = \varepsilon[\hat{a}^\dagger - \hat{a}, \hat{\rho}] + g[\hat{a}^\dagger\hat{\sigma}_- - \hat{a}\hat{\sigma}_+, \hat{\rho}] + \frac{\gamma}{2}(2\hat{\sigma}_-\hat{\rho}\hat{\sigma}_+ - \hat{\sigma}_+\hat{\sigma}_-\hat{\rho} - \hat{\rho}\hat{\sigma}_+\hat{\sigma}_-) + \kappa(2\hat{a}^\dagger\hat{\rho}\hat{a} - \hat{a}^\dagger\hat{a}\hat{\rho} - \hat{\rho}\hat{a}^\dagger\hat{a}) \quad \text{(C.21)}$$

The second term is the Jaynes Cummings-interaction, and the last two damping terms are written in Lindblad form [154].
From this the time-dependent expectation values for operators acting in the Hilbert space of the system can be found. Specifically for the atomic operators we have

$$\langle\dot{\hat{\sigma}}_-\rangle = \dot{\hat{\rho}}_{ge}, \quad \text{(C.22a)}$$
$$\langle\dot{\hat{\sigma}}_+\rangle = \dot{\hat{\rho}}_{eg}, \quad \text{(C.22b)}$$
$$\langle\dot{\hat{\sigma}}_z\rangle = \dot{\hat{\rho}}_{ee} - \dot{\hat{\rho}}_{gg}, \quad \text{(C.22c)}$$

where $\dot{\hat{\rho}}_{ij} = \langle i|\,\dot{\hat{\rho}}\,|j\rangle$. This yields;

$$\langle\dot{\hat{\sigma}}_-\rangle = 2g\langle\hat{\sigma}_z\hat{a}\rangle - (\gamma/2)\langle\hat{\sigma}_-\rangle, \quad \text{(C.23a)}$$
$$\langle\dot{\hat{\sigma}}_+\rangle = 2g\langle\hat{a}^\dagger\hat{\sigma}_z\rangle - (\gamma/2)\langle\hat{\sigma}_+\rangle, \quad \text{(C.23b)}$$
$$\langle\dot{\hat{\sigma}}_z\rangle = -g(\langle\hat{a}^\dagger\hat{\sigma}_-\rangle + \langle\hat{\sigma}_+\hat{a}\rangle) - \gamma(\langle\hat{\sigma}_+\rangle + 1/2). \quad \text{(C.23c)}$$

In order to adiabatically eliminate the field from eq. (C.23c) we consider the Heisenberg equation of motion for the field: $\dot{\hat{a}} = \frac{i}{\hbar}[\hat{H}_s, \hat{a}]$ and include the decay of the cavity field ($\kappa\hat{a}$) and a Langevin force operator $\hat{\xi}$. The Langevin force is added to ensure that the commutator doesn't decay exponentially

$$\dot{\hat{a}} = g\hat{\sigma}_- + \varepsilon - \kappa\hat{a} + \hat{\xi} \quad \text{(C.24)}$$

In the bad-cavity limit, we can adiabatically eliminate the cavity field by assuming $\dot{\hat{a}} = 0$. The bad-cavity limit can be defined by letting

$$\frac{\kappa}{\gamma} \to \infty, \qquad n_s \to 0, \qquad \frac{\varepsilon}{\kappa} \to 0 \quad \text{(C.25)}$$

with C and Y constant. Hence, in this limit the decay rate of the cavity, κ, is large compared to the decay rate of the emitter,γ; the saturation parameter,n_s, that is; the number of photons in the cavity mode required to saturate the emitter, goes to zero and the driving field amplitude is relatively small.

In this limit we can find an expression for $\hat{a}$ in terms of κ, ε, g and $\hat{\sigma}_-$.

Namely

$$\hat{a} = \frac{g\hat{\sigma}_-}{\kappa} + \frac{\varepsilon}{\kappa} + \frac{\hat{\xi}}{\kappa}. \tag{C.26}$$

In terms of the parameters introduced earlier the cavity operator may be written

$$\hat{a}(t) = \sqrt{n_s}[Y + 2\sqrt{2}C\hat{\sigma}_-(t)] + \frac{\hat{\xi}}{\kappa}. \tag{C.27}$$

Using the commutation relations for the atomic operators and the fact that a Langevin force acting on a reservoir vacuum state is zero, we can express the equations of motion for the atomic operator expectation values, also known as the optical Bloch equations

$$\langle\dot{\hat{\sigma}}_-\rangle = \frac{\gamma Y}{\sqrt{2}}\langle\hat{\sigma}_z\rangle - \frac{\gamma}{2}(1+2C)\langle\hat{\sigma}_-\rangle, \tag{C.28a}$$

$$\langle\dot{\hat{\sigma}}_+\rangle = \frac{\gamma Y}{\sqrt{2}}\langle\hat{\sigma}_z\rangle - \frac{\gamma}{2}(1+2C)\langle\hat{\sigma}_+\rangle, \tag{C.28b}$$

$$\langle\dot{\hat{\sigma}}_z\rangle = -\frac{\gamma Y}{2\sqrt{2}}(\langle\hat{\sigma}_+\rangle + \langle\hat{\sigma}_-\rangle) - \gamma(1+2C)(\langle\hat{\sigma}_z\rangle + 1/2). \tag{C.28c}$$

By comparing these to the optical Bloch equations for single atom resonance fluorescence [154], we see that the effect of the cavity is to increase the emission rate by a factor of (1+2C).
The statistics of the transmitted light differs from the case of resonance fluorescence, and thus the effect of the cavity on the photon statistics in the transmitted field can be investigated through analysis of the second-order correlation function.

C.3 Second-order correlation function

The second order correlation function carries information about the photon number distribution in a given field and essentially quantifies the probability of detecting a photon at time $t+\tau$ given that a photon was detected at time t.
Generally the normalized second order correlation function is given by

$$g^{(2)}(\tau) = \frac{\langle\hat{E}^{(-)}(t)\hat{E}^{(-)}(t+\tau)\hat{E}^{(+)}(t+\tau)\hat{E}^{(+)}(t)\rangle}{\langle\hat{E}^{(-)}(t)\hat{E}^{(+)}(t)\rangle\langle\hat{E}^{(-)}(t+\tau)\hat{E}^{(+)}(t+\tau)}, \tag{C.29}$$

where $\hat{E}^{(\pm)}$ is the positive and negative frequency part of the field. In the case of a standing wave field in a cavity we have

$$\hat{E}^{(+)}(z,t) = i\mathbf{e}\left(\frac{\hbar\omega_0}{\epsilon_0 AL}\right)^{1/2}\sin\left(\frac{\omega_0 z}{c}\right)e^{-i\omega_0 t}\hat{a}(t), \tag{C.30}$$

where $\hat{a}$ is the anihilation operator, ω_0 is the frequency of the driving field (that is on resonance with the cavity mode and the two level system in our case), $\mathbf{e}$ is a

polarization vector, and L and A are length and transverse area of the cavity mode respectively. In this case of a single mode field $g^{(2)}(\tau)$ reduces to

$$g^{(2)}(\tau) = \frac{\langle \hat{a}^\dagger(0)\hat{a}^\dagger(\tau)\hat{a}(\tau)\hat{a}(0)\rangle}{(\langle \hat{a}^\dagger\hat{a}\rangle_{ss})^2}. \tag{C.31}$$

In order to evaluate this expression we need to calculate normally ordered, time ordered averages. When the field operator can be written as in eq. (C.27), we get

$$\begin{aligned}\langle \hat{a}^\dagger(t_1)\hat{a}^\dagger(t_2)\hat{\Sigma}\hat{a}(t_2)\hat{a}(t_1)\rangle \\ = n_s^2\langle [Y + 2\sqrt{2}C\hat{\sigma}_+(t_1)][Y + 2\sqrt{2}C\hat{\sigma}_+(t_2)] \\ \times \hat{\Sigma}[Y + 2\sqrt{2}C\hat{\sigma}_-(t_2)][Y + 2\sqrt{2}C\hat{\sigma}_-(t_1)]\rangle\end{aligned} \tag{C.32}$$

where $\hat{\Sigma}$ is an arbitrary atomic operator.
This expression along with the optical Bloch equations (C.28c), gives an expression for the normalized second order correlation function [135]

$$\begin{aligned}g^{(2)}_{ss}(\tau) = 1 + \left(\frac{n_s}{\langle \hat{a}^\dagger\hat{a}\rangle}\right)^2 8C^2 \cdot \Big\{ & 4Y^2\langle : \Delta\hat{\sigma}_1(0)\Delta\hat{\sigma}_1(\tau) : \rangle_{ss} \\ & + 2\sqrt{2}CY[\langle \Delta\hat{\sigma}_+(0)\Delta\hat{\sigma}_+(\tau)(\Delta\hat{\sigma}_-(\tau) + \Delta\hat{\sigma}_-(0))\rangle_{ss} + h.c.] \\ & + 8C^2[\langle \Delta\hat{\sigma}_+(0)\Delta\hat{\sigma}_+(\tau)\Delta\hat{\sigma}_-(\tau)\Delta\hat{\sigma}_-(0)\rangle_{ss} - (\langle \Delta\hat{\sigma}_-\Delta\hat{\sigma}_-\rangle_{ss})^2]\Big\}\end{aligned} \tag{C.33}$$

where $\Delta\hat{\sigma}_1 = \frac{1}{2}(\Delta\hat{\sigma}_- + \Delta\hat{\sigma}_+)$, and $\Delta\hat{\sigma}_\pm = \hat{\sigma}_\pm - \langle\hat{\sigma}_\pm\rangle_{ss}$.
From this we see that we need the steady state solutions to the Bloch equations (C.28c), evaluated from $\langle\dot{\hat{\sigma}}_{\pm,z}\rangle = 0$

$$\langle\hat{\sigma}_\pm\rangle_{ss} = -\frac{1}{\sqrt{2}}\frac{Y(1+2C)}{(1+2C)^2+Y^2}, \quad \text{and} \quad \langle\hat{\sigma}_z\rangle_{ss} = -\frac{1}{2}\frac{(1+2C)^2}{(1+2C)^2+Y^2} \tag{C.34}$$

Moreover, we need to evaluate the expectation values of the atomic operators. This can be done by first writing the Bloch equations in a more general form

$$\dot{\hat{\sigma}}_i = \mathbf{M}_{ij}\hat{\sigma}_j + \lambda_i \tag{C.35}$$

Where in our case the matrix $\mathbf{M}$ is given by

$$\mathbf{M} = \gamma\begin{pmatrix} -\frac{1+2C}{2} & \frac{Y}{\sqrt{2}} & 0 \\ \frac{-Y}{2\sqrt{2}} & -(1+2C) & \frac{-Y}{2\sqrt{2}} \\ 0 & \frac{Y}{\sqrt{2}} & -\frac{1+2C}{2} \end{pmatrix}$$

and

$$\lambda = \gamma \begin{pmatrix} 0 \\ \frac{1}{2}(1+2C) \\ 0 \end{pmatrix}$$

Moreover, the quantum regression theorem allows us to calculate multiple-time operator correlation functions from the knowledge of of single time expectation values [155].

$$\frac{\mathrm{d}}{\mathrm{d}t}\langle\hat{\sigma}_i(t)\hat{\sigma}_k(0)\rangle = M_{ij}\langle\hat{\sigma}_j(t)\hat{\sigma}_k(0)\rangle + \lambda_i\langle\hat{\sigma}_k(0)\rangle, \tag{C.36a}$$

$$\frac{\mathrm{d}}{\mathrm{d}t}\langle\hat{\sigma}_k(0)\hat{\sigma}_i(t)\hat{\sigma}_m(0)\rangle = M_{ij}\langle\hat{\sigma}_k(0)\hat{\sigma}_j(t)\hat{\sigma}_m(0)\rangle + \lambda_i\langle\hat{\sigma}_k(0)\hat{\sigma}_m(0)\rangle, \tag{C.36b}$$

Rice and Carmichael [135] showed, that the atomic correlation functions appearing in eq. (C.33) can be evaluated from the quantum regression theorem (C.36b), the Bloch equations (C.28c) and steady state solutions (C.34)

$$g_{ss}^{(2)}(\tau') = 1 + \left(\frac{2\sqrt{2}C}{1+Y^2}\right)^2 e^{-(3/4)\tau'} \cdot \Big\{(Y^2+2C^2-1)\cosh(\Omega\tau')+ (4\Omega)^{-1}[Y^2\frac{5-2C}{1+2C} - 1 - 2C^2]\sinh(\Omega\tau')\Big\} \quad , \tag{C.37}$$

where

$$\tau' = \gamma(1+2C)\tau \qquad \text{and} \qquad \Omega = \frac{1}{4}\left[1 - \frac{8Y^2}{(1+2C)^2}\right]^{1/2} \tag{C.38}$$

When $Y \ll 1$ corresponding to a very weak driving field, we see that $\Omega = \frac{1}{4}$ and the expression for $g_{ss}^{(2)}(\tau')$ can be written

$$g_{ss}^{(2)}(\tau') = (1 - 4C^2 e^{-\tau'/2})^2, \tag{C.39}$$

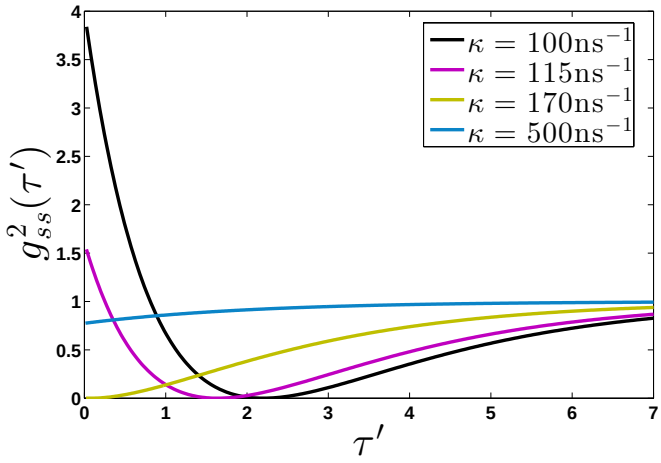

Figure C.3: Normalized Second order correlation versus delay τ' for a weak driving field: $Y = 0.001$, and small emitter damping rate: $\gamma = 0.01\text{ns}^{-1}$

In fig. C.3 eq. (C.39) has been plotted as a function of the dimenesionless time τ', for different values of the cavity damping rate κ, where κ is related to the Q-factor through; $\kappa = \omega_c/Q$. This shows the probability for a second photon to be detected in the transmitted field, conditioned on the detection of a first photon at $\tau = 0$.
For $\kappa \leq 115$, the plots clearly show bunching at zero time delay, followed by anti-bunching at a later time $\tau'_a = 2\ln(4C^2)$.
According to the usual definition of anti-bunching, namely

$$g^{(2)}_{ss}(0) < 1, \qquad g^{(2)\prime}_{ss}(0) = 0 \qquad \text{and} \qquad g^{(2)\prime\prime}_{ss}(0) > 0, \tag{C.40}$$

the photon statistics in the case of $\kappa \leq 115$ ns^{-1} is not non-classical as the value at zero time delay is greater than one. However, the fact that the value subsequently drops to zero is nonclassical.
According to the Schwarz inequality

$$|\langle I(\tau)I(0)\rangle_{ss} \leq \langle I^2\rangle|, \tag{C.41}$$

which yields

$$g^{(2)}(\tau) \leq g^{(2)}(0). \tag{C.42}$$

This inequality is not violated, yet it can be shown that the vanishing of $g^{(2)}_{ss}(\tau'_a)$ as given by (C.39) is not allowed for a classical field when $g^{(2)}_{ss}(0) < 2$ [135].
By expressing the intensity as a mean value plus the deviation from the mean $I = \langle I\rangle_{ss} + \Delta I$, we get an expression for the normalized intensity correlation function

$$g^{(2)}_{ss}(\tau) = 1 + \frac{\langle \Delta I(\tau)\Delta I(0)\rangle_{ss}}{(\langle I\rangle_{ss})^2}. \tag{C.43}$$

Applying the Schwartz inequality to this expression we get

$$|\langle \Delta I(\tau)\Delta I(0)\rangle_{ss}| \leq \langle (\Delta I)^2\rangle_{ss}, \tag{C.44}$$

where equality is obtained when $\tau = 0$.
From this we can establish the inequality

$$|g^{(2)}_{ss}(\tau) - 1| \leq |g^{(2)}_{ss}(0) - 1|, \tag{C.45}$$

and from this we can see, that if $g^{(2)}_{ss}(0) < 2$ then the RHS is smaller than 1, and hence $g^{(2)}_{ss}(\tau)$ cannot vanish. Hence, when $g^{(2)}_{ss}(0) < 2$ the subsequent antibunching at τ'_a is non-classical as it violates the inequality given by eq. (C.45). This antibunching behavior differs from the one familiar from resonance fluorescence, where detection of the first photon indicates that the two-level system is in its ground state, and thus cannot fluoresce. This naturally leads to $g^{(2)}(0) = 0$. By adding a cavity to the system, the interpretation is not as straight forward. Detecting a photon in the transmitted field does not mean that the two-level system is now in its ground state, as the transmitted field is a superposition of the forward reradiation from the dipole with the coherent driving field.
Understanding of the behavior of the second order correlation function can be gained by investigating the reduced quantum state, i.e., the state of the emitter prepared by the first photodetection. In the following this reduction upon photodetection will be termed "jump".

$$\mathrm{tr}(\bar{\rho}(0)\hat{\sigma}_{\pm}) = -\frac{1}{\sqrt{2}}\frac{Y}{1+Y^2} \tag{C.46a}$$

$$\mathrm{tr}(\bar{\rho}(0)\hat{\sigma}_{z}) = -\frac{1}{2}\frac{1}{1+Y^2} \tag{C.46b}$$

where $\bar{\rho}(0)$ denotes the reduced state prepared by the jump. Comparing this to the general expression for the steady state values of the atomic operators (C.34) , we can see that after the first photodetection the cavity enhancement, as expressed through the factor $(1 + 2C)$ in (C.34) is temporarily turned off. Hence, for all C, the jump will cause an increase in the absolute value of the atomic operators $\langle\hat{\sigma}_{\pm}\rangle$ as $\hat{\sigma}_{\pm,jump} > \langle\hat{\sigma}_{\pm}\rangle_{ss}$.

The same can be observed when comparing the mean field amplitude inside the cavity after state reduction

$$\mathrm{tr}(\bar{\rho}(0)\hat{a}) = \sqrt{n_s}\left[Y - 2C\frac{Y}{1+Y^2}\right] \tag{C.47}$$

to the steady state value as obtained from eq. (C.27) and $\langle\sigma_-\rangle$ given by eq. (C.34)

$$\langle\hat{a}\rangle_{ss} = \sqrt{n_s}\left[Y - 2C\frac{Y(1+2C)}{(1+2C)^2+Y^2}\right], \tag{C.48}$$

For weak driving fields, the steady state solution reduces to

$$\langle \hat{a} \rangle_{ss} = \sqrt{n_s}\Big[Y - \frac{2CY}{(1+2C)}\Big], \tag{C.49}$$

and the first term, i.e., the in-phase part dominates, where after photodetection and in the case of $C > 0.5$, the out of phase part of the field is greater than the driving field amplitude. Thus for $C > 0.5$, the amplitude of the field experiences a π phase-shift due to the detection of the first photon.

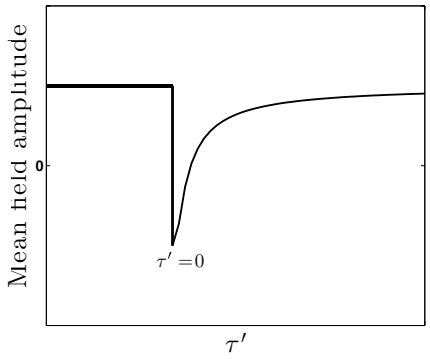

Figure C.4: Evolution of mean cavity field amplitude. The 'jump' takes place at $\tau' = 0$ and the state subsequently evolves back to the steady state

Figure C.4 shows how the mean field amplitude evolves. After the jump, relaxation back to the steady-state will pass through zero at time τ_a', causing the antibunching seen in fig. C.3 for $\kappa < 200$ corresponding to $C > 0.43$.
The correlation function is proportional to the probability density for a second transmitted photon to be detected, and thus takes on the value of the modulus square of the field and the antibunching in the second order correlation function stems from the passing through zero as field relaxes back to the steady-state value after the jump.
Physically this corresponds to destructive interference between the driving field and the driven atomic dipole leading to a zero probability of detecting a second photon.

For $C > 0.5$ we see an increase in the probability to detect a second photon immediately after the jump. From fig. (C.3) we can see that the "degree" of bunching at $\tau' = 0$ depends on the damping rate of the cavity; κ. To see how the behavior of the second order correlation function immediately after the jump depends on κ, fig. C.5 shows $g_{ss}^{(2)}(0)$ versus κ, where the value of the second order correlation function at $\tau = 0$, is obtained from eq. (C.39) and yields

$$g_{ss}^{(2)}(0) = (1 - 4C^2)^2. \tag{C.50}$$

Here the cooperativity depends on the emitter and cavity decay rates as: $C = \frac{g^2}{\kappa\gamma}$.

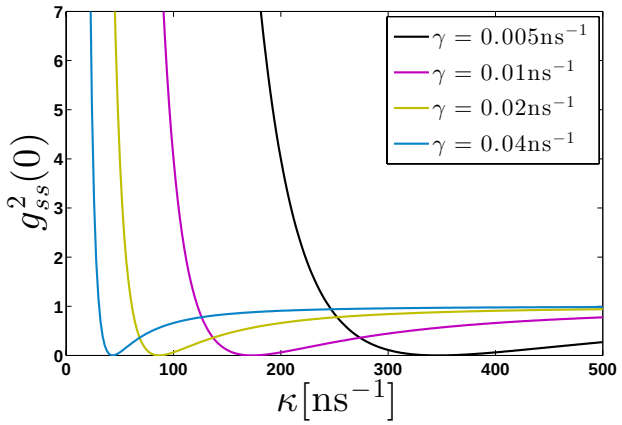

Figure C.5: The value of g^2_{ss} at $\tau = 0$ versus cavity decay rate κ for different values of the emitter damping rate; γ and $g^2 = \sqrt{3}/2$.

From eq. (C.50) we see that the value of $g^{(2)}_{ss}(0)$ will drop to zero when $C = 0.5$, and therefore; depending on the decay rate of the emitter (γ), the value of the second order correlation function at $\tau = 0$, goes to zero for different values of the cavity decay rate (κ) and constant emitter-field coupling constant, g.
For relatively small values of the cavity damping rate (κ) the probability of detecting a second photon at $\tau' = 0$ goes to infinity as the cooperativity ($C = \frac{g^2}{\kappa\gamma}$) is inversely proportional to κ, and the mean cavity field amplitude will be dominated by the second term of eq. (C.47). As κ grows, this probability drops to zero corresponding to the situation where the driving field and the field scattered off the emitter interfere destructively. For even larger values of κ, $g^{(2)}_{ss}(0)$ approaches 1 as the coherent driving field becomes the dominant term in eq. (C.47).